UNIVERSITY OF COPENHAGEN
FACULTY OF SCIENCE

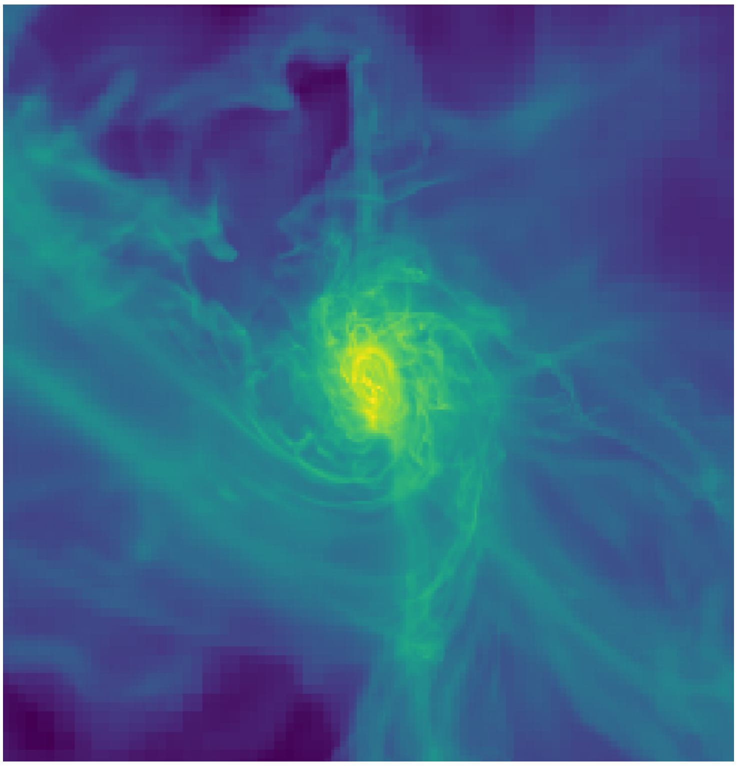

MSc Thesis

Modelling Collapse and Accretion of Protostellar Systems

Daniel Dalsgaard Jonsson

Advisors: Troels Haugbølle and Åke Nordlund

Submitted: June 16, 2023

A thesis submitted in fulfillment of the requirements for the degree of Master of Science in Physics

Abstract

The process of star formation is a truly fascinating one. The attracting properties of self-gravity allows matter in a dense core, with an extent of up to 10.000 AU, to collapse into a star with an extent of 0.001 AU. This, along with the rest of the process, is a multi-scale physical problem extending over 10 orders of magnitude, thus making it difficult to simulate. In this thesis I have investigated the process of accretion with sink particles at varying resolutions and implemented new physics, in the simulation code, RAMSES, to track the induced spin of the forming protostar. As such, we obtain a better understanding of the interplay and evolution of the star particle with its surroundings. This is done by adapting RAMSES to incorporate spin tracking and to handle accretion in binary systems with a recipe inspired by literature on binary blacks holes. I successfully show that this is an improvement to previous versions of RAMSES through tests in isolated idealised scenarios, zooming in on a realistic large scale simulation, and in a large scale simulation with many binary systems. The overall conclusion is that these methods show promising potential, although rigorous testing is needed before it can be applied to the production version of the simulation code.

Contents

Chapter 1

Introduction

The always attracting properties of self-gravity are remarkable in that they allow matter from dense cores of up to 10.000 AU to be collected and compacted into stars, which only extends a mere 0.001 AU. In addition, the dense cores are fed by highly turbulent and filamentary streamers at even larger parsec-scales, corresponding to millions of AUs. This makes star formation a truly multi-scale (and multi-physics) problem, which a priori requires modelling over more than 10 orders of magnitude in space and time. Codes implementing numerical algorithms using adaptive mesh refinement have only recently been sufficiently performant to deal with such a large dynamical range. However, in the few cases where it has been done, the process can only be followed for short amounts of time up to 1000 yr, i.e. much shorter than the million years it takes for the birth and accretion of a single star.

The numerical alternative is to describe the process of gravitational collapse and accretion in a sub-grid model, where at a certain level — in general much larger than the stellar radius — the star is represented by a so-called sink particle that can move, interact gravitationally, and accrete matter. In highly symmetric simple cases, the collapse and accretion can be described semi-numerically, but in general the flow is highly turbulent at early times, while at later times accretion proceeds through a disk.

The aim of this thesis is to investigate the process of accretion using sink particles at various resolutions, as well as to implement new physics in the simulation code RAMSES. This allows us to track the induced spin of the forming protostar, thus providing a better understanding of the interplay and evolution of the star particle with its surroundings. Finally, this gives a physics inspired way of simulating accretion of binary systems. In chapter 2 we introduce relevant background information to understand the physics of the thesis. Chapter 3 describes the methods of modelling star formation, including an introduction to magnetohydronamics, it descibes the simulation code used for this thesis, and it describes the analysis tools developed as part of this work. Accretion and sink particles are central to this thesis and so they have their own chapter, which is chapter 4, where we describe the numerical method of accretion, the implementation of tracking the spin of the stars, and the new accretion recipes. In chapter 5 we test our implementations and discuss the implications of these. Finally, chapter 6 summarises our conclusions.

1.1 Data Availability

Figures and movies from this thesis illustrating physical and numerical processes are available on ERDA through the link `https://sid.erda.dk/cgi-sid/ls.py?share_id=GIUf2SnMg8`. The datasets generated and analyzed in this thesis are not publicly available due to the large data volume and the ongoing research of other aspects of the datasets, but they are available on reasonable request and stored in accordance with FAIR practices on ERDA and the Astro cluster at the Science HPC centre.

Chapter 2

Background

It has long been thought that stars form by gravitational collapse of diffuse matter, even as early as Newton after the theory of gravity was first formulated. However, in order to understand the intricate details of the stars forming and the impact on the general evolution of the universe, there is a range of physical processes that we need to consider (Richard B Larson 2003).

2.1 Interstellar Medium & Star Forming Regions

The Interstellar Medium, hereafter referred to as the ISM, is the material in the region of space between the stars. Contrary to what one might think, the space between the stars is in fact not empty, and the material has a significant impact on star formation. In this section we will look into what the ISM is, what it is made of, and its impact on star formation.

The ISM is, in rough terms, remnants from the Big Bang, but with it being ever-changing since the ISM is much longer lived than stars, meaning that the stars form, live, and die, all in the same ISM, which is altering the ISM slightly. The ISM is also a general term used to group Molecular Clouds, neutral Hydrogen, H I, regions, ionised Hydrogen, H II, regions, and warm H I and H II regions. The physical parameters of the ISM can change by many orders of magnitude depending on which of these regions it is. Particularly relevant is the number density of Hydrogen atoms and the temperature. The density is observed between ~ 0.001 atoms per cm^3 to ~ 10000 atoms per cm^3 and the temperature is observed to be between $\sim$ 10K to over 10^6K (Schulz 2012).

The composition of the ISM is mostly unchanged since its formation in the early universe, starting out with a Hydrogen to Helium ratio of about $1000 : 85$ and some trace deuterium, lithium, and beryllium. Now Hydrogen is about 90% of the matter in the ISM, whether that is neutral, ionised, or molecular. The components of the ISM can be broken into the following categories; Hydrogen, Helium, trace elements like C, O, Fe, and others, molecules like CO, CS, and others, dust, cosmic ray particles, magnetic fields, and radiation fields (Schulz 2012).

Stars form in the ISM and so, naturally, the ISM has a big impact on how the stars form and the rate at which they form. Generally we are interested in the Star Formation Rate (SFR) to help us describe the galaxy, to find its Initial Mass Function (IMF), which is the distribution of stellar masses with a given volume of a star forming region in space, and to tell us something about the evolution of the galaxy. We can measure the SFR in a few different ways, depending on the redshift of the galaxy. The first is for galaxies with $z \leq 0.4$ where we can use the H_α (6563 Å) line luminosities. The second is for galaxies with a redshift in the range $0.4 < z \leq 1$, where we can use the O II (3727 Å) line luminosities. For $z > 1$ we can use the UV continuum luminosity in the wavelength range of 1500 Å to 2800 Å. Finally, in the far IR we can use the 60 µm luminosities for the low IR background. All of these use an empirically determined estimation factor to convert the luminosities into a star formation rate.

Stars form in regions with dense gas where almost all the hydrogen is in its molecular form. These are most often placed either in spiral arms of the galaxies or in the galactic centres. What we know about these is mostly inferred from observations since the dust in the galaxies obscure the star forming regions around the centre, where we can observe the stars forming in the spiral arms directly (Richard B Larson 2003). We will discuss more about how we observe in the next section.

2.2 Observations & Class System

The following section will describe the class system we use for stars along with the basics of how we observe them.

Observationally young stars can be classified according to their appearance. When the stars are very young, they are completely obscured inside the gaseous cocoon from which they accrete matter and no stars emitted from the stellar photosphere reaches the observer. The photons are instead absorbed by the surrounding gas and re-emitted at longer wavelengths. We designate them protostars. At later times, but still early in the life of a star, the stars emerge from the cocoon and photons can be observed directly from the stellar surface, those are termed Pre Main Sequence (PMS) stars. PMS because they are still contracting, but fusion of hydrogen at the center of the star has not yet commenced. This system has classes 0, I, II, and III, and it is based on the spectral energy distribution (SED) of the star in the IR wavelength range $1 - 100$ μm, since most of the emission in the early life of the star is in this wavelength range. The class is based both qualitatively on the shape of the SED and quantitatively on the spectral index α_{IR} as defined in Eq. 2.1 (Schulz 2012).

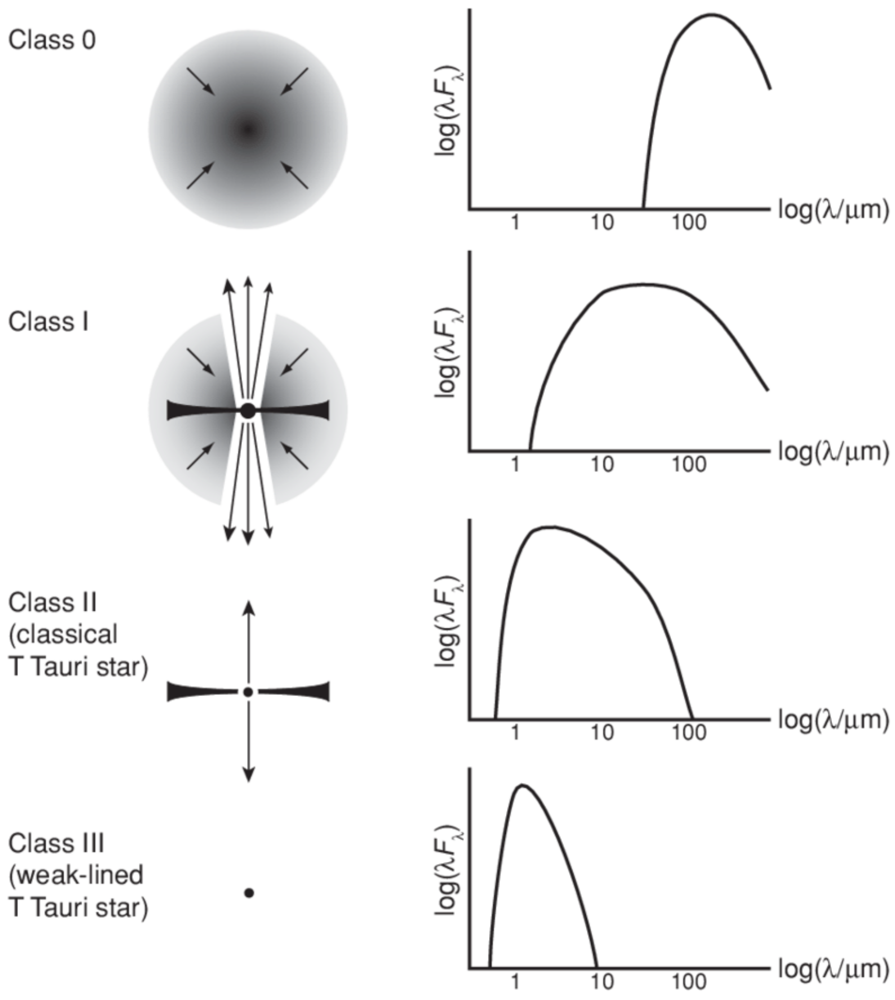

Figure 2.1: An illustration of what class 0, I, II, and III stars look like along with their spectral energy distribution used to give them this class. Figure from (Armitage 2010).

$$\alpha_{\mathrm{IR}} = \frac{d \ \log \lambda F_\lambda}{d \ \log \lambda} \tag{2.1}$$

Historically class I, II, and III were defined first and class 0 defined later based on the SED, so we will follow the descriptions in that way as well. Class I protostars are defined as having a very broad SED as can be seen in Fig. 2.1 and having spectral indices $\alpha_{\mathrm{IR}} > 0$. Class II PMS stars have a narrower SED than class I stars, but still broad, and they have $-2 < \alpha_{\mathrm{IR}} < 0$. Class III stars have a significantly narrower SED than both classes I and II, and they have $\alpha_{\mathrm{IR}} < -2$. Later it was discovered that there was a distribution of objects with emissions disappearing at wavelengths around 25 μm and below which indicates a large amount of material around the star, also pointing to it being a younger star. Seeing as this group of stars are younger, they are called class 0. The SED of class 0 stars can be seen in Fig. 2.1 where it is seen that it is narrower than classes I and II, but at higher wavelengths (Schulz 2012).

Figure 2.2: Picture of Atacama Large Millimeter Array (ALMA) by (Bončina 2010).

In order to observe any of these stars we need to use a observatory that fits our purpose. There are many telescopes with overlapping wavelength ranges and science instruments, and one of the ones often used to observe these stars is the Atacama large mm/submm array (ALMA) as seen in Fig. 2.2. When we are interested in observing star formation, we often want to observe in the IR, sub-mm, and mm wavelengths, since there is a lot of material, such as dust, obscuring our view in the visible wavelengths and, for the same reason as when classifying the stars, most of the emission early on in the life of a star is at wavelengths in the IR part of the spectrum (Schulz 2012).

2.3 Gravitational Collapse

The gravitational collapse of regions in the ISM lead to stars forming. This is typically in the most dense areas of the ISM, i.e., Molecular Clouds. Generally there are two ways we think clouds begin their collapse. The first is using stability analysis and assuming the initial state to be a Bonnor-Ebert sphere slightly over the stability threshold such that gravity wins over thermal pressure. The second is assuming that the prestellar core is magnetically supported and collapses gradually over time by ambipolar diffusion, which means that the gas contracts slowly across the field lines. This will eventually lead to a singular isothermal sphere without magnetic support, which is an unstable configuration. It is thought that physical processes cannot lead to this, but as an idealised case it is still useful to consider as a reference model. More realistic models are expected to be a mix of these two. We can consider the first as fast collapse and the second as slow collapse and as so they can be considered the upper and lower limits of a realistic model (Richard B Larson 2003; Schulz 2012).

A Bonnor-Ebert (BE) sphere is an isothermal, self-gravitating sphere of gas in hydrostatic equilibrium. The maximum mass the cloud has in order to still be in hydrostatic equilibrium is given by Eq. 2.2, where a mass greater than this will initialise a gravitational collapse, since this is a threshold for when the gravitational pull becomes greater than the pressure support present in hydrostatic equilibrium (R. B. Larson 1969; Shu 1977). This process is visualised as the sketch for class 0 protostars in Fig 2.1.

$$\mathrm{M_{crit}} = 1.18 \frac{\mathrm{c_s^3}}{\mathrm{G}^{3/2} \rho_{\mathrm{external}}^{1/2}} \tag{2.2}$$

In order to consider a more real world gravitational collapse, we must first look deeper at the effects of rotation, magnetic fields, and turbulence. Firstly, rotation acts as a stabiliser in general, but introducing the Toomre parameter in Eq. 2.3, we can define stability in terms of rotation. Here Ω_k

is the rotational Kepler speed, Σ is the surface density of the disk, assuming a thin disk, v_k is the Kepler speed, $\mathrm{M}^*_{\mathrm{disk}}$ is the approximate disk mass from $\mathrm{M}^*_{\mathrm{disk}} \approx \pi \mathrm{r}^2\Sigma$, and M_* is the mass of the core. We get instability if $\mathrm{Q} \gtrsim 1$ depending on the specific scenario, however in ideal cases like the BE sphere above, this is exactly 1 (Richard B Larson 2003; Toomre 1964). The second version of writing the parameter is more important when considering the evolution of protostellar systems as we will in the next section, but the same values of Q still apply, just determined from different quantities.

$$\mathrm{Q} = \frac{\mathrm{c_s}\Omega_{\mathrm{k}}}{\pi \mathrm{G}\Sigma} = \left(\frac{\mathrm{c_s}}{\mathrm{v_k}}\right)\left(\frac{\mathrm{M}^*_{\mathrm{disk}}}{\mathrm{M}_*}\right)^{-1} \tag{2.3}$$

When we consider magnetic fields, these also work as a stabiliser in terms of the collapse. The strongest stabilisation in terms of magnetic fields comes when the magnetic field lines are perpendicular to the disk, and in this case the magnetic pressure can actually completely suppress the instability. However, if the instability is not completely suppressed, the collapse will still go on, i.e. if gravity is strong enough so that the collapse can happen, it will happen, and the minimum scale at which this occurs is still defined by the BE mass as seen in Eq. 2.2 (Richard B Larson 2003)

In molecular clouds we observe turbulence as the internal motion of the cloud. This is supersonic on all but the smallest scales, where it is subsonic. This means that we will have Mach numbers, $\mathcal{M}$, larger than 1, i.e. the speed of the waves causing the internal motion is greater than the speed of sound in the medium.

$$\mathcal{M} = \frac{|\mathbf{v}|}{\mathrm{c_s}} \tag{2.4}$$

Since we have Mach numbers greater than 1 we will also have shock waves that compress the gas by a factor equal to $\mathcal{M}^2$, and with Mach numbers usually around 5-10, this means we get up to a two order of magnitude compression. These shocks help create the variation in density that aids in initiating gravitational collapse, and so it is a crucial factor in star formation. When we look at smaller cloud cores in the beginning of a collapse, the turbulence is subsonic and the structures are more smooth and regular, meaning shocks are not creating variations of density in the cores themselves (Richard B Larson 2003).

Now we understand some of the processes behind the collapse and conditions for the collapse, we can take a look at the collapse itself. We will look at a spherical collapse, a collapse with rotation, and finally a collapse with a magnetic field.

2.3.1 Spherical Collapse

In a spherical collapse the temperature stays about the same, even when density increases by many orders of magnitude due to both the thermal coupling with dust at higher densities and the atomic and molecular cooling at lower densities. The temperature in a prestellar core is typically around 6-12 K as long as the density is less then around 10^{10} H_2 cm^{-3} (Richard B Larson 2003). Most calculations assume isothermal collapse and a temperature of 10 K, which is typically a good approximation but not always enough. Boundary conditions are not that important for the collapse itself, as despite the type of boundary conditions the collapse is highly non-uniform and is characterised by runaway growth of a central density peak, called an inside-out collapse.. When there is no pressure gradient present, the collapse occurs in a free-fall time t_{ff} defined as the time required to collapse to infinite density from a state of rest and also shown in Eq. 2.5 (L. Spitzer 1978). When there is an outward facing pressure gradient, the collapse is decelerated, but is still approximately a free-fall time. Both observations and numerical simulations show that the collapse approaches a density distribution $\rho \propto r^{-2}$ as long as the isothermal assumptions holds. A major implication of this is that a very small amount of the mass gets to the densities required to form a star where the rest of the core remains as an infalling envelope. This mass obtains hydrostatic equilibrium with heating and at this point we call it the first hydrostatic core. This also results in the rotation being amplified and bipolar outflows starting to appear, by when the core will have transitioned into the second hydrostatic core, which we call a protostar (R. B. Larson 1969). The envelope remains around the protostar and will either be accreted in later stages of the star formation process or blown away by outflows. The star can be represented as a singularity in the density distribution and it is expected to get almost all of its mass from the accretion process (Richard B Larson 2003).

$$t_{ff} = \sqrt{\frac{3\pi}{32G\rho}} \tag{2.5}$$

2.3.2 Collapse with Rotation

Most star-forming clouds are observed to be rotating which is expected due to their internal motion (turbulence), and we also expect this rotation to strongly affect the collapse if angular momentum is conserved, as we know it is. The angular momentum in the cloud is much too great for a star, even if it rotates at its breakup speed, and so angular momentum cannot be completely conserved. This means that we expect some loss or redistribution of angular momentum. Magnetic fields can dispose of some of the angular momentum, but not close to the amount leftover in this case. In most cases the collapse would result in a binary or multiple system of stars whose orbital motions can account for much of the angular momentum in the overall system (Richard B Larson 2003; Schulz 2012). It is thought that one of the main processes by which angular momentum is transported, and thus this dilemma is solved, is by the outflows which we will come back to in section 2.4.3.

An important conclusion is that rotation does not prevent formation of a density singularity (protostar), that evolves in a qualitatively similar way as the case that is not rotating, as long as the collapse remains isothermal. The main difference is that the mass ends up in a centrifugally supported disk around the protostar, and this disk is predicted to become unstable when $Q < 1$ for all cases (Richard B Larson 2003).

2.3.3 Collapse with Magnetic Fields

Magnetic fields were thought to be important, so historically a lot of modelling has gone into the ambipolar diffusion collapse. This is about an order of magnitude longer timescale than the free-fall time. When the cloud contracts it gets flattened along the field lines and eventually gravity becomes strong enough to overcome the magnetic support and a runaway collapse will start. Because of the flattening, the collapse velocity is a bit smaller than the non-magnetic case and its maximum is about the same as the sound speed (Richard B Larson 2003).

However, further studies suggest that turbulence may play a much more important role than magnetic fields in supporting cloud cores against gravitational collapse, and that the collapse is more likely to be started from dissipation of turbulence than by ambipolar diffusion (Nakano 1998). Magnetic fields are generally less important throughout the collapse, and mostly serve to slow down the collapse compared to the case where there is no magnetic field. Once again, as a collapse begins, the collapse will look similar to the other cases we described with a density distribution approaching the

BE sphere (Richard B Larson 2003).

2.4 Protostellar Evolution

Proceeding from the gravitational collapse, the next step is to consider what happens after a cloud starts collapsing, which is the formation of one or more protostars. We will not be going into details with the binary or multiple star systems, but mention them where relevant.

A protostar is the next step of the stellar evolution going from a molecular cloud to a fully formed star. As mentioned previously, once the cloud transitions into a prestellar core that then starts heating and collapsing into both the first and then the second hydrostatic core, we start calling this a protostar, but only until the onset of nucleosynthesis, at which point it becomes a star, and we start classifying it as such like in Fig. 2.1 (R. B. Larson 1969; Richard B Larson 2003; Schulz 2012).

In the process of protostellar evolution there are three main parts that we will focus on, the first being the formation and impact of protoplanetary disks, the second being how the protostar grows, i.e. accretes matter, and finally we will look at jets and outflows. These are all visualised in Fig. 2.3 which is a sketch of the protostellar system L1527, that was also recently imaged by JWST's NIRCam (see Fig. 2.4).

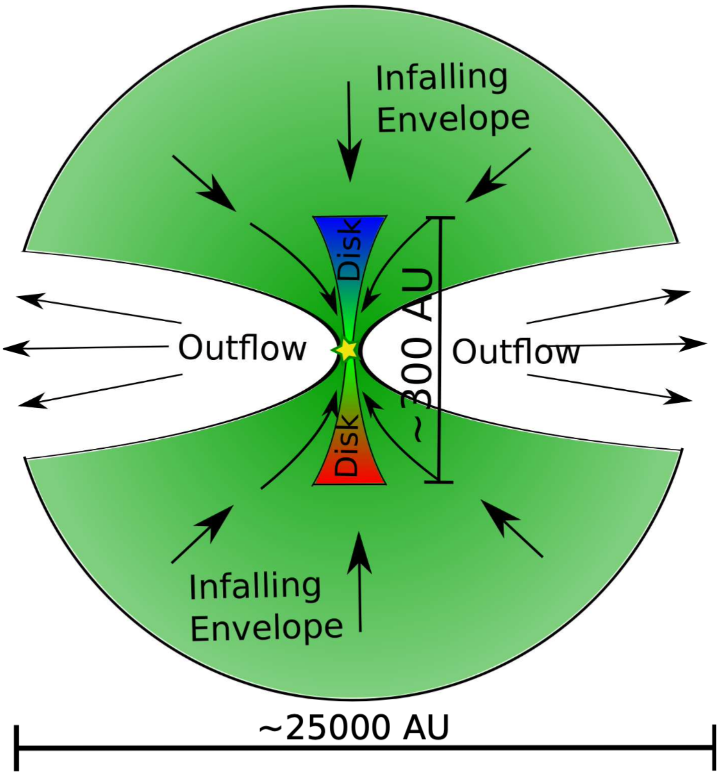

Figure 2.3: Sketch of a protostellar system, specifically of the protostar L1527, by (Tobin et al. 2012)

Figure 2.4: Picture of L1527 by JWST's NIRCam. **Credits:** NASA, ESA, CSA, and STScI. **Image processing:** J. DePasquale, A. Pagan, and A. Koekemoer (STScI)

2.4.1 Protoplanetary Disks

Historically there are two classical problems of star formation, the angular momentum problem and the magnetic flux problem. Here we will focus on the angular momentum problem. This essentially means that a star has far less angular momentum and magnetic flux than an area of the same mass in the ISM, and we do not fully know how this works. We know that the magnetic fields can remove angular momentum quite effectively, under two conditions, namely that the contraction of the core is sub-Alfvénic and the infalling gas consists of well coupled neutral and ionised parts (Mestel and J. Spitzer L. 1956; Mouschovias 1987). When either of these conditions break, the gas will start to collapse with an almost constant specific angular momentum, if the transport of angular momentum done by turbulence and gravity is insignificant. This results in a disk being formed of size $\mathrm{R_d}$ given by Eq. 2.6, where Ω_0 is the initial angular velocity, $\bar{\omega}_0$ is the initial cylindrical radius, and $\mathrm{M_{*d}}$ is the combined mass of the star and disk (McKee and Ostriker 2007).

$$\mathrm{R_d} = \frac{\Omega_0^2 \bar{\omega}_0^4}{\mathrm{GM_{*d}}} \tag{2.6}$$

The disk form because there is a rotationally supported core, which we see in almost all real systems, and conservation of angular momentum during the collapse itself (Richard B Larson 2003; McKee and Ostriker 2007). When looking at the stability of the system with a rotationally supported disk, we can use Q from Eq. 2.3 to see that when the central mass is small compared to the mass of the disk then it gets increasingly unstable leading to further collapse, rather than a stable system.

So far we have looked at disks purely in the rotational regime. Now we will consider the magnetic fields, where early studies of disk formation assume that magnetic fields are well coupled to the bulk neutral gas, and as the gravitational collapse continues, the magnetic field is dragged inwards and pinches the magnetic field. This results in a flattened equatorial region in a pseudo disk-like structure. It also results in a strong magnetic torque that transports most of the angular momentum away from the disk-like structure and brakes the rotation. When there is then no rotational support the collapse continues without forming actual disks that we can compare with observations. This is called the magnetic braking catastrophe in the ideal MHD limit. It is most severe in the axisymmetric case when the magnetic field and rotation is aligned. Either introducing magnetic field misalignment or turbulence can help reduce the severity of the problem. This leads to introducing three overall concepts from non-ideal MHD that we need to consider. These are Ohmic dissipation, Ambipolar diffusion, and the Hall effect. Ohmic dissipation is a diffusive effect that dissipates the total electric current and so weakens the electromotive force. Ambipolar diffusion is another diffusive process which allows the bulk neutral gas to drift relative to the charged parts of the gas which are coupled to the magnetic field. Since the neutral part of the gas exerts a drag force on the charged parts of the gas, the net effect of ambipolar diffusion is to reduce the tendency to bend the magnetic field lines. Unlike Ohmic dissipation and ambipolar diffusion the Hall effect is a dispersive process. The Hall effect can drift the pinched magnetic field lines from the magnetic braking cases along the azimuthal direction, which result in magnetic tension directed in the azimuthal direction, which can either spin up or down the neutral gas in the same direction, depending on the orientation of the magnetic field with respect to the rotation axis (Zhao et al. 2020).

2.4.2 Accretion

Spherical Accretion

Spherical accretion with no rotation or magnetic fields present is a fairly simple problem, since thermal pressure is the only force opposing gravity and is important mainly in outermost part of the envelope, which we can approximate as roughly isothermal. We can further simplify this by considering the protostar as a point mass as in SIS in section 2.3 (Shu 1977). This leads to an accretion rate depending only on a numerical constant ϕ_{in} of order one, the isothermal sound speed and G (McKee and Ostriker 2007):

$$\dot{\mathrm{M}}_{\mathrm{in}} = \phi_{\mathrm{in}} \frac{\mathrm{c}_{\mathrm{s}}^3}{\mathrm{G}} \tag{2.7}$$

This is useful as a standard solution, but has been shown to mostly approximate the slower accretion rates as other solutions give an accretion rate about 50 times higher. The accretion rate also drops rapidly over time. The protostar typically accretes very rapidly for about 10^4 years, then accretes about half of the envelope on 10^5 years, and nearly all of the envelope in 10^6 years (Richard B Larson 2003; McKee and Ostriker 2007).

If we were to introduce magnetic fields or rotation in this scenario, then we get similar accretion rates, just by varying the numerical constant. Furthermore, we get a faster decrease in accretion rate over time compared to the previous solutions (Basu 1998; Richard B Larson 2003; Matsumoto et

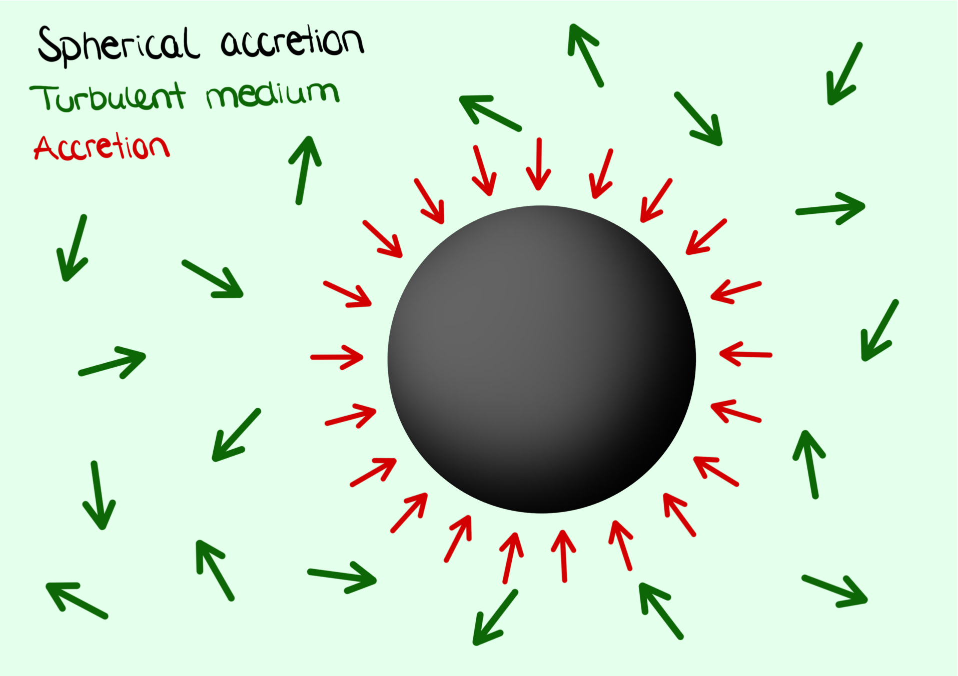

Figure 2.5: Sketch of spherical accretion in a turbulent medium, where the black circle symbolises a Bonnor-Ebert sphere, the green is the turbulent medium, and the red arrows shows the accreting matter onto the sphere. Drawn by Martine Lützen.

al. 1997; Saigo and Hanawa 1998; Tomisaka 1996). Further, if we introduce turbulence we get a scenario like sketched in Fig. 2.5, which compares better to the less ideal scenarios used in this project. In this sketch the accretion of matter is signified by the direction and size of the red arrows, and as we can see it is spherically symmetric like defined above. We can still quite reasonably use spherical accretion as an approximation with turbulence by simply adjusting ϕ_{in} appropriately.

Throughout the accretion phase, the central protostar remains mostly hidden by dust in the envelope and it is not until it has accreted almost all the mass that we can observe it directly. It is however possible with interferometers to look through dust and gas and obtain maps of the (projected) matter distribution. Transitional lines from molecules further allow to constrain chemical abundances, temperatures, and the kinematic structure in the vicinity of the protostar. This can be done with e.g. with ALMA, due to the longer wavelengths probed by interferometers. This also means that it is a good assumption that once we can see a star at visual wavelengths, it has accreted most, if not all, of the matter around it that it will accrete in its formation (Hartmann 1998).

Bondi-Hoyle Accretion

Since (Bondi 1952; Hoyle and Lyttleton 1939) the Bondi-Hoyle accretion has been the primary method of calculating and modelling accretion for a compact object travelling through the ISM, rather than being stationary like spherical accretion above. In real world cases there is likely some motion through the ISM rather than the object being fully stationary, which is one of the reasons why this has been used as a good approximation for so many years. The accretion method is described by Eq. 2.8

$$\dot{\mathrm{M}}_{\mathrm{BH}} = 4\pi\rho_\infty \mathrm{G}^2\mathrm{M}^2\mathrm{c}_\infty^{-3}\left[\frac{\lambda^2+\mathcal{M}^2}{(1+\mathcal{M}^4)}\right]^{1/2} \tag{2.8}$$

which was written in this way by (Ruffert 1994; Ruffert and Arnett 1994). This gives us the accretion rate as a function of $\mathcal{M}$, the Mach number, the sound speed c_∞ far from the star, density ρ_∞ far from the star, and a number of order unit, λ, which also depends on $\mathcal{M}$. In an isothermal medium, which is often assumed at least for part of the star formation process, $\lambda = 0.25\ \mathrm{e}^{1.5} \approx 1.1$ (Krumholz et al. 2005). Furthermore, the characteristic radius at which the compact object accretes from is defined by Eq. 2.9 (McKee and Ostriker 2007). The setup is visualised in a sketch in Fig. 2.6, where it has been sketched in a turbulent medium, as it is more appropriate to this project than an ideal setup. Here we have the compact object moving to the left in the figure, and so accreting the most in the direction that it is moving, which is symbolised by the direction and size of the red arrows. Bondi-Hoyle accretion is still a great way to compare better accretion models to a simplified case that is not just spherical accretion, which we know is a highly idealised case.

$$\mathrm{R}_{\mathrm{BH}} = \frac{\mathrm{GM}}{(1+\mathcal{M}^2)\mathrm{c}_\mathrm{s}^2} \tag{2.9}$$

Accretion from Disks

We know that there is some process(es) that accrete matter from the disks onto the stars. However, it is still an open research question what processes might be responsible for this and how they work. One of the proposed processes is magnetospheric accretion, which works only for magnetised stars that have a magnetosphere (Romanova and Owocki 2016).

Magnetospheric accretion is a very complex process that depend on many factors, like the period of stellar rotation, the magnetic field structure, the

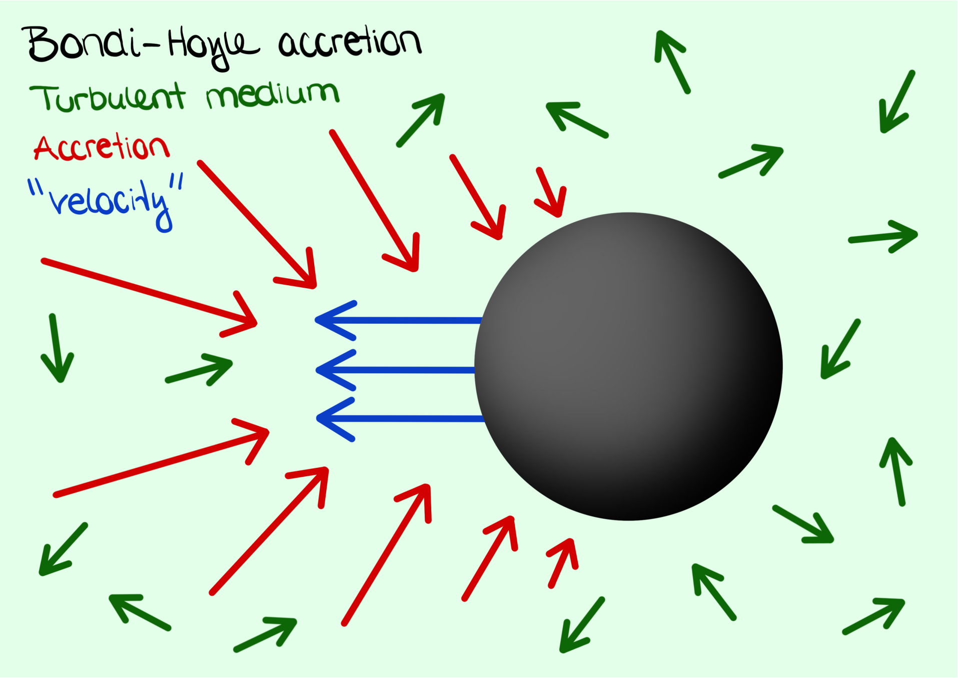

Figure 2.6: Sketch of Bondi-Hoyle accretion in a turbulent medium, where the black circle symbolises a Bonnor-Ebert sphere, the green is the turbulent medium, the red arrows shows the accreting matter onto the sphere, and the blue arrows shows the motion of the sphere. Drawn by Martine Lützen.

size of the magnetosphere, the diffusivity at the boundary of the disk and magnetosphere, properties of the disk, and more. Here we will only give a brief overview of the process, mainly related to the interaction between the magnetosphere and the disk. Theoretically it has been predicted by e.g. (Pringle and Rees 1972) that the inner part of the disk will be truncated by the magnetosphere at radius, $\mathrm{r_m}$, given by Eq. 2.10 where $\mu = \mathrm{B_{star}R^3_{star}}$ is the magnetic moment of the star with a surface field of $\mathrm{B_{star}}$, and $\dot{\mathrm{M}}$ is the accretion rate of the disk. It is then predicted that matter flows above and below the magnetosphere in a funnelled flow onto the star. This has both been simulated and observed to occur but it is not clear if it applies generally or only to rotating magnetised stars (Romanova and Owocki 2016).

$$\mathrm{r_m} = \mathrm{k}\left(\frac{\mu^4}{\dot{\mathrm{M}}^2\mathrm{GM_{star}}}\right)^{1/7}, \qquad \mathrm{k} \sim 1 \tag{2.10}$$

While the above formula only give a good estimate for where the disk should be truncated, it remains open to generalise this, or find other processes that describe the flow of matter from disks onto stars.

2.4.3 Outflows

Generally outflows are characterised as either winds or jets. In literature it is loosely defined, but jets are typically fast and highly collimated whereas winds are much slower and less collimated. In Fig. 2.3 the arrows, in particular the middle arrow, can be thought to represent jets, and the extended white outflow region represents winds. Usual velocities for jets are about 100-1000 km/s where for winds they are about 1-30 km/s (Lesur et al. 2022).

There are two main types of outflows, thermally driven and magnetically driven. Historically, the thermally driven outflows were thought to be most important, but the magnetised outflow scenario has gained traction again as there is no systematic process to drive turbulence, which was proposed as an idea by (Wardle and Koenigl 1993) and further developed by (Königl et al. 2010; Salmeron et al. 2011). It is also likely that winds could be both magnetic and thermally driven rather than one or the other. (Rodenkirch et al. 2020) showed that this is both possible and likely to exist as a result of simulations matching observations (Lesur et al. 2022).

The rate of mass loss from winds can be compared to the mass accretion rate in a steady state scenario with constant efficiency ϵ for a disk with inner radius $\mathrm{R_{in}}$ and outer radius $\mathrm{R_{out}}$ by Eq. 2.11 where for most cases we expect $\dot{\mathrm{M}}_{\mathrm{wind}} \sim \dot{\mathrm{M}}_{\mathrm{acc}}$ based on simulations and observations.

$$\dot{\mathrm{M}}_{\mathrm{wind}} = \dot{\mathrm{M}}_{\mathrm{acc}}(\mathrm{R_{in}}) \left(\left(\frac{\mathrm{R_{out}}}{\mathrm{R_{in}}} \right)^{\epsilon} - 1 \right) \tag{2.11}$$

Disk outflows have been observed through emission lines, and it is still an area that receives a lot of attention. However, there is still a lot that we don't know, in particular the relative occurrence of magnetohydrodynamics (MHD) driven winds and thermally driven winds. In the future we will likely get more knowledgeable about this and all the other open questions with more observations from ALMA, new proposed techniques, and next generation radio telescopes like the ngVLA (next generation Very Large Array) (Lesur et al. 2022).

In numerical models the extent to which winds and jets are captured in the models depends sensitively on the numerical resolution. The reason for that is that jets are sourced very close to the central object, and therefore require resolutions down to tens of stellar radii. Winds are more amenable to numerical modelling , but with significant contributions in the mass flow from the inner disk, still requires a significant numerical effort. Ideally, we would like to study the numerical convergence of our accretion recipes employing different numerical resolutions, but the resolution.dependent outflow-efficiency makes any results non-trivial to interpret. E.g. a perfect accretion recipe that captures exactly how much material is accreted to the central object independent of resolution (below a certain cell size) will still show non-convergence because at varying resolutions the amount of outflow will vary.

Chapter 3

Methods

The methods used in this project can be split into methods applied to modelling star formation in general, the specific code, RAMSES, that we use, a more in depth look at how our sink particles work, and finally the analysis tools developed as part of this project. In this chapter we will go through describing each of these in the order they are listed above.

3.1 Modelling Star Formation

3.1.1 Magnetohydrodynamics

A continuous description based on statistical average using fluid dynamics is well suited for describing the ISM. The media can be ionised and conducting, i.e. plasma, which means that it can interact with magnetic fields (Bodenheimer et al. 2007). These interactions have a large impact on the evolution of ISM and star formation, and so we adopt MHD, which is an extension to fluid dynamics where we take magnetic fields into account using Maxwell's equations to derive the standard MHD equations in Eq. 3.1 which is written in the conservative form (Fromang et al. 2006) useful when using the finite volume method. Here we have also added the Poisson equation as a 5th equation since it will be used to calculate and describe the gravitational force of the system as described below in section 3.1.4.

$$
\begin{aligned}
&\frac{\partial \rho}{\partial \mathrm{t}} + \nabla \cdot (\rho \mathbf{v}) = 0 \\
&\frac{\partial \rho \mathbf{v}}{\partial \mathrm{t}} + \nabla \cdot (\rho \mathbf{v}\mathbf{v} - \mathbf{B}\mathbf{B}) + \nabla \mathrm{P}_{\mathrm{tot}} = -\rho \nabla \Phi \\
&\frac{\partial \mathrm{E}}{\partial \mathrm{t}} + \nabla \cdot [(\mathrm{E} + \mathrm{P}_{\mathrm{tot}})\, \mathbf{v} - \mathbf{B}(\mathbf{B} \cdot \mathbf{v})] = -\rho \mathbf{v} \nabla \Phi \\
&\frac{\partial \mathbf{B}}{\partial \mathrm{t}} + \nabla \cdot (\mathbf{v}\mathbf{B} - \mathbf{B}\mathbf{v}) = 0 \\
&\nabla^2 \Phi = 4\pi \mathrm{G} \rho_{\mathrm{tot}}
\end{aligned}
\tag{3.1}
$$

Here ρ is the density of the fluid, ρ_{tot} is the total density, i.e. $\rho_{\mathrm{tot}} = \rho_{\mathrm{gas}} + \rho_{\mathrm{sink}}$, $\mathbf{B}$ is the magnetic field, $\mathrm{P}_{\mathrm{tot}}$ is the sum of the thermal and magnetic pressure given by Eq. 3.2,

$$
\mathrm{P}_{\mathrm{tot}} = \mathrm{P}_{\mathrm{therm}} + \frac{\mathbf{B} \cdot \mathbf{B}}{2} \tag{3.2}
$$

E is the total energy density of the fluid, given by Eq. 3.3 where ε is the internal energy density (Fromang et al. 2006).

$$
\mathrm{E} = \varepsilon + \rho \frac{\mathbf{v} \cdot \mathbf{v}}{2} + \frac{\mathbf{B} \cdot \mathbf{B}}{2} \tag{3.3}
$$

and finally Φ is the total gravitational potential as determined by the Poisson equation, the 5th equation in Eq. 3.1.

The thermal pressure is given by the equation of state, which is usually assumed to be adiabatic, of the form $\mathrm{P}_{\mathrm{therm}} = (\gamma - 1)\varepsilon$, where γ is the adiabatic index. Finally, in order for the MHD equations to be satisfied at all times, the solenoidal constraint $\nabla \cdot \mathbf{B} = 0$ at all times (Fromang et al. 2006).

3.1.2 Finite Volume Method / numerical conservation of quantities

In physics we generally have conserved quantities like energy, mass, and momentum. When we simulate this we need to take care that these quantities are numerically conserved as well. When writing Eq's. 3.1 in the differential and conservative form like above, then we can take the volume integral to get the conserved quantities and apply Gauss' theorem which gives us the

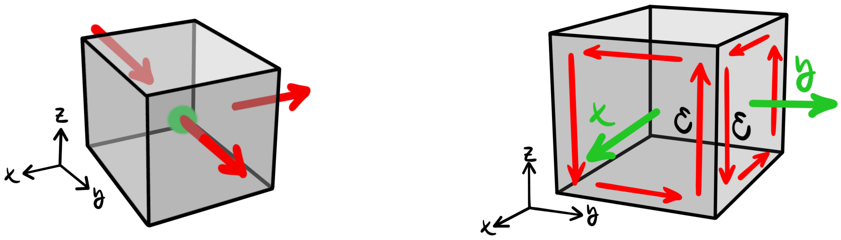

(a) Finite Volume Method (b) Constrained Transport

Figure 3.1: The two sketches are examples of finite volume method and constrained transport method, where only some fluxes are drawn for simplicity, but it applies to all interfaces. On the left, the red arrows symbolises the flux going in and out of a cell, with the green dot being the centre of the cell. On the right the green arrows symbolises the direction of magnetic field components and the red arrows is the electromotive force determined by the right hand rule. As can be seen this cancel out for each edge upholding the solenoidal constraint when summed over the entire cell. Drawn by Martine Lützen.

flux through a surface and a source term. By applying the fact that the quantities are conserved we know that any change is either an effect of the source term or from flux, where if it is the flux, then the flux going out to neighbouring cells must be equal to the incoming flux from the neighbouring cells. Due to the volume integral over cells, we call this Finite Volume Method (FVM) and it explicitly respects the conservation laws from the physics we are simulating. We visualise FVM with example fluxes in Fig. 3.1a. The fluxes drawn are chosen for simplicity, but the idea of the sketch applies to fluxes through all surfaces. It is important to note that the energy in 3.1 is the total energy, as that is what is conserved and we are not interested in the transitions between types of energy, just the total energy (Fromang et al. 2006; Toro 2009).

The FVM does not apply to the magnetic field, but magnetic field flux is also a conserved quantity, represented by the solenoidal constraint, $\nabla \cdot \mathbf{B} = 0$, mentioned in the previous section. For magnetic field flux we instead use the method Constrained Transport (CT), which works similarly to FVM, but applying Stokes' theorem instead of Gauss' theorem, and we get a line integral that tells us how the electromotive force (EMF) is pointing around the interface of cells, like in Fig. 3.1b where only the positive x- and y-components are visualised for simplicity. The idea of CT is to place magnetic components on the interface and update the flux according to the EMF along the edges, which guarantees the conservation of $\nabla \cdot \mathbf{B} = 0$ to numerical roundoff (Fromang et al. 2006; Toro 2009).

The general type of algorithm used to solve FVM and CT is a Godunov scheme, the specific one we will use, and hence describe, is the MUSCL method, which is also one of the most commonly used ones. It works by taking the state at the centre of the cell, q, and interpolating over time and the slope to get the state at the interface between two cells (Toro 2009). This is shown in Fig. 3.2 for left cell $-$ and right cell $+$.

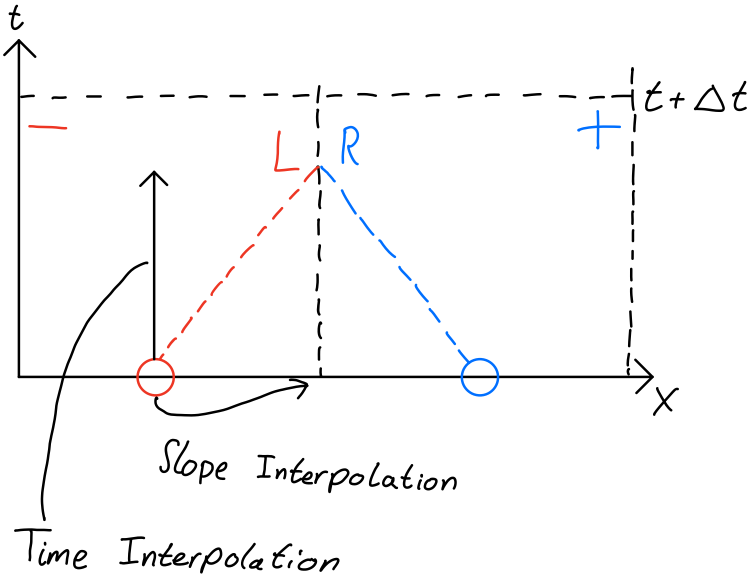

Figure 3.2: Diagram showing the principles of the MUSCL method, which interpolates quantities from the cell centre of the - and + cell to the interface from the left and right at a time t + Δt, shown by their respective symbols.

$$
\begin{aligned}
q_L &= q^{-}_{\text{center}} + \left.\frac{\Delta q}{\Delta x}\right|^{-} \times \frac{1}{2}\Delta x + \left.\frac{\Delta q}{\Delta t}\right|^{-} \times \frac{1}{2}\Delta t \\
q_R &= q^{+}_{\text{center}} + \left.\frac{\Delta q}{\Delta x}\right|^{+} \times \frac{1}{2}\Delta x + \left.\frac{\Delta q}{\Delta t}\right|^{+} \times \frac{1}{2}\Delta t
\end{aligned}
\tag{3.4}
$$

The interpolation is done by first order Taylor expansion with Eqs. 3.1.2 for both time and space. The quantity q represents any quantity of the cell that we want to interpolate to the interface. We calculate the slope $\frac{\Delta q}{\Delta x}$ with a monoticity preserving slope interpolation like moncen or minmod for stability. We then use q_L and q_R as inputs for a Riemann solver, where the Riemann solvers of choice here are LLF, HLL, and HLLD (Fromang et al. 2006; Toro 2009).

3.1.3 Sink Particles

When modelling star formation, there is simply not enough computational power and time to model the ISM, the collapsing core, the protoplanetary disk, and the stellar structure, because it covers so many orders of magnitude. Furthermore, the region of the protostar becomes so dense in comparison that it dominates the time taken for each computational step and can make it so short that it is not feasible to simulate further than a few kyr after the star has formed, and in some cases much less. To get around this problem, when the collapsing core gets dense enough, we represent the forming star with a point particle that we call a sink particle, first used for star formation simulations by (Bate et al. 1995). A big trade-off is that we will no longer simulate the internal structure and evolution of the protostar, however, this allows us to simulate the entire system for much longer for the same computational and time costs.

The algorithm used in this project is the one of (Haugbølle 2018) and since it is central to this project it has a standalone chapter 4 and it will be described there.

3.1.4 Gravity

There are several different ways of modelling gravity in astrophysical simulations and they mostly differ in how they calculate the gravitational potential of both the gas and the sink particles. Here we adopt the method used by(Haugbølle 2018), which is developed to be a scalable way to have accurate orbits for global star forming simulations.

The two methods in (Haugbølle 2018) are based on interpolation over 8 (CSC) neighbours or 27 neighbours (TSC). They use the combined density of the gas and sink particles in order to solve the Poisson equation (Eq. 3.1 number 5) for the combined gravitational potential $\Phi_{\text{gas+sink}}$. The first of the two methods then uses a matching CSC or TSC interpolation of the gradients of $\Phi_{\text{gas+sink}}$ to the sink particle's position in order to find the gravitational potential on the sink particle. For the second method, when computing $\Phi_{\text{gas+sink}}$ they only update the gas, and then solve the Poisson equation a second time using only the gas as input to get Φ_{gas} which allows them to directly compute the gravitational acceleration of the gas on the sink particles. The gravitational force of the sink particles is computed as the sum over the sink particles. For both methods when computing the gravitational force between the sink particles, a cubic spline is used to soften the function of the gravitational force.

For both methods it is true that they are scalable to thousands of sink particles. In simulations that have many multiple-star systems the second method is superior. With a direct N-body integration of the star-star force it is possible to obtain precise orbits even for stars that are separated with less than a single computational cell. This method is crucial to give a realistic simulation of a star forming region. The cost of this scalability is to solve the Poisson equation one more time than other methods. For this project we are exclusively using the second method.

3.2 RAMSES

There are many numerical codes for simulating star formation like Flash (Fryxell et al. 2000), Enzo (Bryan et al. 2014), Gizmo (Hopkins 2015), Arepo (Springel 2010), and Gasolin (Wadsley et al. 2017), but for this project we will be using the code RAMSES originally published by (Teyssier 2002) and updated in (Fromang et al. 2006). RAMSES was initially developed to study the large structures of the universe and galaxy formation, but has since then found its use in studying star formation and the evolution systems spanning many orders of magnitude. Initially it only solved the fluid dynamics of the astrophysics simulations and was unable to include magnetic fields (Teyssier 2002), but with the major update in (Fromang et al. 2006) it was extended to be able to solve the MHD equations in Eqs. 3.1, and so include magnetic fields which we have seen are important. Below we will describe some of the components that makes it work well for large astrophysics simulations and how to zoom-in on a smaller section of these large simulations.

3.2.1 Adaptive Mesh Refinement

RAMSES uses Adaptive Mesh Refinement (AMR) in order to increase resolution in areas of interest, but keep the areas of low interest at a lower resolution to optimise the use of computing power. They use a fundamental data structure called a "Fully Threaded Tree" (FTT) (Khokhlov 1998), which is different to other AMR methods, like patch-based AMR (Teyssier 2002).

Instead of using singular cells as the basic elements of the simulations, they instead use a 2^{dim} group of cells called an *oct*, where we will use only 3 dimensions such that an oct is always 8 cells. We call the refinement levels ℓ and each oct belongs to one of them. The base grid for $\ell = 0$ is a regular Cartesian grid, but each subsequent level is not necessarily regular. We show an example of what octs look like in 3D in Fig. 3.3, where on the left we see the 3D placement of how one cell turns into an oct with 8 new cells for each level, and on the right we have the tree structure of one of these cells. In order to access octs when at a given level, all octs link to the next and previous octs of their given level, but also to the parent cell at $\ell - 1$, to the $2 \times \text{dim}$ neighbouring parent cells, and to the 2^{dim} child octs at $\ell + 1$. If a cell has no child oct it is called a leaf and if it does, it is called a split cell. In order to store the tree-structure for a 3D simulation, we need to store 17 integers per oct to have all the links stored (Teyssier 2002).

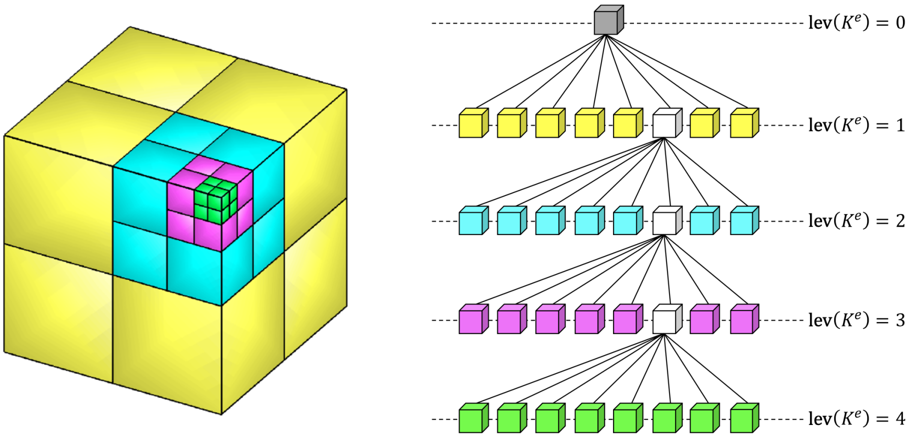

Figure 3.3: Schematic of how a 3D oct works when refining to the next level with the spatial representation on the left and the tree representation on the right. From (Nguyen et al. 2022)

The resolution of the simulation at the highest level in AU is given by $\Delta\text{x}(\ell_{\max}) = \frac{\text{boxlen}}{2^{\ell_{\max}}}$, where $\Delta x(\ell_{max})$ is the resolution and boxlen is the physical length of the box of the simulation in AU. Typically the length of the box is 1 pc which equals 206265 AU.

Refinement Criteria

Here we use the same criteria for refinement as in (Haugbølle 2018), which is based on overdensities. We refine when $\rho > \rho_{\max}(\ell)$, where $\rho_{\max}(\ell)$ is defined as the maximum density for a given level and it is written in Eq. 3.5. Here ρ_{levelmin} is the density of the minimum level, Δx is the cell size, and Δx_{min} is the cell size of the minimum level. This is done in such a way that $\lambda_{J,min}(ell)$, defined in Eq. 3.6, is proportional to the cell size so the number of Jean's lengths per cell size $\mathrm{L_J} = \frac{\lambda_\mathrm{J}}{\Delta \mathrm{x}}$ is independent of level.

$$\rho_{\text{max}} = \rho_{\text{levelmin}} \left(\frac{\Delta x(\ell)}{\Delta x_{\text{min}}} \right)^{-2} \tag{3.5}$$

$$\lambda_{\mathrm{J,min}}(\ell) = \sqrt{\frac{\pi \mathrm{c}_\mathrm{s}^2}{\mathrm{G}\rho_{\text{max}}}} = \sqrt{\frac{\pi \mathrm{c}_\mathrm{s}^2}{\mathrm{G}\rho_{\text{levelmin}}}} \left(\frac{\Delta \mathrm{x}(\ell)}{\Delta \mathrm{x}_{\text{min}}} \right) \tag{3.6}$$

Keeping $\mathrm{L_J}$ independent of level is the Truelove criteria (Truelove et al. 1997), where it is important to have at least 4 Jean's lengths per cell in order to resolve the astrophysics of the simulation. We use $\mathrm{L_J} = 8$ as a minimum to make sure everything is well resolved, and often we have $\mathrm{L_J} > 100$ (Haugbølle 2018). As long as the temperature and therefore the sound speed is kept the same in the simulation, or even other simulations, $\mathrm{L_J}$ is constant.

3.2.2 Zoom-In Runs

Simulations of star formation have often been that of an isolated BE-sphere that collapses in highly idealised models. These idealised cloud collapse models are useful for studying specific cases of star and disk formation, however, they don't incorporate the stellar environment, which has been shown to have a large influence for stars forming in Giant Molecular Clouds (GMC) and hence the models oversimplify the problem at hand. One way to get around this is to use Zoom-In simulations with the approach by (Kuffmeier 2017) which consists of two distinct steps.

The first step is to simulate a GMC with a lower refinement level, specifically they use up to $\ell = 16$ and a total of 9 levels. They use a box of 40 pc^3, but one could choose to use size in the range of about 5 - 200 pc. This box size gives a minimum cell size of $\sim$ 126 AU They also use a total mass of about 10^5 M$_\odot$, which could also be chosen in the range of about 10^3 to 10^3 M$_\odot$, where both of these ranges come from observations from e.g. (Murray 2011). They then evolve this simulation for 4 Myr.

The second step is the zoom-in step, where a selection of stars is picked to simulate at a much higher resolution, up to refinement level $\ell = 22$, which corresponds to a cell size of $\sim$ 2 AU. Once a star is picked, a new simulation

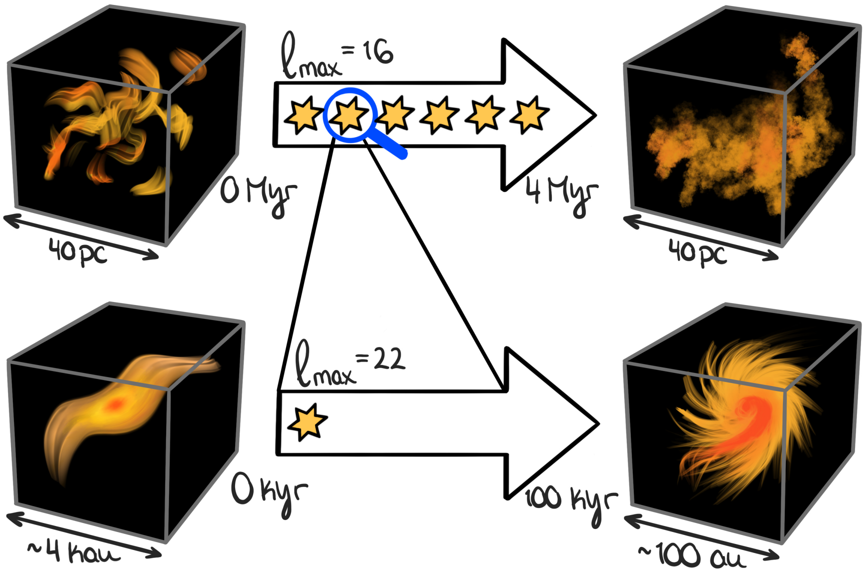

Figure 3.4: Sketch of the process of the zoom-in simulations. The first step is a larger low-resolution Giant Molecular Cloud simulation, where the second step zooms in on chosen stars at a much higher resolution. The sketch is inspired by Figure 1 in (Kuffmeier 2017) and drawn by Martine Lützen.

is started using the environment around that star, where the time between outputs has been changed to somewhere in the range 0.1 kyr – 0.5 kyr. Before the simulation is started, a velocity transformation is done to keep the star stationary in the new simulation box, which also simplifies analysis after the simulation. The simulation is started from a snapshot of the GMC simulation shortly before the star of interest formed. This is to avoid any clashes with changing the refinement levels and other aspects of the numerical nature of the simulation. The simulation is then evolved to about 100kyr to get a good understanding of the accretion of the star and the formation of disks around the star. Both steps of this process is visualised in the sketch in Fig. 3.4 (Kuffmeier 2017).

3.3 Analysis Tools

The following section describes the key analysis tools developed as part of this project. These are key to get a good and quick understanding of the simulations and comparisons between different versions of the simulation code. This is because we do idealised simulations as part of the testing to make sure that it works as intended, and so we know what to expect and therefore we can use these tools to quickly see and compare the expected outcome of important aspects of the simulations, like the mass accreted by the sink particles or the radial profiles of various quantities for each sink particle.

3.3.1 Accretion

The sink particle data is saved in a separate data file which makes it much less computer intensive to take a look at, and that is what we will take advantage of with this tool. Using a Python module, pyramses, developed by (Frimann et al. 2016), to make it easier to read the FORTRAN sink particle outputs from RAMSES, we read in the sink particle data into a Jupyter notebook and extract the mass of each sink particle as a function of time. Using this we can make plots for both the mass accreted for each sink particle and the total mass accreted in the simulation along with plots of the accretion rate, which is simply the mass accreted by a sink in each time step. These serve as a very important check to see that the simulation works as expected, since in our idealised simulations we know the approximate amount of mass available in the simulation and we have a good idea for how much of it should be accreted.

3.3.2 Radial Profiles

One of the best ways of looking at the regions around the sink particles is by looking at radial profiles of the following quantities for each of the sink particles:

- Density
- Integrated mass
- Sound speed
- Kepler speed
- Radial velocity
- Angular velocity
- Magnetic field in the z-direction

Using a quantity q and weight w we use the moments defined be Eq. 3.7 with $\alpha = 0,\ 1,$ and 2. We can then express the mean of q, $\bar{\mathrm{q}}$, and the standard deviation of q, σ_{q}, in terms of these moments as in Eq. 3.8 and 3.9 respectively.

$$\mathrm{z}^{\alpha}_{\mathrm{q,w}} = \int \mathrm{q}^{\alpha}\mathrm{dw} = \sum_{\mathrm{i}\ \in\ \mathrm{cells}} \Delta \mathrm{w_i} \mathrm{q_i^{\alpha}} \tag{3.7}$$

$$\bar{\mathrm{q}} = \frac{\sum \Delta \mathrm{wq}}{\sum \Delta \mathrm{w}} = \frac{\mathrm{z}_1}{\mathrm{z}_0} \tag{3.8}$$

$$\sigma^2_{\mathrm{q}} = \frac{\sum (\mathrm{q} - \bar{\mathrm{q}})^2 \mathrm{w}}{\sum \mathrm{w}} = \frac{\mathrm{z}_2}{\mathrm{z}_0} - \bar{\mathrm{q}}^2 \tag{3.9}$$

We use this method for all profiles except for the integrated mass, which is the cumulative sum of the binned mass, and Kepler speed, which is calculated directly with $\mathrm{v_K} = \sqrt{\frac{\mathrm{GM}}{\mathrm{r}}}$. The quantities and weights we use for each of the other profiles are shown in Table 3.1, and they are loaded into the code using the Python package Osyris (Vaytet 2022), which is a python package meant to accompany RAMSES, and then calculate all the profiles. We further overlay the accretion radius of the simulation by calculating it from the input file using Eq. 3.10, where max_distance multiplied by acc_fraction is the maximum number of cells away from a sink that it can accrete matter, unit_length is the conversion factor for numerical units to AU, and $2^{\ell_{max}}$ is the resolution in AU.

Table 3.1: Quantities and weights for the radial profiles

Profile	q	w
Density	ρ	V
Sound speed	$\mathrm{c_s}$	V
Magnetic field	$\mathrm{B_z}$	V
Radial velocity	$\mathrm{v_{radial}}$	m
Angular velocity	$\mathrm{v_{angular}}$	m

$$\mathrm{R_{acc}} = \frac{\mathrm{max\_distance} \cdot \mathrm{acc\_fraction} \cdot \mathrm{unit\_length}}{2^{\ell_{\mathrm{max}}}} \tag{3.10}$$

3.3.3 Spin

In section 4.0.2 is introduced the concept of spin of a protostar. The spin is important because it allows a measure of the rotation axis and the possibility of comparing it with the instantaneous distribution of angular momentum in the gas surrounding the protostar. As part of the project a new model for tracking the spin has been implemented in RAMSES. To investigate the results support for reading the spin components have been integrated in to the data analysis work-flow. The size of the spin does not carry relevant information, but the direction does, and related to this the corresponding spherical coordinates (ϕ, θ). Below we will use the spin components and plots of the spherical coordinates in a mollweide projection to better understand tempo and variation in how fast the stellar spin settles down during the accretion and formation process.

$$\begin{aligned} \theta &= \pi/2 - \arctan\left(\frac{\sqrt{S_x^2 + S_y^2}}{S_z}\right) \\ \phi &= \arctan\left(\frac{S_x}{S_y}\right) \end{aligned} \tag{3.11}$$

3.3.4 Movies

For the purpose of visualisation and getting a quick overview and understanding of each simulation, a small pipeline to create videos of the simulations was made. This is done by utilising Osyris once again. We load in the gas data and plot the logarithmic density centered either on a specific sink particle or the center of mass of the simulation. The spin vector is used to create three plots side by side of the x-, y-, z-direction of the sink particle. This is done a total of three times, one with just the logarithmic density and no overlay, one with the velocity field from the data overlaid as vectors, and one with the magnetic field from the data overlaid as streamlines. This is then repeated for each output from RAMSES and save all the plots. Finally, we use the module ffmpeg (Tomar 2006) to combine the plots into videos. Here it is worth noting that the pixel format must be set to **yuv420p** in order to view the videos as more than just black frames.

We came across a plotting artefact in Osyris where if the spin vector changes sign on one component, then the axes swap around in the plot itself. This is fixed by considering the spin vector of the previous output and call the same Osyris routine ”get_direction” which gives three direction vectors for plotting called ”normal”, ”pos_u”, and ”pos_v”. We then consider if Eq. 3.12 is true and if this is true, then ”pos_u” and ”pos_v” are swapped. We then consider if Eq. 3.13 is true and if it is then ”pos_u” swaps to ”-pos_u”. This conserves the direction of the plots when all the frames are plotted and so fixes the artefact.

$$|\mathbf{pos\_u} \cdot \mathbf{pos\_u}_{\mathrm{old}}| < |\mathbf{pos\_v} \cdot \mathbf{pos\_u}_{\mathrm{old}}| \tag{3.12}$$

$$\mathbf{pos\_u} \cdot \mathbf{pos\_u}_{\text{old}} < 0 \tag{3.13}$$

This pipeline is applied to each run and can even be executed for each run in parallel as the limiting factor is reading in the data and plotting it in Python, which can only use a single core. This means that using one core per run, it is possible to process as many runs as there are cores available.

Chapter 4

Accretion of Matter to Sink Particles

In this chapter an in-depth look at sink particles will be presented. They are the numerical sub-grid model for describing accreting stars. In past chapters the general methodology relevant for modelling star formation, the RAMSES code that has been used to obtain the results of this thesis, and the analysis tools have been introduced. This gives the needed background to consider the sink particles, and in the following sections we will describe what are the criteria for creating sink particles, and how they accrete mass, momentum, and spin from the surrounding material, along with how the accretion to binary systems with overlapping accretion radii is handled.

The algorithm for deciding when sink particles are created is the same as (Haugbølle 2018) which has the following steps.

1. Sink particles can only be created if the density in a cell is over a threshold density, $\rho_{\rm s}$, and is at the highest level of refinement for the simulation. Generally the cell is resolved with at least 2 Jean's lengths as described in 3.2.1, but often it is more. (Haugbølle 2018) finds that even under-resolving cells by a little does not affect the number of sink particles in a large scale simulation significantly.

2. The gravitational potential needs to be at a local minimum in the cell that forms a sink particle. They check this by calculating a smoothed average in a $2 \times 2 \times 2$ area and comparing with the neighbouring 26 cells, where the same smoothed average is calculated.

3. The velocity field needs to be converging in the cell forming the sink particle, i.e. $\nabla \cdot \mathbf{v} < 0$.

4. There can be no existing sink particle present within a distance we call the exclusion radius, $\mathrm{r_{ex}}$, to the cell that forms the new sink particle.

Sink particles created in this way are created with no mass initially but will immediately start accreting mass following the procedures described below.

4.0.1 Accretion of Mass and Momentum

Simply put, a sink particle can accrete matter from cells within the accretion radius, $\mathrm{r_{acc}}$, which we typically set to 1 to 2 Jean's lengths, and the cells need to have a density higher than the threshold ρ_{acc}. In order to avoid a high density build-up just outside the accretion radius, we make sure that $\rho_{\mathrm{acc}} \leq \rho_{\mathrm{s}}$. We also check the relative velocity of the sink and the gas in the cell in order to not artificially accrete unbound gas. If the relative velocity is less than $\sqrt{2}$ times the Kepler velocity, then we allow the gas to be accreted. We define the Kepler velocity of the sink as $\mathrm{v_K} = (\mathrm{Gm_{sink}/d})^{1/2}$, where d, is the distance between the centre of the cell and the nearest sink particle. The mass accretion rate, $\mathrm{\dot{m}_{gas}}$, in a time step $\Delta\mathrm{t}$ from a cell with density ρ is then given by Eq. 4.1 (Haugbølle 2018).

$$\mathrm{\dot{m}_{gas}} = \frac{\Delta \mathrm{m}}{\Delta \mathrm{t}} = \begin{cases} \alpha_{\mathrm{rate}}\ \mathrm{m_{cell} v_K \Delta x^{-1} f_v} & \text{if } \rho \leqslant \rho_{\mathrm{s}} \\ 0.5\mathrm{m_{cell}}\Delta \mathrm{t}^{-1} & \text{if } \rho > \rho_{\mathrm{s}} \end{cases} \tag{4.1}$$

Here $\Delta\mathrm{m}$ is the change in gas mass within a cell, ρ_{s} is used as a threshold density to prevent a large amount of gas building up faster than it can be accreted within the accretion radius, α_{rate} is a numerical accretion efficiency parameter that controls how efficient accretion is compared to the rotation, and it is typically set to 0.2. Finally $\mathrm{f_v}$ is a function that limits the accretion depending on the distance from the sink to the cell and the relative speed and it is given by

$$\mathrm{f_v} = \left[1 - \left(\frac{\mathrm{d}}{\mathrm{r_{acc}}}\right)^2\right] \times \begin{cases} 0 & \text{if } \mathrm{v} \geqslant \sqrt{2}\mathrm{v_K} \\ 2 - \left(\frac{\mathrm{v}}{\mathrm{v_K}}\right)^2 & \text{if } \mathrm{v_K} < \mathrm{v} < \sqrt{2}\mathrm{v_K} \\ 1 & \text{if } \mathrm{v} \leqslant \mathrm{v_K} \end{cases} \tag{4.2}$$

Once the accretion rate from a single cell in the model has been calculated, the accretion can be accounted for by removing the corresponding amount of mass, momentum, and thermal energy from the cell, and adding the mass and momentum to the sink particle. If we denote the updated quantities with a prime, the equations become

$$\begin{aligned} \text{mass:} \quad & m'_{\text{sink}} && = m_{\text{sink}} + \Delta m \\ \text{c.o.m.:} \quad & m'_{\text{sink}}\, \mathbf{r}'_{\text{sink}} && = m_{\text{sink}}\, \mathbf{r}_{\text{sink}} + \Delta m \mathbf{r}_{\text{cell}} \\ \text{momentum:} \quad & m'_{\text{sink}}\, \mathbf{v}'_{\text{sink}} && = m_{\text{sink}}\, \mathbf{v}_{\text{sink}} + \Delta m \mathbf{v}_{\text{cell}} \end{aligned} \tag{4.3}$$

where c.o.m. is the updated centre of mass of the sink particle; e.g. the change in the sink position due to the addition of the cell mass. Correspondingly, the cell quantities are adjusted as

$$\begin{aligned} \text{mass:} \quad & \rho'_{\text{cell}} && = \rho_{\text{cell}} - \Delta \mathrm{m}/\Delta \mathrm{V} \\ \text{momentum:} \quad & \mathrm{m}'_{\text{cell}}\, \mathbf{v}'_{\text{cell}} && = \mathrm{m}_{\text{cell}}\, \mathbf{v}_{\text{cell}} - \Delta \mathrm{m} \mathbf{v}_{\text{cell}} \\ \text{energy:} \quad & E'_{\text{tot}} && = \mathrm{E}'_{\text{therm}} + \mathrm{E}'_{\text{kin}} + \mathrm{E}_{\text{mag}} \\ & && = \tfrac{\rho-\Delta\rho}{\rho} \left[\mathrm{E}_{\text{therm}} + \mathrm{E}_{\text{kin}}\right] + \mathrm{E}_{\text{mag}} \end{aligned} \tag{4.4}$$

Here we note that the magnetic fields are not accreted, hence E_{mag} remains unchanged in the updating of E_{tot}. Exactly what happens with the magnetic fields during the accretion process is an unsolved problem. Most probably in nature there is a complicated combination of reconnection events and ohmic dissipation of magnetic energy, dragging of magnetic flux into the star and flux expulsion into the outflow. Nobody have yet found a good way to describe this numerically, except for adding resolution, and any numerical sub-grid model is further hampered by the complication of the solenoidal constraint making it impossible to arbitrarily decrease the magnetic flux e.g. in proportion to the accreted mass.

4.0.2 Spin

For this project we wanted to implement the tracking of the internal spin of the sink particles. In order to do this, we adapt Eq. 8 in (Federrath 2014), shown here in Eq. 4.5 for completeness. Specifically we are looking at the bottom 2 equations related to angular momentum and spin. Here primed quantities denote quantities after accretion.

$$\begin{aligned} \text{mass:} \quad & M'_{\text{sink}} && = M_{\text{sink}} + M_{\text{acc}} \\ \text{c.o.m.:} \quad & M'_{\text{sink}}\, \mathbf{R}'_{\text{sink}} && = M_{\text{sink}}\, \mathbf{R}_{\text{sink}} + M_{\text{acc}}\, \mathbf{R}_{\text{acc}} \\ \text{momentum:} \quad & M'_{\text{sink}}\, \mathbf{V}'_{\text{sink}} && = M_{\text{sink}}\, \mathbf{V}_{\text{sink}} + M_{\text{acc}}\, \mathbf{V}_{\text{acc}} \\ \text{ang.mom.:} \quad & \mathbf{L}'_{\text{sink}} && = M'_{\text{sink}}\, \mathbf{R}'_{\text{sink}} \times \mathbf{V}'_{\text{sink}} \\ \text{spin:} \quad & \mathbf{S}'_{\text{sink}} && = \mathbf{S}_{\text{sink}} + \mathbf{L}_{\text{sink}} - \mathbf{L}'_{\text{sink}} + \mathbf{L}_{\text{acc}} \end{aligned} \tag{4.5}$$

We adapt these equations to our code by rewriting them in terms of quantities we have in our code already, and more specifically we rewrite it in quantities before the accretion step. Firstly, we rewrite and simplify the angular momentum equation to Eq. 4.6.

$$\mathbf{L}_{\mathrm{sink}} - \mathbf{L}'_{\mathrm{sink}} + \mathbf{L}_{\mathrm{acc}} = \frac{\mathrm{m}_{\mathrm{sink}}\Delta\mathrm{m}}{\mathrm{m}_{\mathrm{sink}+\Delta\mathrm{m}}}(\mathbf{r}_{\mathrm{sink}} - \mathbf{r}_{\mathrm{cell}}) \times (\mathbf{v}_{\mathrm{sink}} - \mathbf{v}_{\mathrm{cell}}) \tag{4.6}$$

Where we have ensured that the distances are relative in order to not have an issue with periodic boundary conditions. Here $\Delta\mathrm{m} = \Delta\rho\Delta\mathrm{V}$ as in Eq. 4.1, since we calculate the mass in terms of densities and volume elements. For mathematical simplicity the rewritten equations contain mass, but in the code itself the mass is calculated for these steps from the density and volume elements. We then use this to update the equation for spin to Eq. 4.7.

$$\mathbf{S}'_{\mathrm{sink}} = \mathbf{S}_{\mathrm{sink}} + \frac{\mathrm{m}_{\mathrm{sink}}\Delta\mathrm{m}}{\mathrm{m}_{\mathrm{sink}} + \Delta\mathrm{m}}(\mathrm{r}_{\mathrm{sink}} - \mathrm{r}_{\mathrm{cell}}) \times (\mathrm{v}_{\mathrm{sink}} - \mathrm{v}_{\mathrm{cell}}) \tag{4.7}$$

This gives us the spin of each sink particle which we can use for our analyses described in the next section.

4.0.3 Accretion Recipes

In the current version of RAMSES the mass of a cell can only be accreted by the closest sink particle. This means that for binary or multiple systems, which we have many of, they take turns being the closest sink and so the accretion rate varies rapidly and not in a physical way. In order to give a more realistic accretion rate for binary systems we implement a new recipe for accreting matter which first checks for binary systems within $\mathrm{r}_{\mathrm{acc}}$ and then applies the recipe below to get a more physical accretion rate over the course of the simulation.

Preferential Binary Accretion

We consult the literature for more general preferential binary accretion not limited to stars and use this here as an attempt to give a good estimate of the accretion. We find that (Siwek et al. 2022) has done simulations of binary black holes with mass ratios of 0.1 to 1 for a variety of eccentricities shown in Fig. 4.1 and we also find that Eq. 1 in (Kelley et al. 2019) describes preferential accretion for active galactic nuclei. In order to cover mass ratios, q, between 0 and 1, we decide to combine Eq. 1 in (Kelley et al. 2019) with the data from (Siwek et al. 2022) at q = 0.1. We find that the term that dominates the equation is the second term, which is in Eq. 4.8:

$$\lambda(\mathrm{q_b}) = \frac{\mathrm{a_3}}{(\mathrm{a_4 q_b})^{\mathrm{a_5}} + (\mathrm{a_4 q_b})^{-\mathrm{a_5}}} \tag{4.8}$$

Where we are changing $\mathrm{a_4}$ to 10 instead of 12, to make the derivative 0 in our transition, even if the data from (Siwek et al. 2022) is not. This is because of λ going to 0 for q going to 0, as we know it should, and because it is the best comparable result in literature, since it has not been fully investigated in the case we are considering. We keep $\mathrm{a_3} = 50$ and $\mathrm{a_5} = 3.5$ for the fit, and the table created with the values goes to smaller q than Fig. 4.1, but the figure is limited for clarity as it is trivial to extend the left side all the way to $\mathrm{q} = 0$.

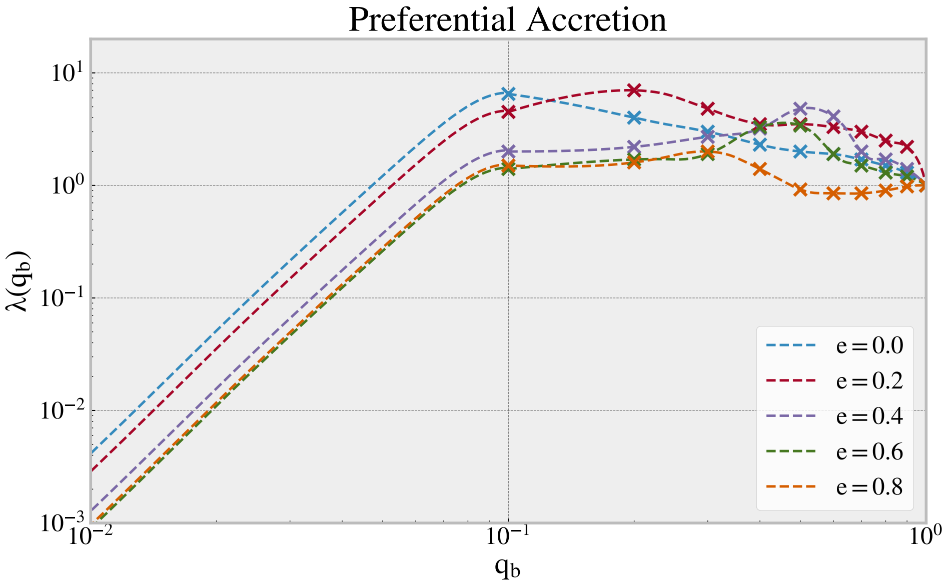

Figure 4.1: Plot of λ against the mass ratio of binaries. The data is merged from (Siwek et al. 2022) to the right of $\mathrm{q_b} = 0.1$ and Eq. 4.8 which is adapted from (Kelley et al. 2019). The left side of the plot continues to $\mathrm{q_b} = 0$, but has been cut off to get a better overall view of the data.

In order to implement this in our version of RAMSES, we modify the module that calculates the accretion onto stars. We modify it in such a way that if the flag *do_binary_accretion* is set to true in the input file, then we load in the table of the values in Fig. 4.1 and calculate the two nearest stars to a cell having mass being accreted from it. Then we calculate the total specific internal energy of the system as in Eq. 4.9 and check to see if the system is bound, i.e. if $\varepsilon < 0$, and if it is, then we calculate the eccentricity,e, with Eq. 4.10.

$$\varepsilon = \frac{1}{2}\mathrm{v}^2 - \frac{\mathrm{G}(\mathrm{m}_1 + \mathrm{m}_2)}{\mathrm{r}} \tag{4.9}$$

$$\mathrm{e} = \sqrt{1 + \frac{2\ \varepsilon\ \mathrm{h}^2}{\mathrm{G}(\mathrm{m}_1 + \mathrm{m}_2)}} \tag{4.10}$$

Here v is the relative speed of the stars, m_1 and m_2 are the masses of star 1 and 2 respectively, r is the distance between the stars, and h is the specific relative angular momentum. They can all be calculated based on quantities already existing in this part of the code. If the system is not bound we set the eccentricity to 0.8, which is the highest in our table, since this will give a better estimate than only 1 star accreting from the cell, and in an instantaneous consideration, the uncertainties associated with this decisions are assessed to be minimal, and less than just 1 star accreting. The mass available for accretion in the cell is then calculated with centre of mass quantities of the binary system instead of the quantities from the single star, and then we accrete as previously, just looping over the 2 stars instead.

Accretion in a Turbulent Medium Based on Vorticity

Considering accretion in a turbulent medium there are other parts affecting the accretion than just the Bondi-Hoyle accretion. That is what (Krumholz et al. 2005) sets out to try and find a better approximation by incorporating vorticity, $\omega = |\nabla \times \mathbf{v}|$, into an accretion rate for turbulent media as described in Eq. 4.11

$$\dot{\mathrm{M}}_{\mathrm{turb}}(\mathbf{x}) \approx \left[\dot{\mathrm{M}}_{\mathrm{BH}}(\mathbf{x})^{-2} + \dot{\mathrm{M}}_{\omega}(\mathbf{x})^{-2}\right]^{-1/2} \tag{4.11}$$

where $\dot{\mathrm{M}}_{\mathrm{BH}}$ is the Bondi-Hoyle accretion as in Eq. 2.8 and $\dot{\mathrm{M}}_{\omega}$ is the accretion in a vorticity-dominated medium as found by (Krumholz et al. 2005) and shown in Eq. 4.12

$$\dot{\mathrm{M}}_{\omega} = 4\pi\rho_{\infty}\frac{(\mathrm{GM})^2}{\mathrm{c_s^3}}0.34\mathrm{f}(\omega_*), \tag{4.12}$$

where

$$\omega_* \equiv \omega\frac{\mathrm{r_B}}{\mathrm{c_s}}, \tag{4.13}$$

is the dimensionless vorticity,

$$\mathrm{r_B} \equiv \frac{\mathrm{GM}}{\mathrm{c_s^2}}, \tag{4.14}$$

is the Bondi radius, and the function $\mathrm{f}(\omega_*)$ is approximated by

$$\mathrm{f}(\omega_*) \approx \frac{1}{1+\omega_*^{0.9}} \tag{4.15}$$

as done in (Krumholz et al. 2005) and (Krumholz et al. 2006).

In order to adapt this to our code, we need to flip the problem and consider the mass accreted from each cell. We do this by considering the mass that is available to be accreted from a cell as the mass within the Bondi radius as

$$\mathrm{M_{BH}} = \frac{4\pi}{3}\rho\mathrm{r_B^3} \tag{4.16}$$

We then calculate the fraction of mass accreted from the cell and the mass of the cell. This is given by

$$\frac{\Delta\mathrm{m}}{\mathrm{m_{cell}}} = \frac{\dot{\mathrm{M}}_{\mathrm{turb}}}{\mathrm{M_{BH}}}\Delta\mathrm{t}\ \mathrm{f_v} \tag{4.17}$$

Expanding this and simplifying we get

$$\frac{\dot{\mathrm{M}}_{\mathrm{turb}}}{\mathrm{M_{BH}}} = \frac{3\mathrm{c_s}}{\mathrm{r_B}}\ \mathrm{h} \tag{4.18}$$

with h being the numerical function given by

$$h = \left[\frac{(1 + \mathcal{M}^4)}{\lambda^2 + \mathcal{M}^2} + \frac{1}{(0.34f(\omega_*))^2} \right]^{-1/2} \tag{4.19}$$

We can conveniently rewrite r_B with quantities already available in the code as

$$r_B = \frac{GM}{c_s^2} = \left(\frac{v_K}{c_s} \right)^2 r \tag{4.20}$$

With $r = |\mathbf{r}_{cell} - \mathbf{r}_{sink}|$ which is the distance between the sink and the cell. Putting all this back together we get

$$\frac{\Delta m}{m_{cell}} = 3 \frac{c_s^3}{v_K^2} \frac{h}{r} \Delta t \ f_v \tag{4.21}$$

This gives us a new way to accrete mass from cells to sinks that we can apply to RAMSES. We retain the numerical efficiency factor, f_v, from before. This gives an advantage by eliminating the need for using α_{rate} from Eq. 4.1, which is good because it is a numerically needed efficiency factor that is not directly based in physics.

Unfortunately, due to the time required for these derivations along with the complexity of implementing it into the code and the time to run simulations to test the implementation, there has not been enough time to actually implement and test it. The considerations and implications this accretion recipe could have will be further discussed in the Future Work section of the conclusion.

Chapter 5

Results and Discussion

5.1 Accretion and Star Formation in an Isolated Collapsing Core

In this section we will look at an isolated collapsing core with the version of RAMSES before we make changes to accretion, i.e. the one described in 3.2 and used by (Haugbølle 2018). However, we do include a few diagnostics that will be described when they are relevant.

5.1.1 Simulation Setup

The setup used for all these different runs are based around one fiducial run and then all other runs make small changes to the *input.nml* file from there.

We simulate an isolated core in a 1 pc cube for 0.36 Myr, or approximately two free-fall times, where the output cadence is conveniently set to 1 kyr. In the timespan of two free-fall times it is almost certain that a collapse would happen if the conditions allow for it to happen as discussed in section 2.3, which is the reason for picking this simulation time. For refinement we use $\ell_{\text{min}} = 6$ and $\ell_{\text{max}} = 10$ along with the Truelove criterion (Truelove et al. 1997) to keep the number of Jean's lengths per cell constant and for the fiducial run specifically the constant number is 132. The resolution at ℓ_{max} is 200 AU/cell.

The isolated core is the region where star formation can happen, i.e., where the density of gas is higher than the surroundings. To better define the core parameters of the simulation we introduce Eqs. 5.1, 5.2 (Commerçon et al. 2008), and 5.3 (Hennebelle et al. 2011) in order to set the temperature, rotation, and magnetic fields with 3 simple dimensionless parameters in the *input.nml* file. These are α, β, and μ respectively.

$$\alpha = \frac{\mathrm{E_{therm}}}{\mathrm{E_{bind}}} = \frac{5}{2}\frac{\mathrm{Rk_BT}}{\mu \mathrm{m_p GM}} = \frac{5}{2}\frac{\mathrm{R}}{\mathrm{GM}}\mathrm{c_s^2} \tag{5.1}$$

$$\beta = \frac{\mathrm{E_{rot}}}{\mathrm{E_{bind}}} = \frac{1}{3}\frac{\mathrm{R^3\Omega_0^2}}{\mathrm{3GM}} \tag{5.2}$$

$$\mu = \frac{\mathrm{M}/\Phi}{(\mathrm{M}/\Phi)_{\mathrm{crit}}} = \frac{\mathrm{M}}{\sqrt{\mathrm{B^2\pi R^2}}\mathrm{c_\Phi G^{-1/2}}} \tag{5.3}$$

We set $\alpha = 0.65$ which is the same value used by (Commerçon et al. 2008). In the fiducial run we use $\beta = 0.04$ and $\mu = 5$ and for the other runs, these will be varied as per Table 5.1. We define a density contrast of $\Delta\rho = 0.1$, which corresponds to the ratio of the density of the surroundings and the density of the core, and then apply a bipolar density perturbation defined by Eq. 5.4 according to the density contrast. Here the radius of the core is set to 0.05 of the box length, which corresponds to 0.05 pc or 10313 AU. Lastly, we set the mass of the core to 1 $\mathrm{M_\odot}$.

$$\rho = \rho_0 \left(1.0 + \Delta\rho \cos\left(2 \arctan\left(\frac{\mathrm{y}}{\mathrm{x}}\right)\right)\right) \tag{5.4}$$

The physics parameters of the simulations are set such that the physical units of length are 1 pc, the units of time are 1 Myr, the units of density corresponds to 1 $\mathrm{M_\odot}$ with a sphere of radius 0.05 pc, the units of velocity are 1 km/s, the units of mass are 1909.86 $\mathrm{M_\odot}$, and the value for the gravitational constant is $\mathrm{G} = 8.589$, which in turn gives us a free-fall time $\mathrm{t_{ff}} = 0.185$ Myr.

There are also a few parameters specific to the numerical aspect of accretion which are investigated. These are defined as acc_fraction, acc_rate, and rho_limit_factor, which are set to 0.5, 0.2, and 4710 respectively in the fiducial run. acc_fraction is the fraction of mass available for accretion that will be accreted, acc_rate is an accretion efficiency parameter used in Eq. 4.1, where it is called α_{rate}, and rho_limit_factor is the density threshold for sink creating called ρ_{s} in Eq. 4.1.

5.1.2 Magnetism and Rotation

The following section looks at a parameter study of β and μ as introduced in Eqs. 5.2 and 5.3. Here β is a dimensionless rotation parameter and μ is a dimensionless parameter for the magnetic field strength. The runs presented here are simulated using β and μ according to Table 5.1 below.

When processing the data for each run we wrote a small data pipeline that processed each timestep of 1 kyr as a frame of a movie, and combined all frames into movies. We made movies of the density, log density, log density with velocity field overlaid, and log density with magnetic field lines overlaid. Each of these movies were done for a top down (x,y-plane) projection and straight on (y,z-plane) projection in order to be able to follow the evolution of the area over the duration of the simulation. This is a simplified version of the movies described in the analysis tools section 3.3.4, since that version requires the spin implementation.

Table 5.1: RAMSES Simulation Parameters

	$\mu = 0.5$	$\mu = 2$	$\mu = 5$	$\mu = 120$
$\beta = 0$	Run 5	Run 6	Run 7	Run 8
$\beta = 0.01$	Run 9	Run 10	Run 11	Run 12
$\beta = 0.04$	Run 13	Run 14	Run 15	Run 16
$\beta = 0.1$	Run 17	Run 18	Run 19	Run 20
$\beta = 0.5$	Run 21	Run 22	Run 23	Run 24

The parameters β and μ used for creating benchmark simulations for RAMSES. Apart from these parameters, all simulations used the same inputs, notably $\alpha = 0.65$ and simulating for ~ 2 free-fall times totalling ~ 360 kyr.

The total accreted mass for each run is shown in Fig. 5.1. We picked run 15 as our fiducial run, since it used the same parameters as (Commerçon et al. 2008) & (Hennebelle et al. 2011), and because it is a good middle ground of the parameters. From the plots we can see that no rotation yields close to 1 $M_\odot$ star regardless of the magnetic field in runs 5 to 8. Low rotation gives a similar profile, however the sink particles form slightly later, denoted by the black dashed line. In runs 13 to 16, we see that there is a balance between rotation and magnetic fields but increasing the magnetic fields decreases the total mass accreted. For runs 17 to 20 we see a similar pattern, however, the accreted mass drops by about half in runs 18 to 20, and there is an odd wiggle in the graph. In the last row no sink particles form due to the rotation being too high and there not being enough collapse for the density to exceed the thresholds for sink particle formation. Summing this up, along with conclusions from the videos, we see that with higher rotation, the gas stays in orbit around the sink particle, rather than being accreted to the sink particle, yielding a lower final mass. The magnetic fields act as fric-

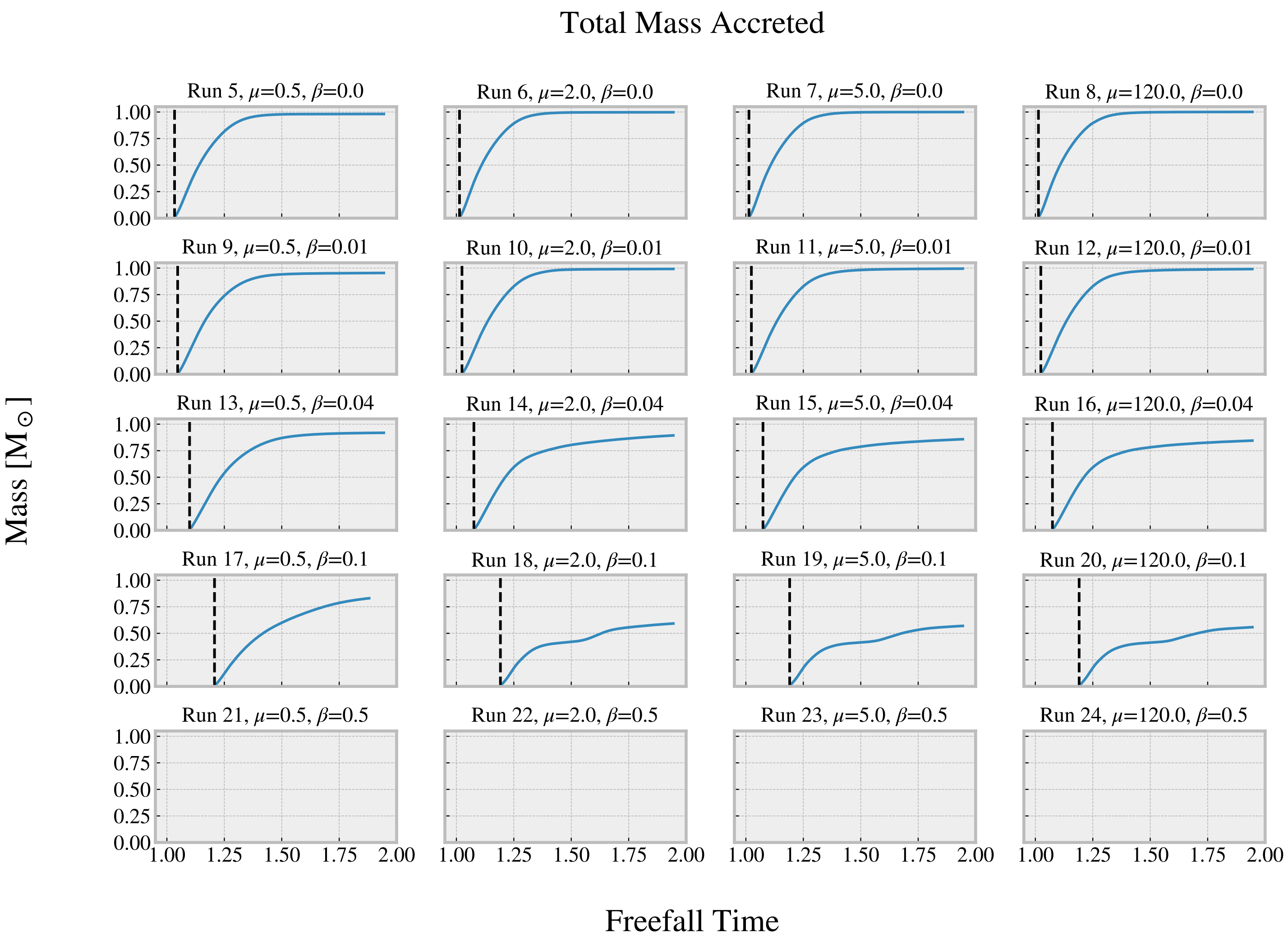

Figure 5.1: The total mass accreted for each run in Table 5.1 with the total mass having units of $M_{\odot}$ and the time having units of free-fall time, where $t_{ff} = 0.185$ Myr.

tion for the rotation, i.e. magnetic braking (Mestel 1968; Tsukamoto et al. 2022), thus transporting angular momentum along magnetic field lines giving rise to outflow and also yielding stronger accretion. This is an azimuthal frictional force acting opposite the rotation. The magnetic field lines in the z-direction get pinched during the simulation, resulting from a radial frictional force, which in turn reduces accretion. The azimuthal force reduces rotation and increases accretion, and the radial force reduces accretion.

When we then look directly at the accretion rates in Fig. 5.2 we come to

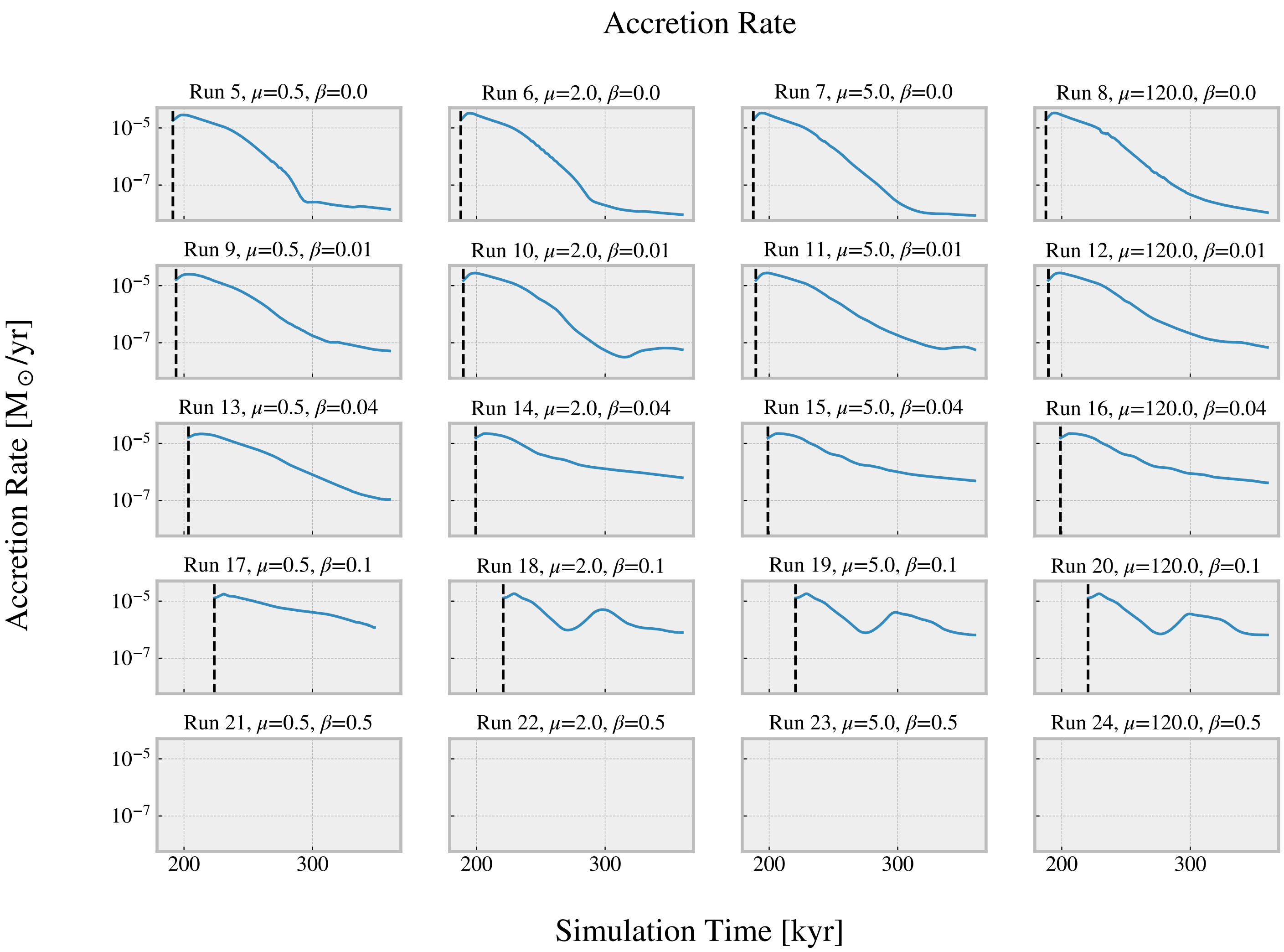

Figure 5.2: The accretion rate for each run in Table 5.1 in units of $M_\odot$/yr and with the x-axis being simulation time in kyr.

the same conclusions as above; however, we get a better view of the wiggle feature in runs 18 to 20. They start at a comparably high accretion rate to previous runs, but at around 300 kyr there is an increase in the accretion rate before there is a drop again to similar levels of runs 13 to 16.

Following up on our fiducial run, we made a higher resolution run with ℓ_{max}, corresponding to a resolution at the highest refinement level of 50 AU/cell. This simulation ran for 0.5 Myr and created 6 sink particles. The increased resolution likely leads to fragmentation of the sink we see form in run 15, as the resolution is 4 times greater and so the likelihood that the criteria for sink formation is met in an increasing number of cases is more likely. We will get back to this in section 5.1.3. The mass accreted for each sink particle, and the total accreted mass, is shown in Fig. 5.3.

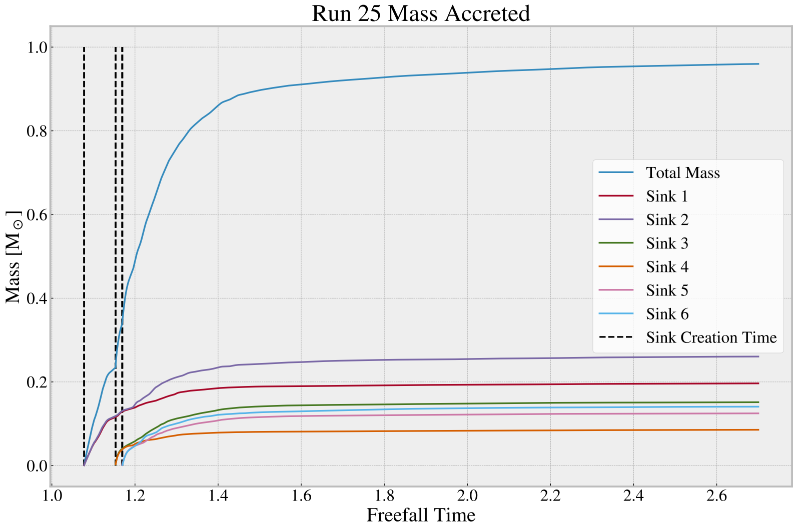

Figure 5.3: The mass accreted for each sink particle in run 25, along with the total mass accreted in units of $M_\odot$ and the time in units of free-fall times. The creation of each sink particle is marked with vertical dashed black lines.

The total accreted mass in run 25 looks quite similar to runs 9 to 12 rather than run 15 as would be expected. Further we see the 6 produced sinks are formed mostly in pairs with the heaviest pair forming first and the subsequent two pairs forming very close to each other, while also being close to each other in masses. The total accreted mass approaches the mass of the collapsing core meaning that between the sinks, most of the core has been accreted in the 0.5 Myr that the simulation ran for.

Looking at Fig. 5.4 which shows the accretion rate of all sinks in run 25 as a function of time, we see that it starts out at a similar accretion rate to runs 5 to 20, but due to sharing between 6 sinks it quickly drops below the lowest values in those runs. Furthermore, we see that there is high variability of the accretion rate over a very short timespan creating what appears to be almost vertical lines in many places. This is likely due to the current way of modelling accretion in binary and multiple systems, as we can see on the movies that most of these sinks indeed form as binary or multiple systems and over the course of the simulation they remain as such. In this model

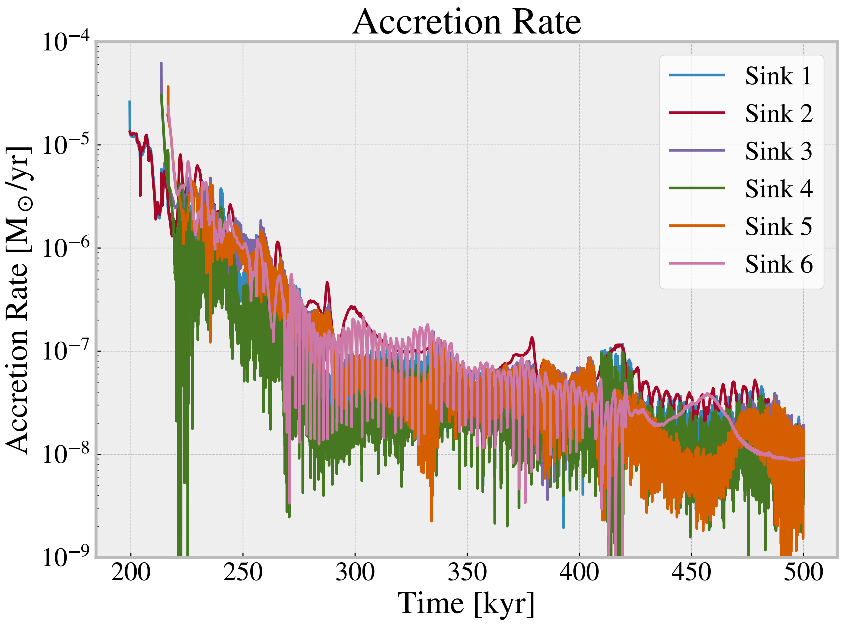

Figure 5.4: The accretion rate for each sink particle in run 25, in units of $M_\odot$/yr and the time in units of kyr.

only one sink can accrete from any one cell in a given timestep, which adds these extreme changes of up to 5 orders of magnitude in a short timeframe in the most extreme case, and a few orders of magnitude otherwise.

Having inspected both the accretion rate and accreted mass, we will now look at the radial profiles for the sinks in run 25 at the final output with t = 499kyr. The accretion radius is defined from *input.nml* file and calculated using Eq. 3.10 and it is plotted as a black dashed line. Within the accretion radius, we know that the profiles are more likely to not be physically accurate, since the numerical accretion process going on at small scales is not resembling high resolution models at the distances, and so we will ignore this for the time being. Firstly we look at the density profile, specifically the slope of it, as we know the slope in a loglog plot should approach ~ -2 for a BE sphere. The slope is calculated for each sink from the accretion radius and out to 1000AU, which is our current imposed limit of the profiles. The slopes are in the range -1 to -2.8 for these sinks, with the mean slope being close to -2. This corresponds well with the expected values for a collapsing BE sphere, which this setup is made to simulate.

Looking at the sound speed we also see it increases with distance, which

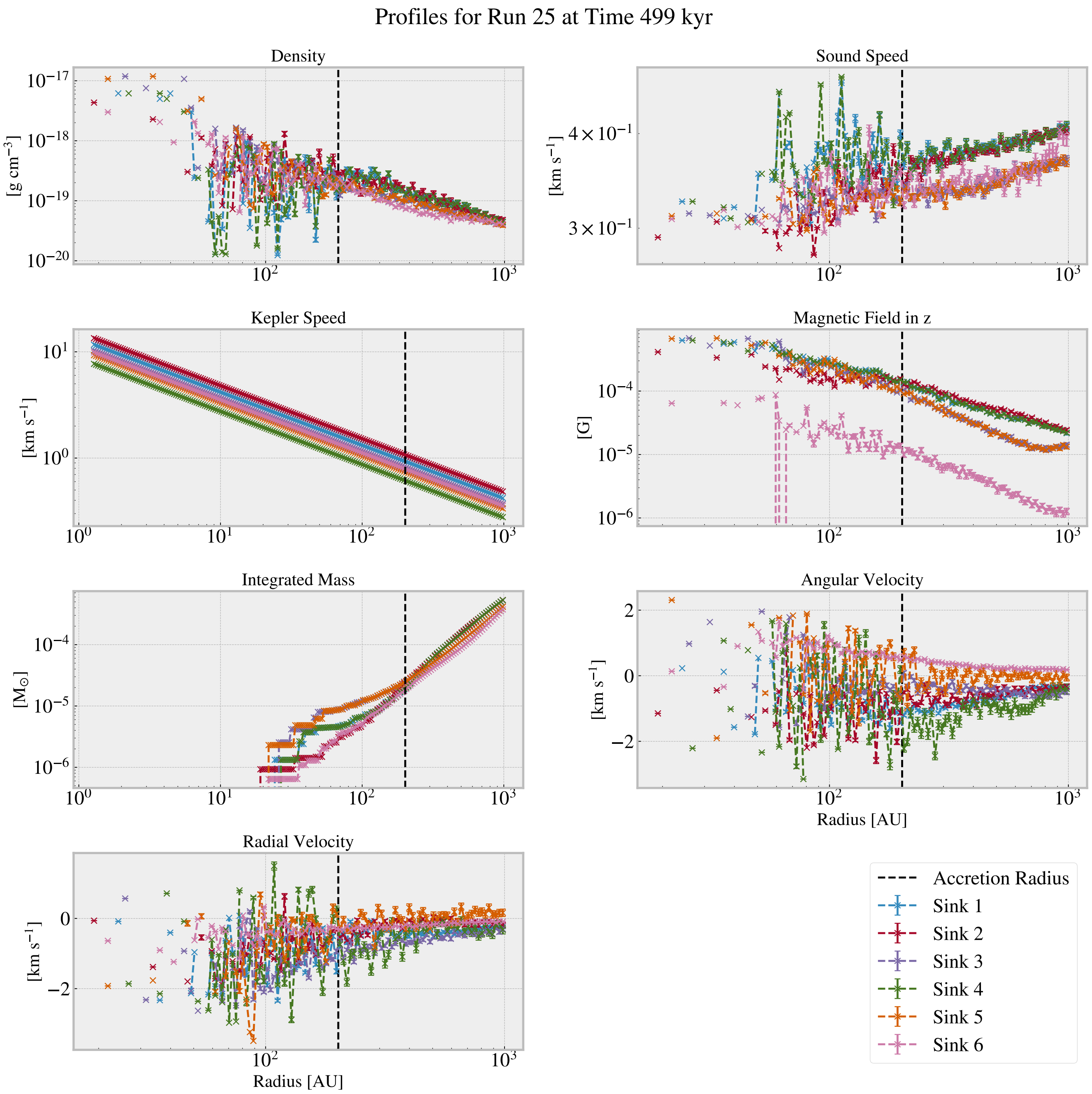

Figure 5.5: A collection of all the radial profiles for run 25 at t = 499kyr created as part of the analysis tools pipeline.

makes sense as the gas density is going down, since $c_s = \left(\frac{\partial P}{\partial \rho}\right)^{1/2}$. This mostly works as a sanity check, same as the Kepler speed and the integrated mass. The Kepler speed is linearly decreasing as expected. The integrated mass is monotonically increasing and approaching a similar value, and if we integrate in a much larger radius it should approach the same value regardless of the sink used as reference. Looking at the magnetic field profile we see that it corresponds well with an increase in density, since we see an increase in magnetic flux. We solve ideal MHD corresponding to infinite conductivity. This is often done in astrophysics, where many free charges are expected to be present in the plasma. In this case the frozen-in approximation is expected with the field lines following the mass flow. An accumulation of magnetic flux is therefore expected in high density regions. Furthermore, we see that sink 6 must have been created at a different position since the magnetic field strength is significantly different. Looking at the radial and angular velocities, we see that the angular velocities show rotation with some sinks having gas rotating one direction and some the other, but with similar angular speeds. The radial velocities are mostly negative meaning that the gas is travelling towards the sink, however, at the larger radii we see that some of the speeds are positive, showing gas travelling away, which could likely be from other sinks interfering and attracting the gas to them instead.

5.1.3 Numerical Parameter Study

In this section we will look at run 26 to 39, which investigate the parameters acc_rate, ℓ_{max}, rho_limit_factor, and acc_fraction with these runs being permutations of run 25, i.e of the fiducial run with $\ell_{\text{max}} = 12$. We will look at each of the parameter investigations separately.

Varying the Efficiency of Gas Accretion: acc_rate

Here we vary the parameter acc_rate, α_{rate} from Eq. 4.1, from 0.2 in run 25, then 0.1 for run 26, 0.03 for run 27, 0.01 for run 28, 0.003 for run 29, and finally 0.001 for run 30. Note here that run 29 crashed due to a known bug in RAMSES where a newly formed sink can jump one cell in rare cases. It is outside the scope of this project to fix this bug, so run 29 will be left out of the following section.

In Table 5.2 the number of sinks created in runs 25 to 30 and the total accreted mass in those runs are shown. We see that for accretion efficiency dropping below 0.03, that the total mass accreted in the runs start dropping. Especially for run 30, where we also see weird step-function-like accreted masses. Both of these are explained by the buildup of gas that cannot be accreted due to the numerical limitation of the α_{rate} parameter, and as such we see lower total masses even though the collapse occurs similarly. It is

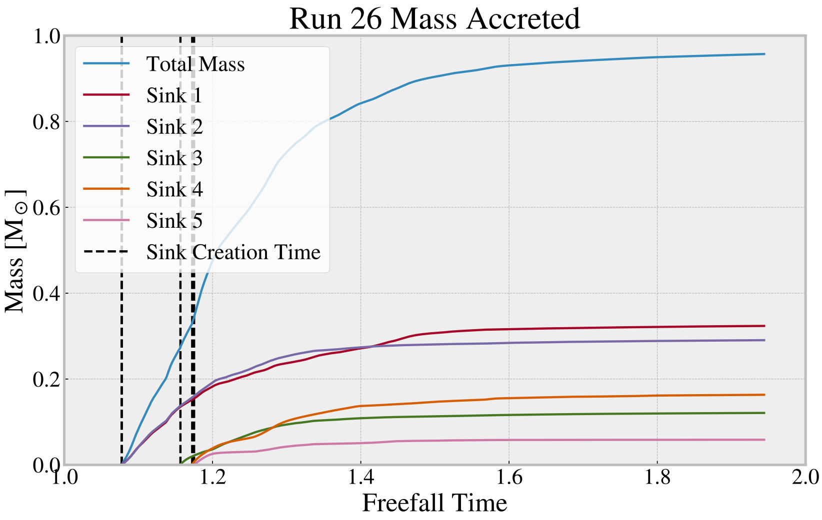

Figure 5.6: The total accreted mass in run 26 in units of $M_\odot$ and the time in units of free-fall times, $t_{ff} \approx 0.18$ kyr.

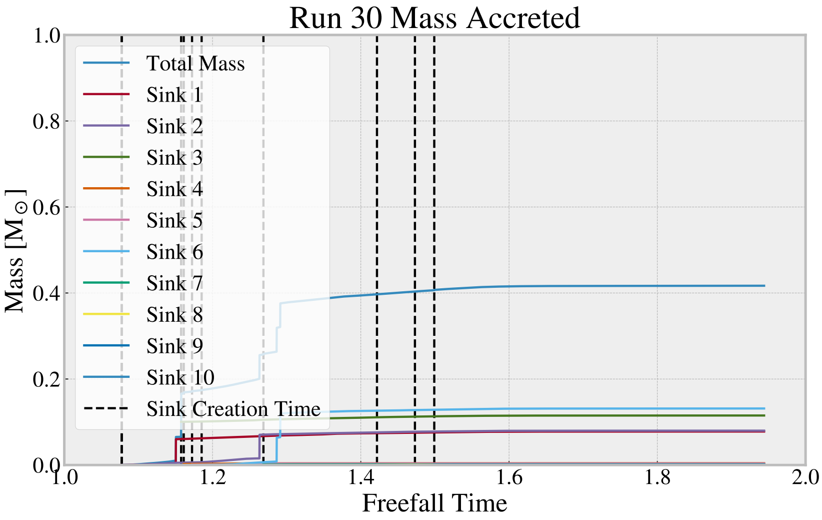

Figure 5.7: The total accreted mass in run 30 in units of $M_\odot$ and the time in units of free-fall times, $t_{ff} \approx 0.18$ kyr.

also likely that this buildup in gas is what causes the much larger number of sink particles in run 30 to form, since there is a dense area around earlier sinks that cannot be accreted, and eventually it could cross the threshold to create new sinks.

Run	Sinks	Total Mass [$M_\odot$]
25	6	0.95
26	5	0.95
27	6	0.85
28	10	0.65
30	10	0.4

Table 5.2: The number of sinks and the total accreted mass in runs 25 to 30.

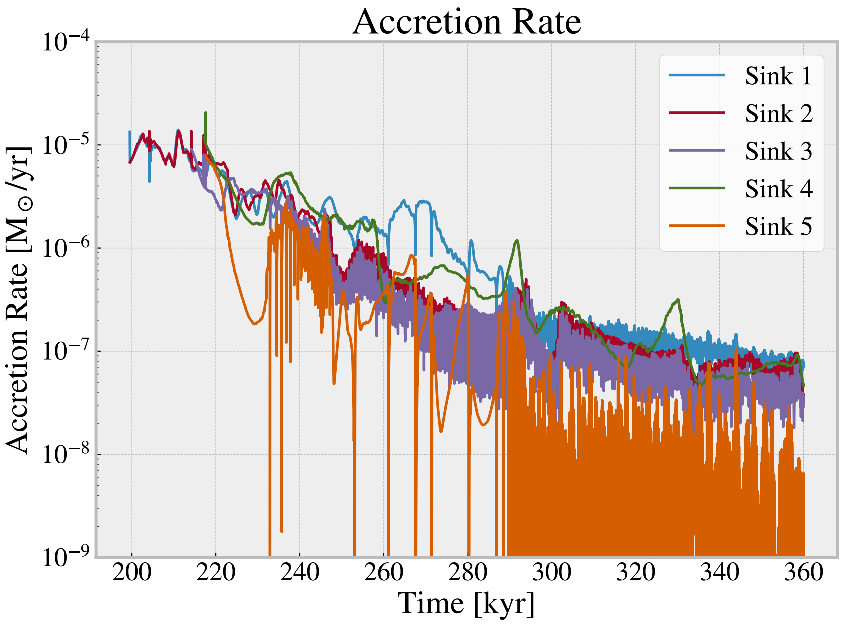

Figure 5.8: The accretion rates of the sink particles in run 26 in units of $M_\odot$/yr and the time in units of kyr.

Extending the above observations to the accretion rates, we compare specifically those of run 26 in Fig. 5.8 and those of run 30 in Fig. 5.9 as these are representative of the runs in between as well. In run 26 we will largely be disregarding sink 5 as we can see that it is affected by the same binary or multiple system accretion issues as previously described. Disregarding that, the accretion rate starts around a few 10^{-3} $M_\odot$/yr and goes to a few 10^{-5} $M_\odot$/yr at late times. In run 30 we see quite different accretion rates, and some of them unphysical. We see sink 1, 2, and 6 having accretion rates 4 orders of magnitude higher than the rest in what appears to be a single timestep, which corresponds well with what we saw with the total accrreted mass. We also see several sinks where the accretion rate is zero for several

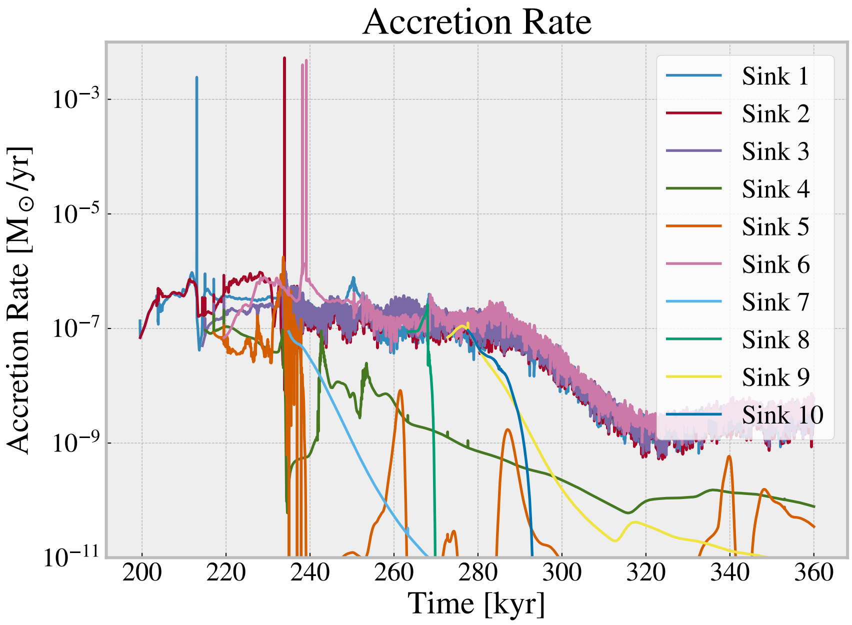

Figure 5.9: The accretion rates of the sink particles in run 30 in units of $M_\odot$/yr and the time in units of kyr.

different timesteps and several orders of magnitude lower than the bulk of the sinks for most of the simulation. If we then look at the bulk of the sinks, they start at around 10^{-4} $M_\odot$/yr and goes down to just over 10^{-6} $M_\odot$/yr at the end of the simulation. This corresponds well with a lower accretion efficiency and more stars having formed. To conclude, below a threshold value of approximately 0.01 α_{rate} seems to affect the physical evolution of the run because a buildup of material is observed near the sink particles leading to formation of spurious sink particles. Similarly, a very high value of α_{rate} will over accrete leading to unphysical low densities inside the accretion radius, leading to the creation of a vacuum that could promote further infall driven by an implosion. It therefore seems from this test that a reasonable value for α_{rate} is somewhere between 0.01 and 0.1.

Varying the Minimum Cell Size: ℓ_{max}

This investigation is to look both at the fragmentation of the idealised scenario, and to look at accretion rates and how they change as a function of ℓ_{max}. Here we will compare with run 15 using $\ell_{\text{max}} = 10$, once again with run 25 using $\ell_{\text{max}} = 12$, run 31 is simulated using $\ell_{\text{max}} = 14$, and run 32 uses $\ell_{\text{max}} = 16$.

Run 31 created 15 sinks and ran to about 230 kyr, while run 32 created 11 sinks and ran until about 204 kyr. The reason these runs only ran this shortly is that when the sinks start forming around 180-200 kyr, as for all these idealised scenarios, then the dynamics of the system becomes so complex that the adaptive timestep becomes very small. This means that for each day of wall clock time, only up to about 0.5 kyr of simulation time has passed, so we stopped the runs manually.

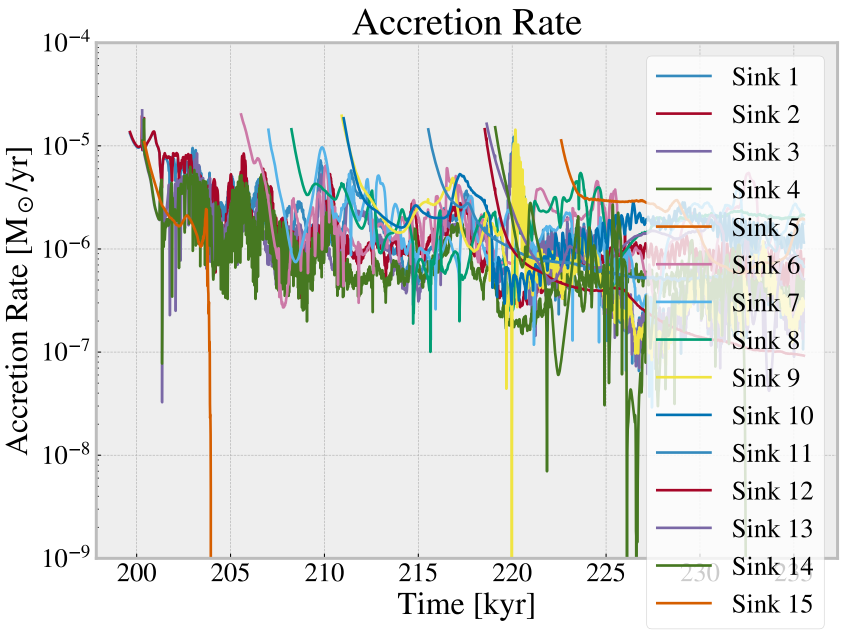

Figure 5.10: The accretion rates of the sink particles in run 31 in units of $M_\odot$/yr and the time in units of kyr.

For these runs it does not make sense to look at the total accreted mass since they ran for such a short time, so we will look just at the accretion rates. Looking at the accretion rates for run 31 in Fig. 5.10 we see that the majority of the sinks have accretion rates in the range 10^{-5} to a few 10^{-7} $M_\odot$/yr which is quite similar to the earlier runs we have looked at. There are a few sinks where the accretion drops to unphysically low levels. For run 32 in Fig. 5.11 we see a range of accretion rates of 10^{-5} to 10^{-6} $M_\odot$/yr for most of the sinks, but a few of them again show unphysical behaviour. Since both runs are so short its hard to say much about the accretion rates other than the fact that the early accretion rates are similar to the previous runs like run 25 and 26.

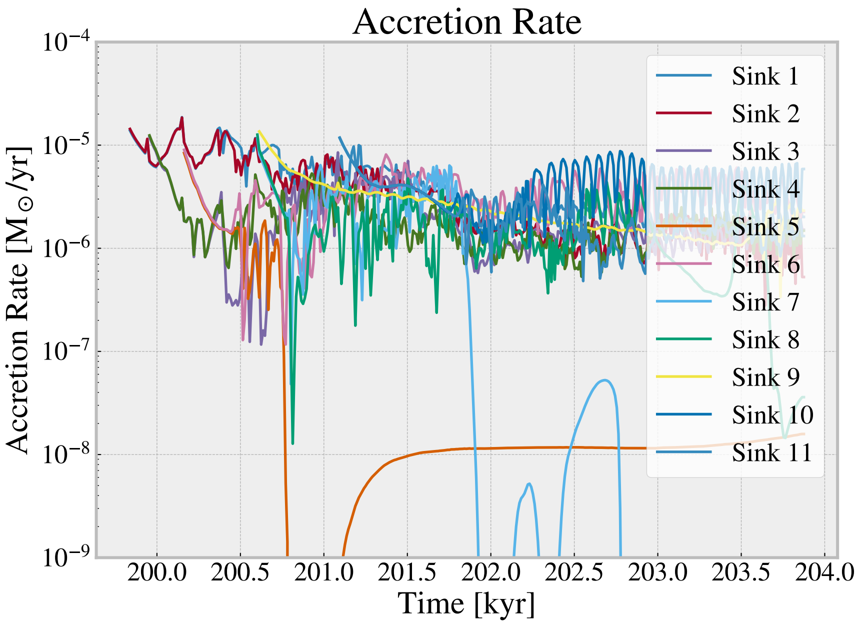

Figure 5.11: The accretion rates of the sink particles in run 32 in units of $M_\odot$/yr and the time in units of kyr.

The main takeaway from these two runs is that idealised scenarios do not handle smaller minimum cell sizes well. This is because the adaptive timestep becomes so small that the simulations take so long to run. This means that the computational cost becomes high for the small amount of possible knowledge to be gained, especially for this case where it is a simple idealised setup like here.

Varying the Threshold Density for Sink Creation: ρ_s

The purpose of varying the threshold density for sink creation is to see if we, with the previous setups, can achieve an idealised run with just one or a few sinks that behave as they would in a more complex and realistic scenario, and with higher resolution than runs 5 to 24. Here we base the runs on run 25 and then we vary ρ_s, which is scaled numerically by rho_limit_factor introduced earlier, from 1.9×10^{-10} g/cm^3 in run 25, to 2.5×10^{-10} g/cm^3 in run 33, and to 4.9×10^{-10} g/cm^3 in run 34. In run 35 we set rho_limit_factor back to 2.5×10^{-10} g/cm^3 and vary the parameters giving us the accretion radius, i.e. the max distance in cells from 8 to 16, and the accretion fraction from these from 0.5 to 0.25, which effectively keeps the accretion radius constant, but varies how we get there. We also change the density contrast from 0.1 to 0.05. Finally in run 36 we use the same parameters as run 35, but halve the density contrast to 0.025.

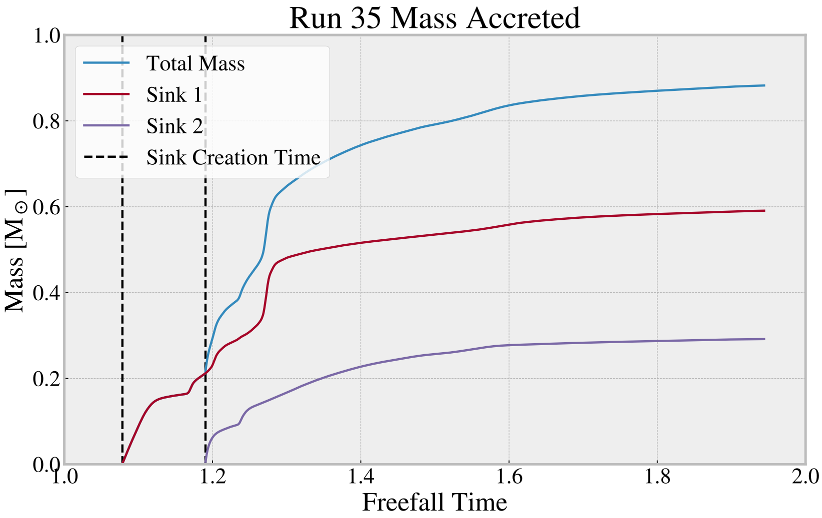

Figure 5.12: The total accreted mass in run 35 in units of $M_\odot$ and the time in units of free-fall times, $t_{ff} \approx 0.18$ kyr.

For all runs discussed here, the simulation ran for the full 360 kyr (2 free-fall times) and in this time we see 7 sink particles form in run 33, 5 sink particles for in run 34, 2 sink particles form in run 35, and 4 sink particles form in run 36. Looking at the total accreted mass, both runs 33 and 34 look near identical to run 25 at around 0.95 $M_\odot$. Run 35 is just below 0.9 $M_\odot$ but the sinks have some odd, very rapid, accretion periods, which can be seen in Fig. 5.12 and the corresponding accretion rates in Fig. 5.13, where we see accretion rates close to 5×10^{-2} $M_\odot$/yr, which is amongst the highest we have seen thus far. In run 36 the total accreted mass is slightly over 0.95 $M_\odot$, but one of the sinks have similarly weird accretion bursts as seen in run 35, with accretion rates for that sink looking very similar to sink 1 of run 35. Furthermore, specifically for run 33, we get a bar instability which happens when the bipolar density perturbation collapses faster than the global collapse. In this run they occur at roughly the same timescale according to the movies, with the perturbation collapsing slightly faster, which is an unphysical scenario. The movies are avaiable on `https://sid.erda.dk/cgi-sid/ls.py?share_id=fEWvzEfnsN`.

The accretion rates for run 33 and 34 are again quite similar to those of run 25 in Fig. 5.4 and so is the accretion rates for the remaining sinks in run 36, if the outlier above is taken out of consideration.

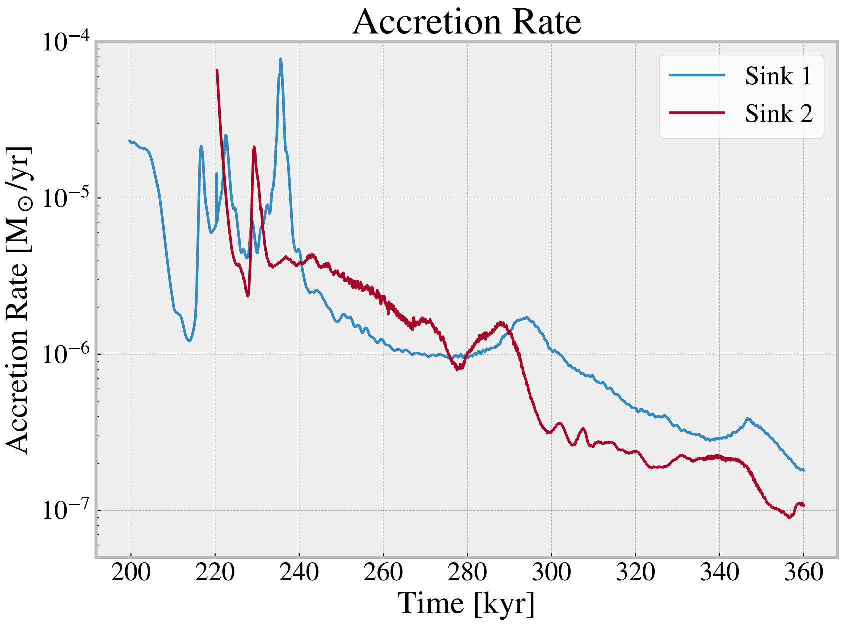

Figure 5.13: The accretion rates of the sink particles in run 35 in units of $M_\odot$/yr and the time in units of kyr.

Based on these runs, we do see a decrease in the number of sink particles that form, but at the cost of accretion behaviour that does not line up with our expectations based on previous runs with similar physical parameters.

Varying the Accretion Radius: acc_fraction

In this section we build on the previous section, more specifically run 35, where we vary the accretion radius from Eq. 3.10 by varying acc_fraction from 0.25 in run 35 to 0.1 in run 37, 0.03 in run 38, and 0.001 in run 39. Unfortunately both run 37 and 39 failed to run after the formation of one of the first few sinks, due to the same error as described above at run 29, and it is outside the scope of the project to fix this known error.

We will be looking only at run 38 for this, since the others crashed. It ran all 360 kyr and formed 5 sink particles in this time. The total accreted mass is around 0.75 $M_\odot$, which is significantly lower than the 0.9 $M_\odot$ we have seen earlier. Sink particle number 3 in Fig. 5.14 has an odd spike in accreted mass as it forms. This immediately turns this sink particle into the heaviest in this run. If we then look at the accretion rate in Fig. 5.15,

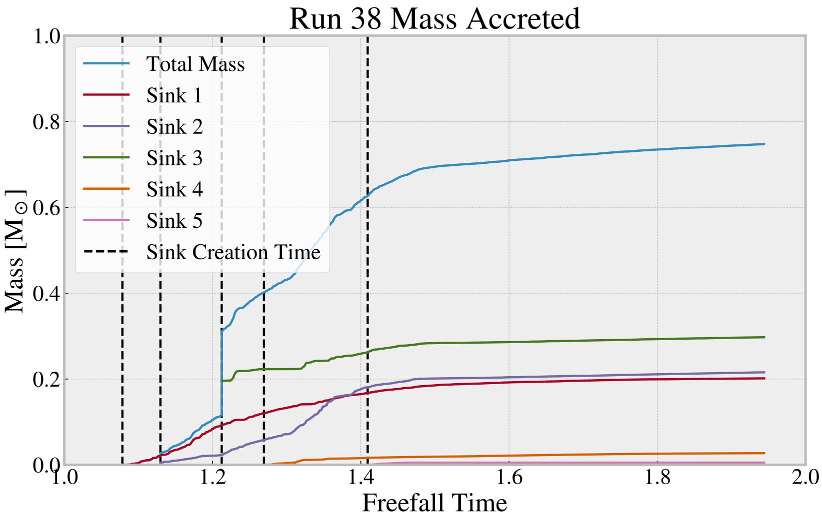

Figure 5.14: The total accreted mass in run 38 in units of $\mathrm{M}_\odot$ and the time in units of free-fall times, $\mathrm{t}_{\mathrm{ff}} \approx 0.18$ kyr.

it shows high accretion rates around 10^{-4} $\mathrm{M}_\odot$/yr, but we see the binary or multiple system issue as described earlier, where the accretion rate drops to practically zero.

Investigating these parameters we find overall that the fiducial run is more numerically stable and physical than most of the others. Increasing ℓ_{max} to 12 keeps similarly good simulations, where there are little to no numerical artefacts affecting the physics. Changing the accretion specific parameters more than a little bit from the fiducial run has not yielded simulations well suited for testing implementations. Since testing new implementations of accretion recipes and other code changes was the overall goal for these simulations, we will keep using the fiducial run, or small variations there off, for testing in the coming section.

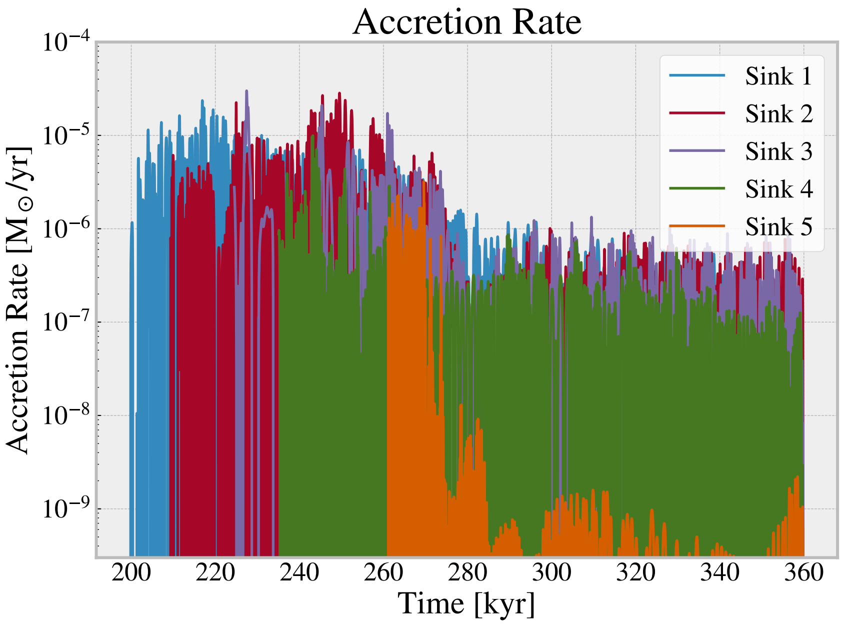

Figure 5.15: The accretion rates of the sink particles in run 38 in units of $M_\odot$/yr and the time in units of kyr.

5.1.4 Spin Evolution

In section 4.0.2 we introduced Eq. 4.7 (the equation for tracking spin) and implemented it in our simulation code. In order to test the spin implementation we take run 15 and re-run it with the spin implementation, and another run where we change $\ell_{\text{max}} = 16$ to see the effects at higher resolution. The second run is at a much shorter timescale due to the very short timesteps we discovered at high resolutions in the previous sections. These are runs 40 and 41 respectively. The first run is about 360 kyr, and the higher resolution run is about 220 kyr. Since the spin tracking is mostly a diagnostics tool, our analysis tools will focus on visualising the spin in a few different ways. The first is in a Mollweide projection, as it is an area-conserving projection of the spherical space, with the time as the colour bar. The next is to visualise the angles as a function of the time. Finally we visualise the spin x-, y-, z-components as a function of time in one plot. The last two are mostly meant as a testing feature as we expect the idealised run 15 to be purely in the z-direction after the sink settles in the time after creation. It is worth noting that the last two tools are only suited for analysis of 1 sink particle as otherwise the plot gets overcrowded and it is near impossible to draw any conclusions.

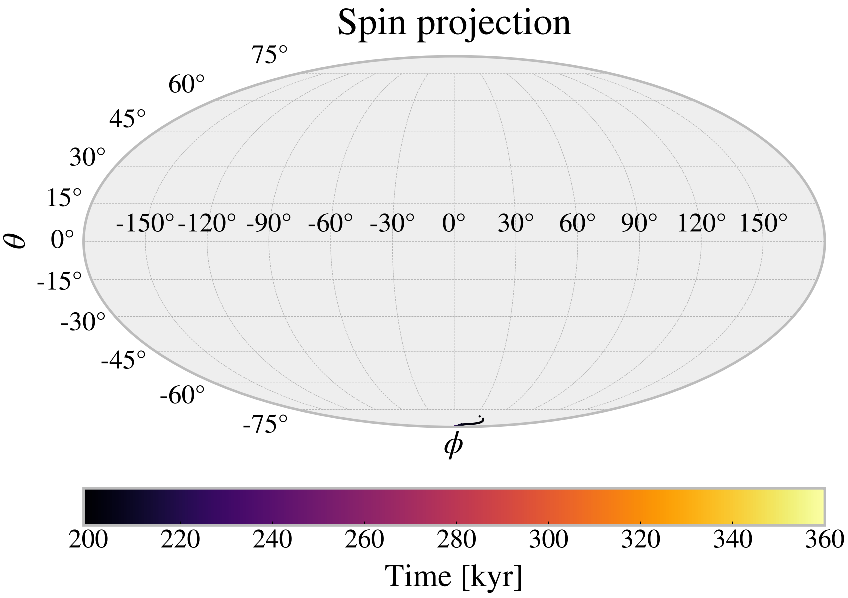

Figure 5.16: Mollweide projection of the spin of the sink particle in run 40 shown with angular positions as a function of time.

In Fig. 5.16 we see that the sink particle is created with orientation close to the south pole of the Mollweide plot and then it goes towards the south pole. It is challenging to see in this idealised situation if it actually goes to the south pole as expected, since it is mostly in the south pole area. In order to confirm that, we will use the plots of the spin components.

Looking at Fig. 5.17 we can see that the x-, y-components of the spin are going to 0 and the z-component is going to -1, which is consistent with the south pole of the Mollweide plot. This is as we expected in this idealised scenario.

Now looking at run 41 in Fig. 5.18 we see a similar pattern. The sink particles are created pointing in random directions, although mostly towards the south pole, and in the time available in the high resolution simulation we see them all turning towards the south pole, even if all of them do not get there in the 220 kyr of the simulation. This mostly works as a confirmation that the spin tracking works as anticipated both at lower resolution and

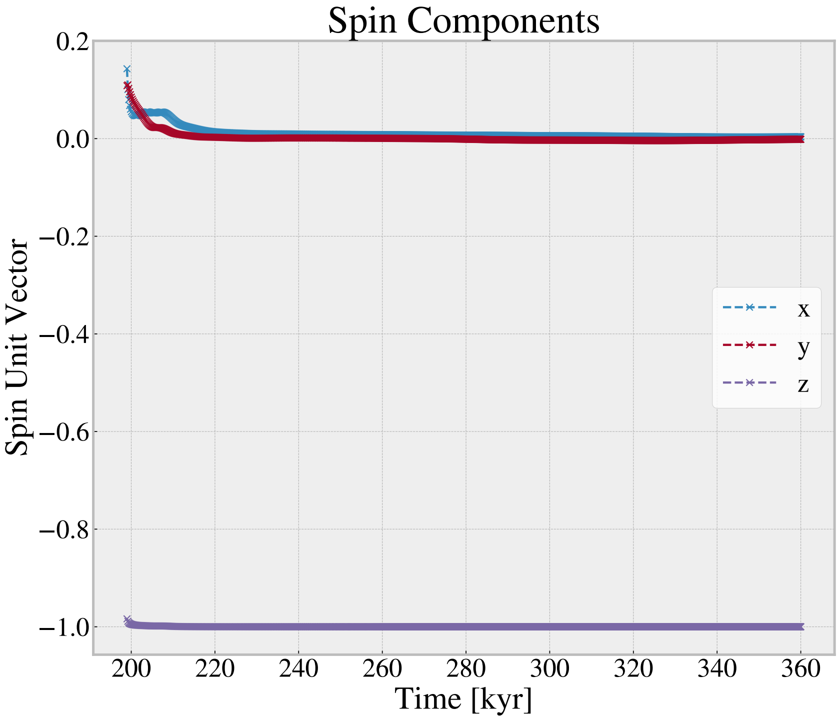

Figure 5.17: Plot of the x-, y-, z-components of the spin vector of the sink particle in run 40 as a function of time.

at higher resolutions and produce what we are expecting in these idealised simulations, which it certainly does.

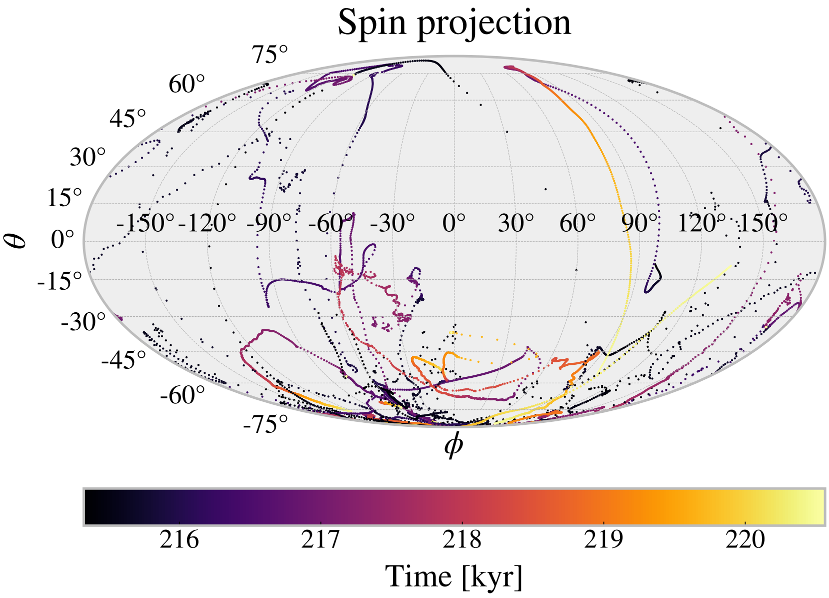

Figure 5.18: Mollweide projection of the spin of all the sink particles in run 41 shown with angular positions as a function of time.

5.2 Evolution of the Disk and Stellar Rotation Axis

5.2.1 Simulation Setup

In this section we will be studying the accretion process in a realistic environment. Using the method of zoom-in simulations as described in section 3.2.2. The initial and boundary conditions is supplied by embedding the model in to a global simulation of a star forming region. Here we will be using a simulation that has the same parameters as the fiducial run described in (Haugbølle 2018), but the model has 8 times higher number of cells at all AMR levels and a maximum cell size of 25 AU. This is an excellent basis for modelling the formation of a single star in detail, while retaining the effects of torques and the anchoring of the magnetic field. Specifically, we use sink 13, a single star that is in a relatively isolated prestellar core, with a smooth core geometry, placed at the edge of a denser environment that has a velocity contrast to the surrounding low-density void. The compression at the upstream edge of the cloud generates a compression that leads to the formation of sink 13. To study the accretion process systematically, and obtain numerically sound results, we carry out the run at three different resolutions, namely $\ell_{\max} = 17,\ 18,$ and 19, which gives us minimum cell sizes of 6 AU, 3 AU, and 1.5 AU respectively. We then repeat this with accretion efficiency parameter, $\alpha_{\text{rate}} = 0.05$ and 0.1. The fiducial run for this section is run 42 that has $\ell_{\max} = 19$, acc_rate = 0.1, and finally rho_limit_factor = 2355, which is different to all previous runs, but will not be varied here. For all runs we set the output cadence to 50 yr and let them run for 40 kyr, with the exception of our fiducial run, which ran for just over 50 kyr.

To convert from computational to physical units, a units class was developed in Python by Troels for this setup, which we have applied directly when loading the data into our analysis setup.

5.2.2 Results

Firstly, we want to look at the total accreted mass of sink 13 across resolution and α_{rate}. Note that Fig. 5.19 goes to 50 kyr instead of 40 in the other runs, so we will compare at 40 kyr. Starting with run 42, the total accreted mass is just below 0.6 $\mathrm{M}_\odot$, then for run 44 ($\ell_{\max} = 18$) it is slightly over 0.6 $\mathrm{M}_\odot$, and for run 43 ($\ell_{\max} = 17$) it is also slightly over 0.6 $\mathrm{M}_\odot$. Qualitatively this means that for lower resolution, sink 13 accretes slightly more mass over the duration of 40 kyr, but it is not a noticeable difference when visually inspecting the plots. The shape of the curves are also very similar. When we then look at runs 45 to 47 with $\alpha_{\text{rate}} = 0.05$, we see a similar pattern, that $\ell_{\max} = 19$ is lowest with the other resolutions linearly increasing ever so slightly, and they are all just around 0.6 $\mathrm{M}_\odot$. The one thing to note, is that for $\alpha_{\text{rate}} = 0.05$, the total mass has shifted to about 0.01 $\mathrm{M}_\odot$ less than the equivalent runs with $\alpha_{\text{rate}} = 0.1$.

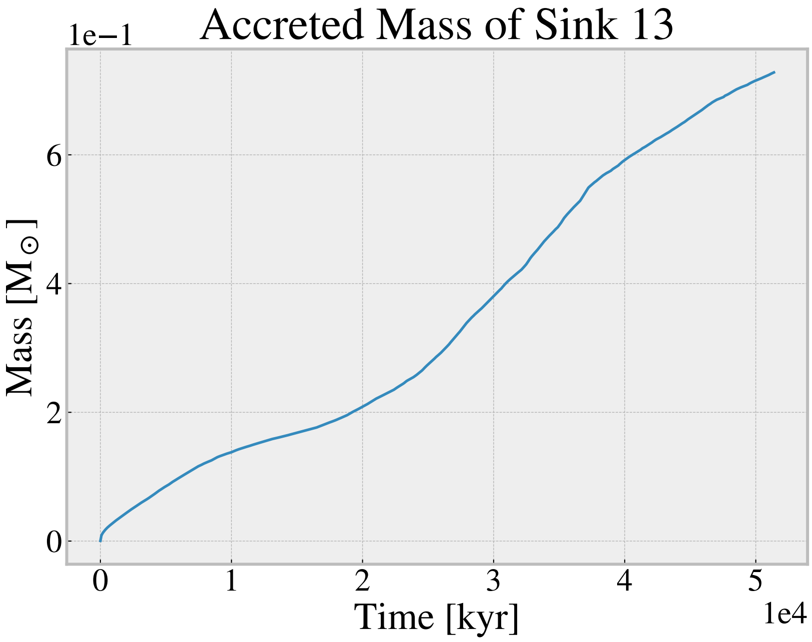

Figure 5.19: The total accreted mass of sink 13 in run 42 in units of $M_\odot$ and the time in units of kyr.

Taking a look at the accretion rates, we specifically want to inspect the relation to resolution. For that reason we show $\ell_{\max} = 17$ and $\ell_{\max} = 19$ in Fig. 5.20. Again note that run 42 ran for longer than the other runs, so we need to compare up to 40 kyr. Looking at Fig. 5.20a we see that the accretion rate starts at about 2 times higher than Fig. 5.20b but they both quickly fall to around 10^{-5} $M_\odot$/yr, where at first they both drop a little below and then rise to about 2×10^{-5} $M_\odot$/yr at around 40 kyr. These quite similar accretion rates, both the values and the shape of the curve over time, show up in the other 4 runs as well and there is no differences not mentioned here already as they lay in the small gap of these two runs. This lines up well with the close values in total accreted mass above.

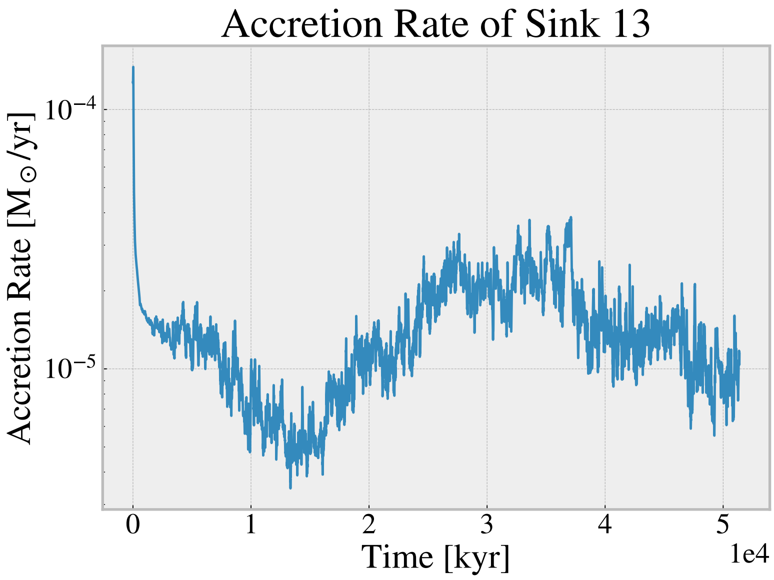

(a) Run 42 with $\ell_{\max} = 19$

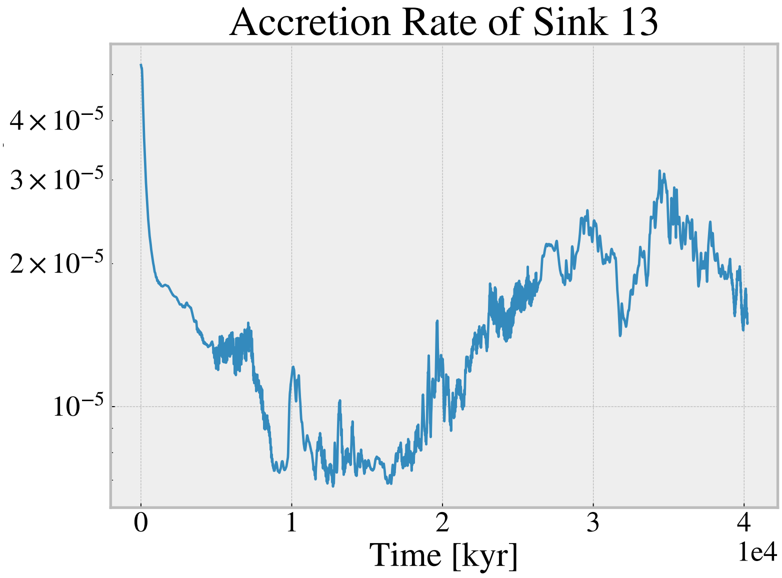

(b) Run 43 with $\ell_{\max} = 17$

Figure 5.20: The accretion rate of sink 13 for run 42 and 43, in units of M$_\odot$/yr and the time in units of kyr.

From both the accreted mass and the accretion rate we see, that the evolution of the sink particle is not largely affected by the change in resolution, and that the accretion efficiency (α_{rate}) has little effect on this as well. This is overall a good property, as it allows us to get similar results spending many fewer cpu-hours. For example run 42 with $\ell_{\max} = 19$ took 10 days to get to 40 kyr, and run 43 with $\ell_{\max} = 17$ took 1 day to get to the same around 40 kyr, using the same type and number of nodes in the HPC centre. Having looked at the accretion rates and accreted mass we will now look at the spin implementation and the curious feature we noticed in the movies, specifically in run 42 where with the high resolution it was more visible. This is that the normal vector of the disk changes angle with the direction of the spin of the sink particle and this is the reason we evolved run 42 for another 10 kyr.

The feature we see in the movies is that around 30-40 kyr, the disk turns at an angle to the spin to the point where the x-/y-, z-plane looks like the top down view, which previously, and after, was in the x-, y-plane. This can be seen in Fig. 5.21 in the 30-40 kyr, where we look top down at the x-, y-plane, which is equivalent to the left panel of the movies. More specifically, looking at t = 30 kyr, we see the disk being in the y-, z-plane as compared to the sink, with the thickness in x. Just a few timesteps later we see the disk being back in the x-, y-plane. It is more obvious in the movies. What we think is happening is that the sink particle itself is changing its direction to the environment, and in extension the disk, but moving rapidly so that within a few kyr it is back to the same plane as before. We can also see this by looking at the direction of the spin of the sink in Fig. 5.22, where we do see the sink particle actually changing its direction quite a lot. From this, it does look like both the sink and disk changes the direction, but that the sink changes its direction much faster and the disk slowly following. We infer this from seeing the view of the disk return to the x-, y-plane, even though we see that the sink particle does not return to the same direction as prior.

When we look at the movies we observe outflows at all our 3 resolutions. At low resolutions they are not well resolved, but they are visible, and in the higher resolution they are quite well resolved. The fact that we observe these is good as we know they should exist in our simulations since they have been observed as per section 2.4.3.

Finally, we look at the radial profiles in Fig. 5.23 for run 42 at the last output at 51 kyr. We see a bump at 20-50 AU in the density profile. Comparing this to the last panel in Fig. 5.21 we see that this bump is at the distance that the high density area of the disk at this time. Other than the bump, the profile is near linear in loglog, with a slope of ~ -2 as we would expect

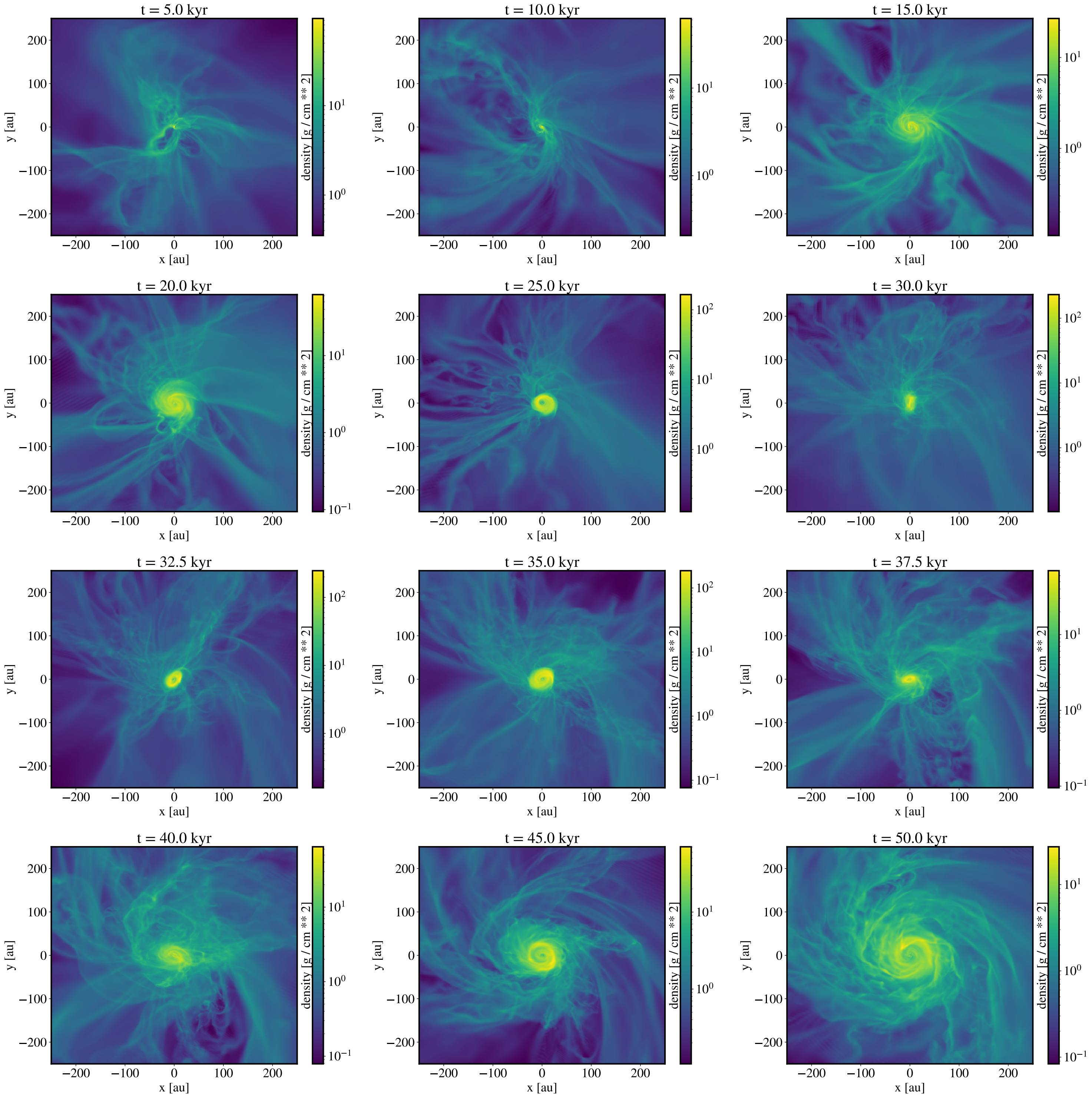

Figure 5.21: A grid of snapshots from run 42 with sink 13 from 5 kyr after sink 13 formed until 50 kyr, where the view is top down as defined by the spin vector.

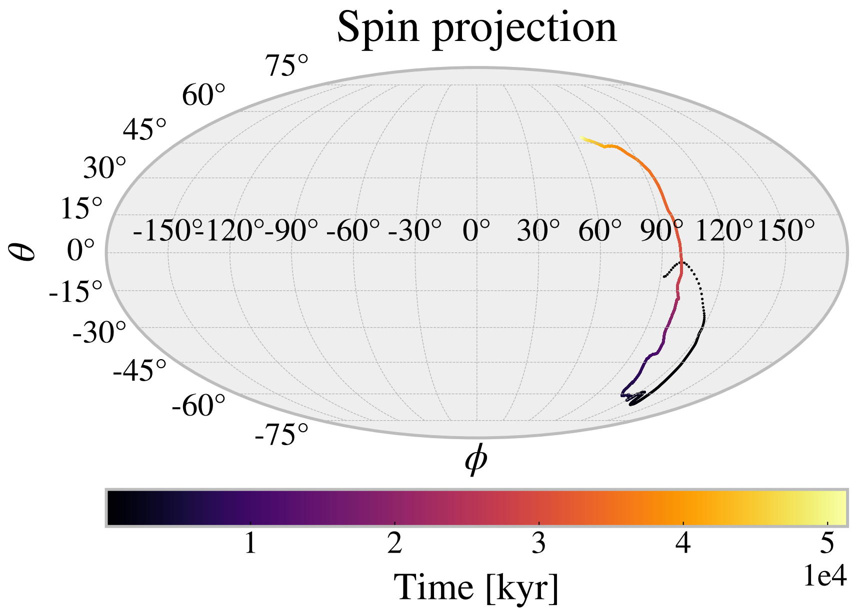

Figure 5.22: Mollweide projection of the spin of sink 13 in run 42 shown with angular positions as a function of time.

for BE-spheres, although it is slightly above. The other profiles show no oddities and are as we expect, e.g. rotation being confirmed by the angular velocity, which we also see in the videos, and infall being confirmed by the radial velocity, which is negative for all radii in the figure.

In this section we have seen that a zoom-in run gives very good and stable results overall over the three different resolutions and two different α_{rate}. There is a lot of advantages to doing zoom-in runs, but also especially one big disadvantage, the computational cost. For one or a few sink particles, zoom-in runs are viable and very powerful at the resolutions presented here, especially $\ell_{\max} = 18$ for a good compromise with resolution to see the evolution in the movies and not spend many weeks of compute time on running the simulation. However, if one needs zoom-in runs for many sinks, an alternative method might be preferred, one of which is preferential binary accretion that we will explore in the next section.

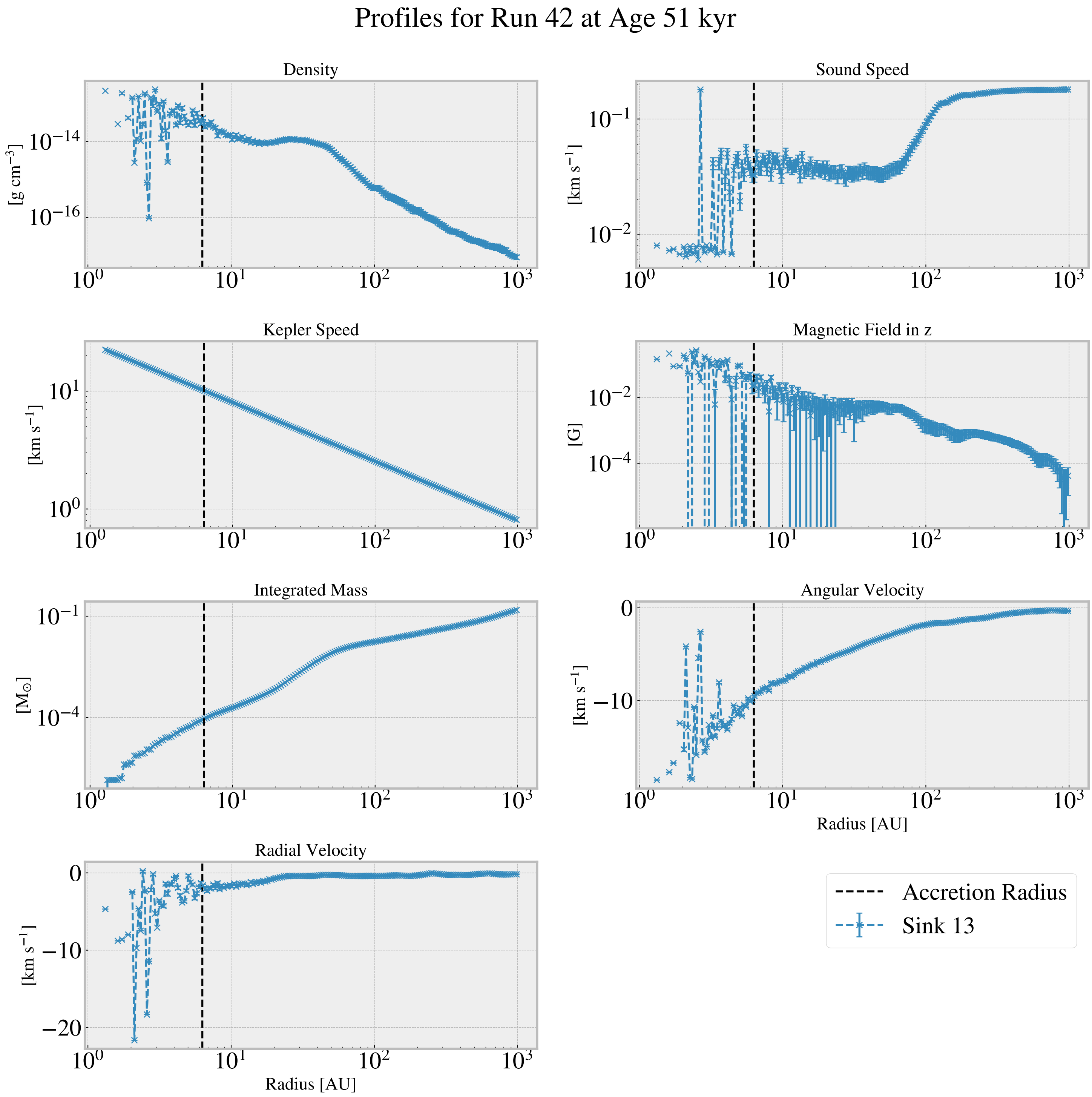

Figure 5.23: A collection of all the radial profiles for run 42 at t = 51 kyr created as part of the analysis tools pipeline.

5.3 Investigating Preferential Accretion in Close Binaries

There exists many types of binaries, wide binaries with 10000 AU, tight binaries, and even contact binaries. Observationally we find that the distances vary with mass ratio, but for solar mass stars, the typical distance is 10 - 5000 AU (Offner et al. 2022). It is important to have accretion recipes that can take care of binaries, whether it is a zoom-in run like section 5.2 or a global simulation, especially for close binaries where their accretion radii overlap some of or all the time. In this section we will be investigating the effects of implementing a preferential binary accretion recipe on close binaries.

5.3.1 Simulation Setup

The basis for this simulation is the global simulation with parameters as described in the fiducial run in (Haugbølle 2018). This is a great starting point to test our implementation of preferential binary accretion since it is a well developed star forming region, that is known to give good results on a global level, and it would cost several months of 1000 CPU cores to develop a similar star forming region. We use the resolution, which is $\ell_{\mathrm{min}} = 8$ and $\ell_{\mathrm{max}} = 14$ giving us a minimum cell size of about 50 AU. Further, we increase the output cadence to 500 yr to get several outputs over a short time. The testing setup consists of two runs, 48 and 49, where run 48 does use our preferential accretion recipe, and 49 does not. They both run for about 30 kyr. In order to convert from computational units to physical units, we use the same unit class in Python as in the previous section, since the unit conversion is the same.

5.3.2 Results

In these simulations we have a little over 300 sinks with about 30 binary or multiple systems. Of those we will look closer at pair 15, 25, and 28, where pairs 25 and 28 are binaries and pair 15 is part of a triple system. We will be looking at these pairs in a shorter timeframe, namely 2 kyr, in order to get a better overview of what is going on instead of the full 30 kyr of the simulations.

The first pair, number 25, consists of stars 292 and 290, that has masses 1.01 $\mathrm{M}_{\odot}$ and 0.28 $\mathrm{M}_{\odot}$ respectively, with a mass ratio of $\mathrm{q} = 0.27$. They have distance ranges of about 0.9 cells to 1.2 cells to each other, and eccentricities about 1.2 to 1.3. Their orbital period is about 0.2 kyr. Looking at Fig. 5.24 we see that turning on preferential binary accretion swaps the accretion rates of the primary and the secondary sink particles. This can be explained by their mass ratio and Fig. 4.1, which shows that the secondary sink particle should indeed have a few times higher accretion rate at this configuration. The other main observation is that the accretion rate of the secondary sink particle varies a lot less with the orbital motion of the system. The total accretion rate of the system in this timeframe is near identical at most points.

Pair 28 consists of stars 283 and 285, that has masses 0.27 $M_\odot$ and 0.26 $M_\odot$ respectively, with a mass ratio of $q = 0.96$. They are within one cell of each other at all times in this snapshot, namely in the range 0.2 cells to 0.6 cells, and at these distances the eccentricity of the orbit starts to become somewhat meaningless due to the numerical smoothing happening, but for the purposes of calculating the accretion ratio, the eccentricity is about 0.55. The orbital period of this system is about 0.1 kyr.

In Fig. 5.25 we see the accretion rates, distances, and eccentricities for pair 28. For this pair we see that, unlike pair 25, the primary sink particle accretes more than the secondary, which is true for both the original algorithm, as well as the new one. This is because of the high eccentricity and high mass ratio as we can see in Fig. 4.1. Furthermore, we see that for the preferential binary accretion run, both accretion rates are with a few times of each other and has a similar value over this range, varying mainly with the orbit of the binary system. This is unlike the original sink particles where when they are at periastron (their closest approach) one of the two sink particles drop their accretion rate by up to two orders of magnitude only for a few points around periastron. This is similar to what we saw e.g.g in run 38 in Fig. 5.15, which is one of the main issues we are trying to solve. The fact that this big dip gets negated in our new approach where we specifically handle binary accretion is seen across most of these pairs, where it would activate due to the overlap of their accretion distances, is a success to see that it works as intended.

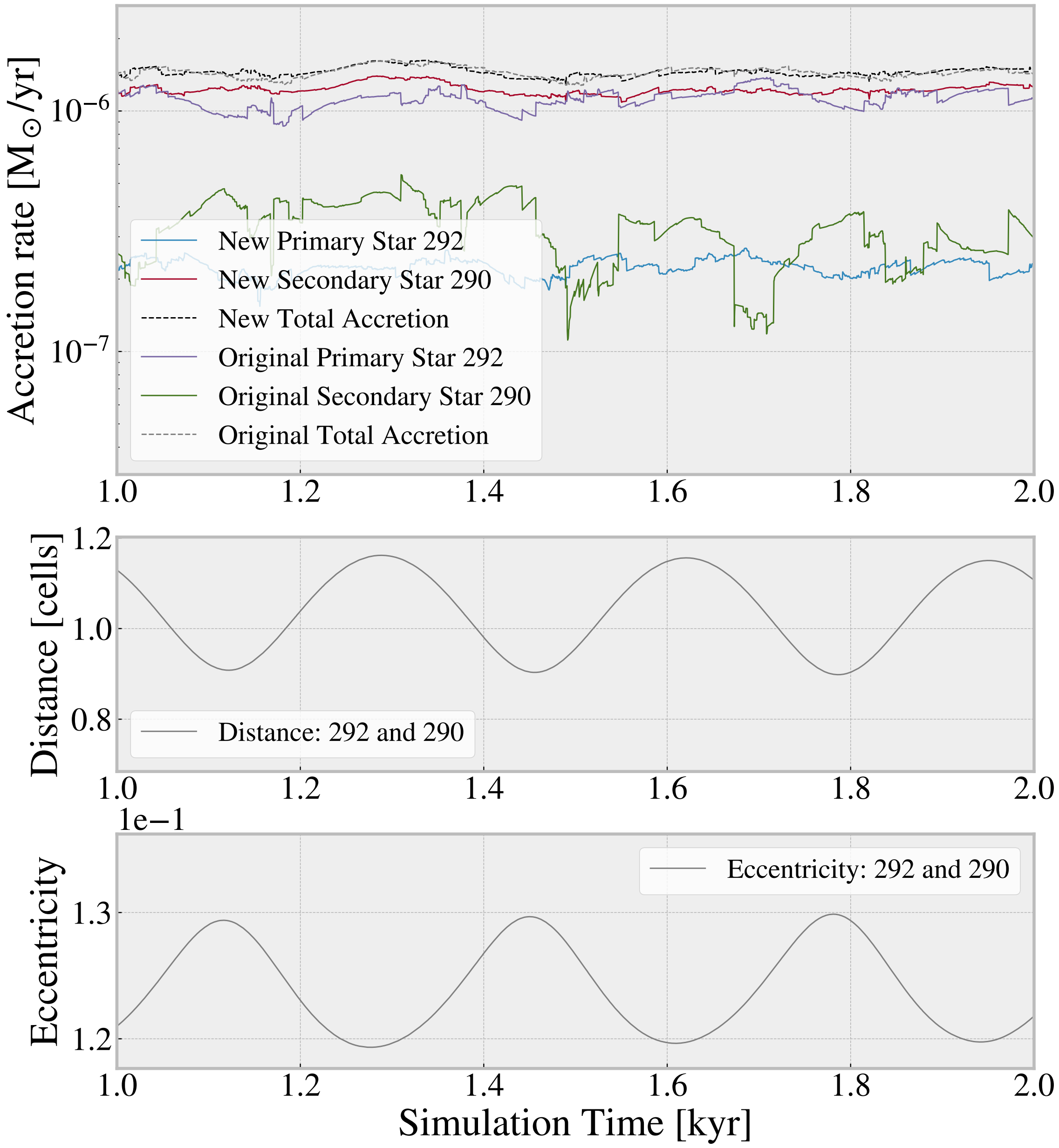

Figure 5.24: The accretion rate of binary pair 25, consisting of sink particles 292 and 290, over a timespan of 2 kyr. It also shows the distance in cells along with the eccentricity of the orbit.

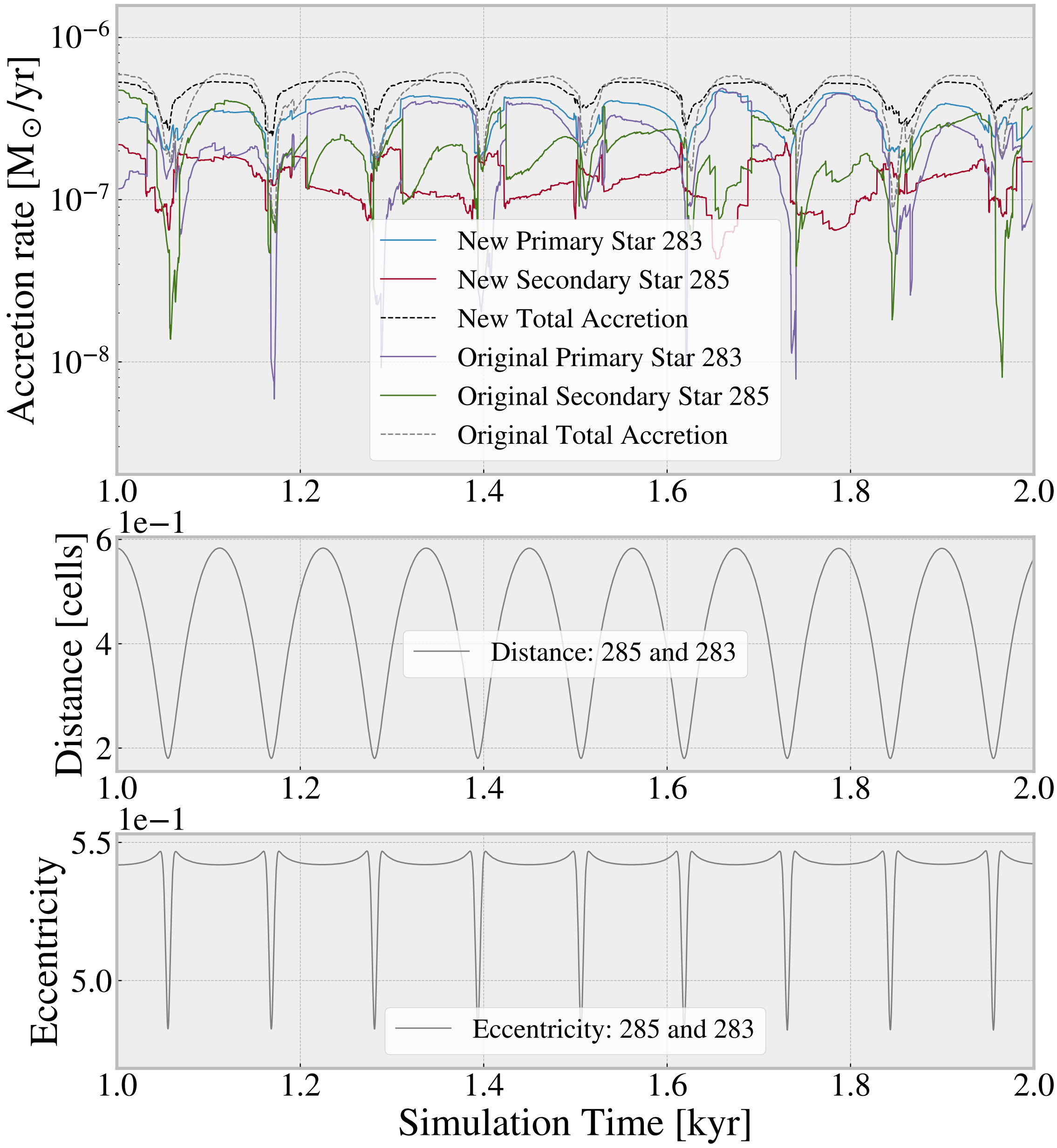

Figure 5.25: The accretion rate of binary pair 28, consisting of sink particles 283 and 285, over a timespan of 2 kyr. It also shows the distance in cells along with the eccentricity of the orbit. These two sink particles are within 1 cell distance to each other at all times in this plot, which also means inaccurate eccentricities at the shortest distances.

Finally pair 15 consists of stars 186 and 221, that has masses 2.01 $M_\odot$ and 0.83 $M_\odot$ respectively, with a mass ratio of $q = 0.41$. This system is part of a triple system which can be seen in the smaller periods during one longer period on the distance part of Fig. 5.26. This also means that our eccentricity calculation is no longer accurate as can be seen on the number going all the way up to 50, so for these stars we will ignore that. The third star of the system is significantly smaller and orbits mostly the secondary star, 221, of this system, which shows up as small wiggles in the distance part of the figure. We infer the orbital period of stars 186 and 221 to be about 2 kyr as we see just about half a period in this range of 1 kyr.

When we look at the accretion rates in Fig. 5.26 we see something quite interesting, since this is a triple system. We see that overall the total accretion is quite similar between the new method and the old method, and until the distance is about 5 cells the secondary stars' accretion rates are identical. This is because the binary accretion has not turned on at this point, but when it does the secondary star accretes less than the old method and varies according to the periodic motion of the secondary star and the tertiary star, inferred from the wiggles in the distance plot and from other figures that look directly at those two sink particles. This is a good illustration that the binary accretion is only relevant when the two sinks have overlapping accretion radii and when that is not the case, the old method is still used. Furthermore, we see many drops in the primary star of the old method, and these are eliminated with binary accretion turned on. This is once again a good sign that the binary accretion is indeed working as intended by giving more physical accretion rates in binary systems.

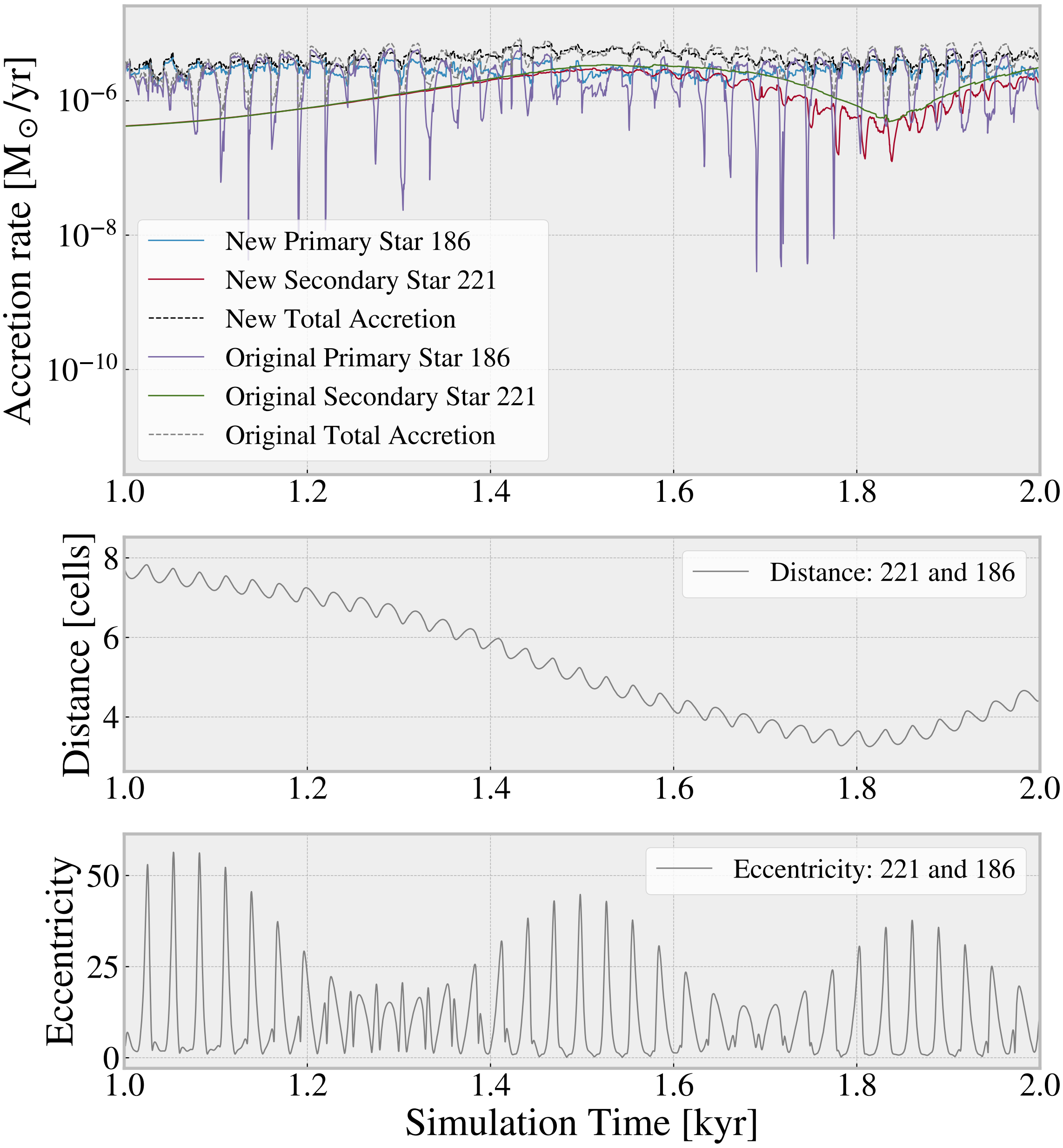

Figure 5.26: The accretion rate of binary pair 15, consisting of sink particles 186 and 221, over a timespan of 2 kyr. This binary pair is part of a triple system. It also shows the distance in cells along with the eccentricity of the orbit. Note here that due to this being a triple system, the calculation of the eccentricity is inaccurate making the bottom panel meaningless in this timespan.

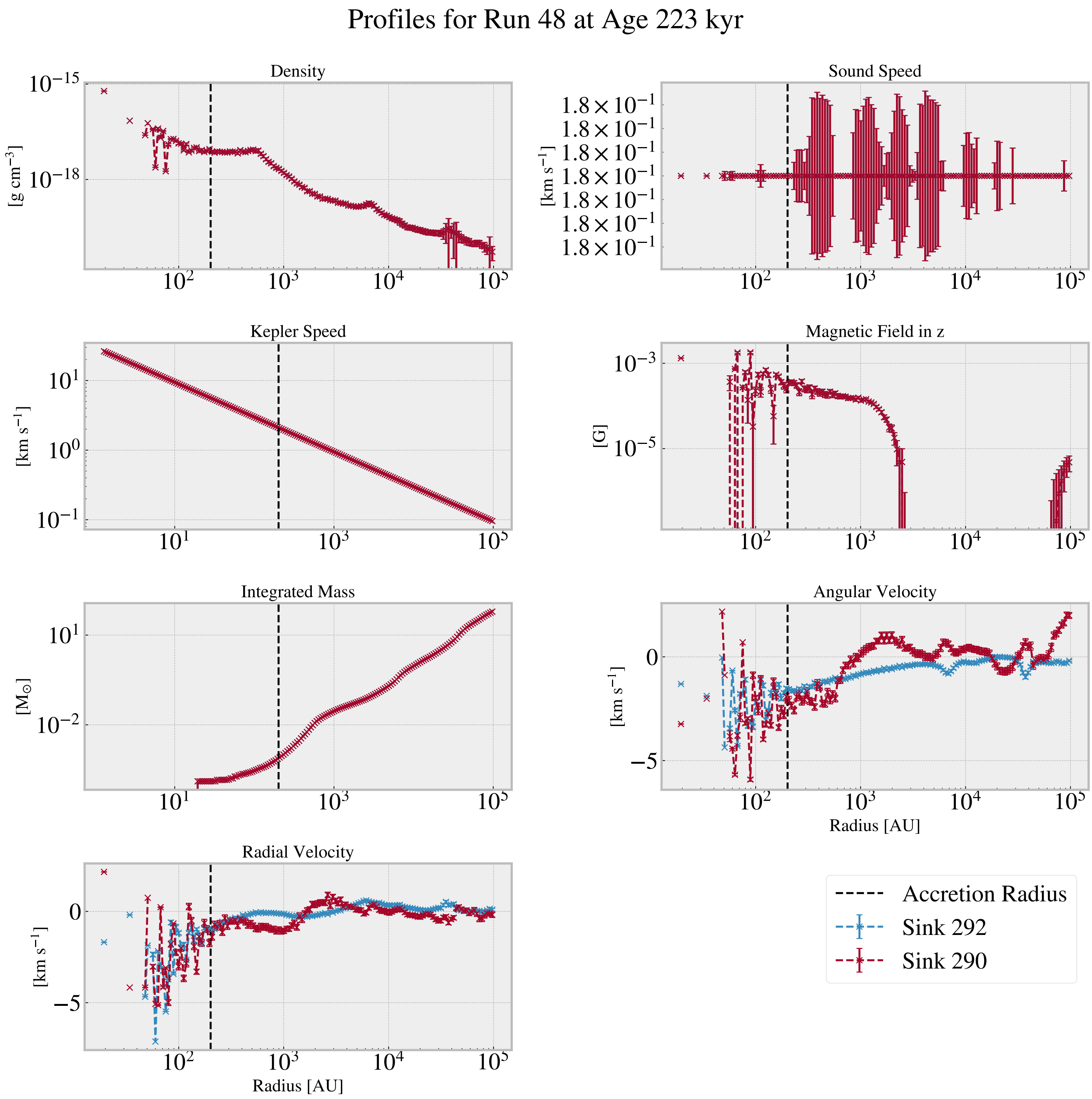

Figure 5.27: Radial profiles of binary pair 25 where sink particle 292 is the primary star of the system and sink particle 290 is the secondary star. The time the profiles are calculated is the last output of the simulation.

Another way to check that the preferential accretion method works as intended, is to inspect the radial profiles for each run, and the differences between them. Specifically, we will inspect the radial profiles of pair 25 in Fig. 5.27 and the residuals between run 48 and run 49 of pair 25 in Fig. 5.28. Nevertheless, the conclusions made have been made across other pairs as well and those radial profiles are available here `https://sid.erda.dk/cgi-sid/ls.py?share_id=b4F5pPa2Li`.

The first thing to note here compared to previous radial profiles is that we have radii out to 10^5 AU instead of 10^3 AU which is simply due to differences in resolution and it not being an idealised scenario. The second is that the simulation is isothermal and because of that, the sound speed is constant. This gives rise to odd errorbars on the sounds speed profile, since the calculation assumes it to not be isothermal when considering the errors. The right way to fix it is in the analysis pipeline, which unfortunately was not possible due to time when it was discovered, and so we simply ignore it as it has no effect elsewhere. The density profile has some odd bumps, but since this is a complex simulation, this may simply be explained by other sink particles within the radii shown. We will be able to see this in the residuals if it is present in both simulations. When we look at the Kepler speed and integrated mass, these both look as we expect, so nothing critical has gone wrong. We do see that the magnetic field in the range 2×10^3 AU to 6×10^4 AU is zero. This may simply be due to the fact that we measured the z-direction of the magnetic field strength, and again it is a much more complex setup. The important thing here is that it looks consistent and it drops off rapidly just after 10^3 AU. Finally, when looking at the velocities, we remember that sink 290 is the secondary star, and we can see the angular velocity of this varying much more than the primary star. This means that the material is more attracted to the primary star and so the angular velocity compared to the secondary star varies since their relative velocities are different. When we look at the radial velocity we see this as well, where at a few 10^3 AU we see the gas move towards the primary star and away from the secondary star, but closer to the stars it moves faster towards the secondary star. This is the same that we see with the accretion rate of sink 290 in Fig. 5.24 where it is higher than the primary star.

Looking at the residual profiles in Fig. 5.28 in order to see the changes between runs 48 and 49 on larger scales. Here we see that the residual density is zero and so we can conclude that the bumps we saw earlier in Fig. 5.27 are likely other stars in the simulation or at the very least that the increased densities are present in both simulations. The sound speed is also effectively zero, and once again we see numerical oddities due to the isothermal sounds speed calculated as if it was not isothermal. Again this should be fixed in the analysis pipeline itself but was spotted too late. We then see the Kepler speed approaching zero and the residual is low outside the

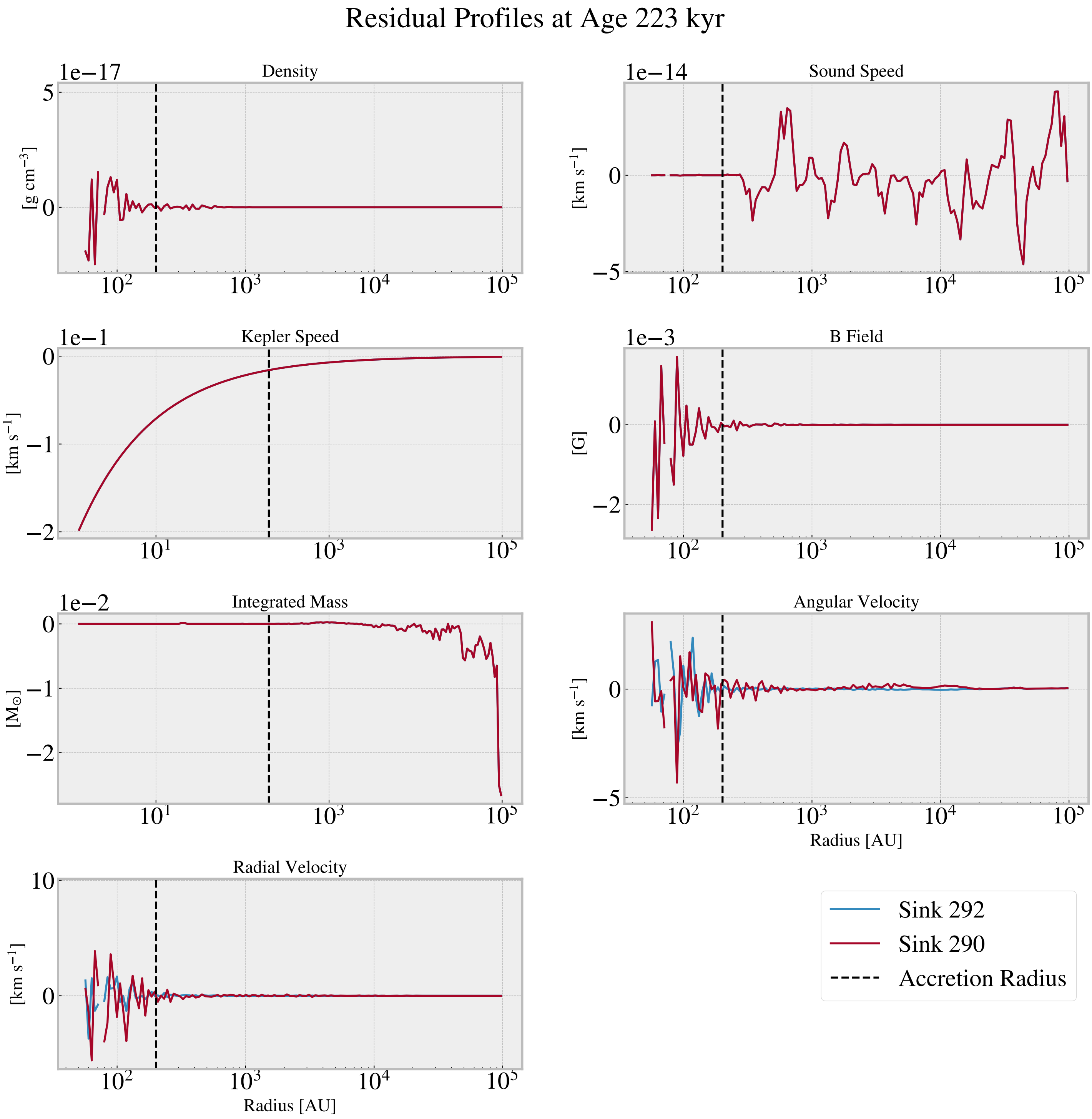

Figure 5.28: Residuals of radial profiles of binary pair 25 in runs 48 and 49, defined as run 48 - run 49. Sink particle 292 is the primary star and sink particle 290 is the secondary star. The time the profiles are calculated is the last output of the simulation.

accretion radius. The magnetic field residuals are also zero. Interestingly the integrated mass is zero until a few 10^3 AU after which it starts dropping. This means that the mass in run 49 without binary accretion activated is larger at large distances. The difference is only of order 10^{-2} $M_\odot$ which is small when integrating all the mass in a sphere with radius 10^5 AU and so we see it more as a peculiar feature than a problem. Finally, looking at the velocities we do see some differences. The radial velocities are very close, but just outside the accretion radius we see the secondary star varying slightly above and below zero. We see a similar story with the angular velocity of the secondary star. This shows us that the binary accretion method does not overall impact the environment around the sink particles and on larger scales, but it does impact the dynamics of the binary system itself. Although the changes are small, they are present. In order to fully understand these changes in dynamics, these simulations need to be run for much longer and several binary pairs need to be investigated and followed across the duration of the simulation, which has unfortunately not been possible to do for this thesis.

In this section we have seen that implementing preferential binary accretion for close binaries gives us a physics driven way of dealing with binary systems that has been shown to avoid extreme unphysical changes in accretion rates that we saw previously. This has worked as a proof of concept, but in order to fully put this in production in RAMSES we need to test it in significantly more scenarios and make sure that it always works as intended. However, it is a great starting point and it is promising for developing this further, where it would also be good to incorporate ways of dealing with triple and other multiple systems.

Chapter 6

Conclusion

In this thesis we have investigated the accretion process using sink particles in an idealised setup with various different parameters for both physical initial conditions and numerical setups at several different resolutions. We also implemented tracking of the induced spin in the forming protostar which we tested in a variety of setups, both idealised and more realistic zoom-in simulations as well as using various different resolutions. Finally, we implemented a different accretion recipe to check for and handle close binary systems where their accretion radii overlap. This was tested with a simulation of a well developed star forming region with both the accretion recipe turned on and off. These are our main objectives and their results:

1. Setting up a simulation of an idealised core collapse well suited to test various parameters and implementations to the code. We fine-tuned this setup by performing a parameter study of some of the parameters present in RAMSES. Furthermore, we used the setup to test our spin implementation and showed that it worked as intended.
2. Testing the spin implementation in a realistic scenario in a zoom-in simulation at three different resolutions, where we simultaneously tested the accretion rates and total accreted mass against resolution. We get good agreement with accretion rates and accreted mass across resolutions concluding the zoom-in simulations are a great tool in the investigation of stellar evolution, specifically for a single star or a few stars, as otherwise it is too expensive computationally.
3. Implemented a new accretion recipe inspired by literature on binary black holes that specifically aims to model accretion for close binary systems by preferential binary accretion. This was shown to reduce the unphysical accretion rate variability we often saw in binary systems before this implementation.

The implications of these are that in 1. we have successfully made a setup that can be reused to perform quick tests of new implementations in the simulation code of various situations. This works as a fast way to test if there are any simulation breaking bugs in the implementation itself. However, it is not suited for investigating the physics, since the idealised setup is not reflecting a more realistic scenario as we see in (Kuffmeier 2017) and in section 5.2.

For 2. we have shown that our implementation of spin tracking successfully tracks the spin of the sink particle and allows us to investigate the rotation of the star compared to the orientation of the disk, since we observed this changing throughout the simulations. Further, we have shown that accretion rates and total accreted mass remains comparable across $\ell_{\text{max}} = 17,\ 18$, and 19. This means that it is possible to do zoom-in simulations at lower resolutions, and so save costs on computational time, if accretion rate and accreted mass is the desired parameters of the star, or if one wants to develop the star and the area close around it before changing to a higher resolution. It is crucial to keep the computational costs in mind and consider the pros and cons of each approach before deciding on how to simulate what we want to investigate. With the zoom-in approach we see the cons as not being able to simulate many stars at once. Or in other terms, that simulating all stars in the star forming region has great computational costs, even when lowering the resolution of the zoom-in simulations.

Finally for 3. we have shown that our new accretion recipe inspired by simulation data from binary black holes, (Siwek et al. 2022), and theoretical considerations, (Kelley et al. 2019), shows promising results on eliminating the unphysical rapid changes in accretion rates that we saw previously. This has only been shown in one comparative simulation so far which means that the results are to be interpreted as such. In order to fully put this in production in RAMSES significantly more testing in various edge scenarios is required along with comparing to previous simulations where binaries are present. One specific test is a high resolution zoom-in simulation of a binary system with both the recipe turned on and off, as we have already shown that zoom-in simulations are an incredibly powerful tool to investigate a single system.

From this work we conclude that although our results have several drawbacks, (mainly from not being tested thoroughly enough for the production version of the code,) they do indeed show promise in further working towards this. Especially the tracking of spin, although being a minor code change, can have big implications for the visualisation aspect of the analysis process. It also has great future potential. Access to a spin direction could be leveraged in a future extension to make a subgrid model for outflows, and with proper rescaling it could track the actual spin of the protostar something that would be of great value for e.g. models of the internal stellar structure based on these data (see e.g. (Jensen and Haugbølle 2018)). The binary accretion recipe shows promise in using a physics inspired recipe to handle the unphysical accretion rate of binaries. In the following we will summarise some of the ways that could improve upon the results and which are natural next steps for this work.

6.1 Future Work

This thesis has produced valuable new extensions to the accretion algorithm and diagnostics for modelling accretion of material to young protostars. It also leaves a number of opportunities and potential next steps open for investigation. Specifically we suggest looking at these parts and investing more time into improving the methods and testing the reliability and how stable it is:

1. Implement the accretion recipe described in section 4.0.3
2. Develop the binary accretion recipe, or a new recipe, to take multiple systems into account, i.e. bound systems of 3 sink particles or more, which we saw occurs often enough that we need a specific and tested way to handle these.
3. Develop a way to handle fly-by events where two sinks overlap accretion radii only for a short time and then never again, i.e. the code sees them as a binary system when they in fact are not. The conclusion to this may be that the current binary accretion recipe works well enough, but it needs to be investigated.
4. Further test the binary accretion recipe to make sure it works as intended in a variety scenarios and use that to convince us that it is ready for the production version of the code.
5. Adapt the work here to the simulation code DISPATCH for speeding up simulations extensively. (Nordlund et al. 2018)

6.2 Acknowledgements

I would like to thank my supervisor, Troels Haugbølle, for his incredible support and feedback throughout this project which has helped shape it into the project that it is, and I achieved much more than I had thought possible because of this. Furthermore, I would like to thank Danai Bili, Ida S. Holk, and Martine Lützen for help with proof reading and sparring of ideas

throughout the project. Finally I would like thank Martine for lending me her skills with drawing figures for a large part of this thesis that have turned out truly incredible.

Bibliography

Armitage, Philip J. (2010). *Astrophysics of Planet Formation.*

Basu, Shantanu (Dec. 1998). "Constraints on the Formation and Evolution of Circumstellar Disks in Rotating Magnetized Cloud Cores". In: *apj* 509.1. _eprint: astro-ph/9808140, pp. 229–237. DOI: 10.1086/306494.

Bate, Matthew R., Ian A. Bonnell, and Nigel M. Price (Dec. 1995). "Modelling accretion in protobinary systems". en. In: *Monthly Notices of the Royal Astronomical Society* 277.2, pp. 362–376. ISSN: 0035-8711, 1365-2966. DOI: 10.1093/mnras/277.2.362. URL: https://academic.oup.com/mnras/article-lookup/doi/10.1093/mnras/277.2.362 (visited on 05/01/2023).

Bodenheimer, Peter et al. (Jan. 2007). *Numerical Methods in Astrophysics: An Introduction.* Publication Title: Numerical Methods in Astrophysics: An Introduction. Part of the Series in Astronomy and Astrophysics. Edited by Peter Bodenheimer.

Bončina, Iztok (Oct. 2010). *ALMA antennas on Chajnantor.* en. URL: https://www.eso.org/public/images/potw1040a/ (visited on 03/17/2023).

Bondi, H. (Jan. 1952). "On spherically symmetrical accretion". In: *mnras* 112, p. 195. DOI: 10.1093/mnras/112.2.195.

Bryan, Greg L. et al. (Apr. 2014). "ENZO: An Adaptive Mesh Refinement Code for Astrophysics". In: *apjs* 211.2. _eprint: 1307.2265, p. 19. DOI: 10.1088/0067-0049/211/2/19.

Commerçon, B. et al. (Apr. 2008). "Protostellar collapse: a comparison between smoothed particle hydrodynamics and adaptative mesh refinement calculations". en. In: *Astronomy & Astrophysics* 482.1, pp. 371–385. ISSN: 0004-6361, 1432-0746. DOI: 10.1051/0004-6361:20078591. URL: http://www.aanda.org/10.1051/0004-6361:20078591 (visited on 10/11/2022).

Federrath, Christoph (2014). "MODELING JET AND OUTFLOW FEEDBACK DURING STAR CLUSTER FORMATION". en. In: *The Astrophysical Journal*, p. 25.

Frimann, S., J. K. Jørgensen, and T. Haugbølle (Mar. 2016). "Large-scale numerical simulations of star formation put to the test: Comparing synthetic images and actual observations for statistical samples of protostars". en. In: *Astronomy & Astrophysics* 587, A59. ISSN: 0004-6361, 1432-0746. DOI: 10.1051/0004-6361/201525702. URL: http://www.aanda.org/10.1051/0004-6361/201525702 (visited on 03/07/2023).

Fromang, S., P. Hennebelle, and R. Teyssier (Oct. 2006). "A high order Godunov scheme with constrained transport and adaptive mesh refinement for astrophysical magnetohydrodynamics". en. In: *Astronomy & Astrophysics* 457.2, pp. 371–384. ISSN: 0004-6361, 1432-0746. DOI: 10.1051/0004-6361:20065371. URL: http://www.aanda.org/10.1051/0004-6361:20065371 (visited on 04/28/2023).

Fryxell, B. et al. (Nov. 2000). "FLASH: An Adaptive Mesh Hydrodynamics Code for Modeling Astrophysical Thermonuclear Flashes". In: *apjs* 131.1, pp. 273–334. DOI: 10.1086/317361.

Hartmann, Lee (1998). *Accretion Processes in Star Formation.*

Haugbølle, Troels (2018). "The Stellar IMF from Isothermal MHD Turbulence". en. In: *The Astrophysical Journal*, p. 25.

Hennebelle, P. et al. (Apr. 2011). "Collapse, outflows and fragmentation of massive, turbulent and magnetized prestellar barotropic cores". en. In: *Astronomy & Astrophysics* 528, A72. ISSN: 0004-6361, 1432-0746. DOI: 10.1051/0004-6361/201016052. URL: http://www.aanda.org/10.1051/0004-6361/201016052 (visited on 10/11/2022).

Hopkins, Philip F. (June 2015). "A new class of accurate, mesh-free hydrodynamic simulation methods". In: *mnras* 450.1. _eprint: 1409.7395, pp. 53–110. DOI: 10.1093/mnras/stv195.

Hoyle, F. and R. A. Lyttleton (Jan. 1939). "The effect of interstellar matter on climatic variation". In: *Proceedings of the Cambridge Philosophical Society* 35.3, p. 405. DOI: 10.1017/S0305004100021150.

Jensen, Sigurd S and Troels Haugbølle (2018). "Explaining the luminosity spread in young clusters: proto and pre-main sequence stellar evolution in a molecular cloud environment". en. In: p. 18.

Kelley, Luke Zoltan et al. (May 2019). "Massive BH binaries as periodically variable AGN". en. In: *Monthly Notices of the Royal Astronomical Society* 485.2, pp. 1579–1594. ISSN: 0035-8711, 1365-2966. DOI: 10.1093/mnras/stz150. URL: https://academic.oup.com/mnras/article/485/2/1579/5304631 (visited on 04/25/2023).

Khokhlov, A. (July 1998). "Fully Threaded Tree Algorithms for Adaptive Refinement Fluid Dynamics Simulations". In: *Journal of Computational Physics* 143.2. _eprint: astro-ph/9701194, pp. 519–543. DOI: 10.1006/jcph.1998.9998.

Königl, Arieh, Raquel Salmeron, and Mark Wardle (Jan. 2010). "Wind-driving protostellar accretion discs - I. Formulation and parameter constraints". In: *mnras* 401.1. _eprint: 0909.2396, pp. 479–499. DOI: 10.1111/j.1365-2966.2009.15664.x.

Krumholz, Mark R., Christopher F. McKee, and Richard I. Klein (Jan. 2005). "Bondi Accretion in the Presence of Vorticity". en. In: *The Astrophysical Journal* 618.2, pp. 757–768. ISSN: 0004-637X, 1538-4357. DOI:

10.1086/426051. URL: https://iopscience.iop.org/article/10.1086/426051 (visited on 09/23/2022).

Krumholz, Mark R., Christopher F. McKee, and Richard I. Klein (Feb. 2006). "Bondi-Hoyle Accretion in a Turbulent Medium". en. In: *The Astrophysical Journal* 638.1. arXiv:astro-ph/0510410, pp. 369–381. ISSN: 0004-637X, 1538-4357. DOI: 10.1086/498844. URL: http://arxiv.org/abs/astro-ph/0510410 (visited on 08/22/2022).

Kuffmeier, Michael (2017). "Zoom-in Simulations of Protoplanetary Disks Starting from GMC Scales". en. In: *The Astrophysical Journal*, p. 21.

Larson, R. B. (Aug. 1969). "Numerical Calculations of the Dynamics of a Collapsing Proto-Star*". en. In: *Monthly Notices of the Royal Astronomical Society* 145.3, pp. 271–295. ISSN: 0035-8711, 1365-2966. DOI: 10.1093/mnras/145.3.271. URL: https://academic.oup.com/mnras/article-lookup/doi/10.1093/mnras/145.3.271 (visited on 03/21/2023).

Larson, Richard B (Oct. 2003). "The physics of star formation". en. In: *Reports on Progress in Physics* 66.10, pp. 1651–1697. ISSN: 0034-4885, 1361-6633. DOI: 10.1088/0034-4885/66/10/R03. URL: https://iopscience.iop.org/article/10.1088/0034-4885/66/10/R03 (visited on 03/23/2023).

Lesur, G. et al. (Mar. 2022). "Hydro-, Magnetohydro-, and Dust-Gas Dynamics of Protoplanetary Disks". In: *arXiv e-prints*. _eprint: 2203.09821, arXiv:2203.09821. DOI: 10.48550/arXiv.2203.09821.

Matsumoto, Tomoaki, Tomoyuki Hanawa, and Fumitaka Nakamura (Apr. 1997). "Gravitational Contraction of Rotating Clouds: Formation of Self-similarly Collapsing Disks". en. In: *The Astrophysical Journal* 478.2, pp. 569–584. ISSN: 0004-637X, 1538-4357. DOI: 10.1086/303822. URL: https://iopscience.iop.org/article/10.1086/303822 (visited on 04/17/2023).

McKee, Christopher F. and Eve C. Ostriker (Sept. 2007). "Theory of Star Formation". en. In: *Annual Review of Astronomy and Astrophysics* 45.1, pp. 565–687. ISSN: 0066-4146, 1545-4282. DOI: 10.1146/annurev.astro.45.051806.110602. URL: https://www.annualreviews.org/doi/10.1146/annurev.astro.45.051806.110602 (visited on 03/31/2023).

Mestel, L. (Feb. 1968). "Magnetic Braking by a Stellar Wind–I". en. In: *Monthly Notices of the Royal Astronomical Society* 138.3, pp. 359–391. ISSN: 0035-8711, 1365-2966. DOI: 10.1093/mnras/138.3.359. URL: https://academic.oup.com/mnras/article-lookup/doi/10.1093/mnras/138.3.359 (visited on 11/29/2022).

Mestel, L. and Jr. Spitzer L. (Jan. 1956). "Star formation in magnetic dust clouds". In: *mnras* 116, p. 503. DOI: 10.1093/mnras/116.5.503.

Mouschovias, Telemachos Ch. (Jan. 1987). "Star formation in magnetic interstellar clouds: I. Interplay between theory and observations." In: *Phys-*

ical Processes in Interstellar Clouds. Ed. by G. E. Morfill and M. Scholer. Vol. 210. NATO Advanced Study Institute (ASI) Series C, pp. 453–489.

Murray, Norman (Mar. 2011). "Star Formation Efficiencies and Lifetimes of Giant Molecular Clouds in the Milky Way". In: *apj* 729.2. _eprint: 1007.3270, p. 133. DOI: 10.1088/0004-637X/729/2/133.

Nakano, Takenori (Feb. 1998). "Star Formation in Magnetic Clouds". en. In: *The Astrophysical Journal* 494.2, pp. 587–604. ISSN: 0004-637X, 1538-4357. DOI: 10.1086/305230. URL: https://iopscience.iop.org/article/10.1086/305230 (visited on 04/03/2023).

Nguyen, Son H., Dongwoo Sohn, and Hyun-Gyu Kim (Feb. 2022). "A novel hr-adaptive mesh refinement scheme for stress-constrained shape and topology optimization using level-set-based trimmed meshes". en. In: *Structural and Multidisciplinary Optimization* 65.2, p. 71. ISSN: 1615-147X, 1615-1488. DOI: 10.1007/s00158-021-03132-6. URL: https://link.springer.com/10.1007/s00158-021-03132-6 (visited on 05/12/2023).

Nordlund, Åke et al. (2018). "DISPATCH: a numerical simulation framework for the exa-scale era – I. Fundamentals". en. In: p. 15.

Offner, Stella S. R. et al. (Mar. 2022). "The Origin and Evolution of Multiple Star Systems". In: *arXiv e-prints*. _eprint: 2203.10066, arXiv:2203.10066. DOI: 10.48550/arXiv.2203.10066.

Pringle, J. E. and M. J. Rees (Oct. 1972). "Accretion Disc Models for Compact X-Ray Sources". In: *åp* 21, p. 1.

Rodenkirch, P. J. et al. (Jan. 2020). "Global axisymmetric simulations of photoevaporation and magnetically driven protoplanetary disk winds". In: *åp* 633. _eprint: 1911.04510, A21. DOI: 10.1051/0004-6361/201834945.

Romanova, Marina M. and Stanley P. Owocki (2016). "Accretion, Outflows, and Winds of Magnetized Stars". In: *The Strongest Magnetic Fields in the Universe*. Ed. by V.S. Beskin et al. New York, NY: Springer New York, pp. 347–397. ISBN: 978-1-4939-3550-5. DOI: 10.1007/978-1-4939-3550-5_11. URL: https://doi.org/10.1007/978-1-4939-3550-5_11.

Ruffert, Maximilian (May 1994). "Three-dimensional Hydrodynamic Bondi-Hoyle Accretion. I. Code Validation and Stationary Accretors". In: *apj* 427, p. 342. DOI: 10.1086/174144.

Ruffert, Maximilian and David Arnett (May 1994). "Three-dimensional Hydrodynamic Bondi-Hoyle Accretion. II. Homogeneous Medium at Mach 3 with gamma = 5/3". In: *apj* 427, p. 351. DOI: 10.1086/174145.

Saigo, Kazuya and Tomoyuki Hanawa (Jan. 1998). "Similarity Solution for Formation of a Circumstellar Disk through the Collapse of a Flattened Rotating Cloud". en. In: *The Astrophysical Journal* 493.1, pp. 342–350. ISSN: 0004-637X, 1538-4357. DOI: 10.1086/305093. URL: https://iopscience.iop.org/article/10.1086/305093 (visited on 04/17/2023).

Salmeron, Raquel, Arieh Königl, and Mark Wardle (Apr. 2011). "Wind-driving protostellar accretion discs - II. Numerical method and illustrative solutions". In: \mnras 412.2. _eprint: 1006.0299, pp. 1162–1180. DOI: 10.1111/j.1365-2966.2010.17974.x.

Schulz, Norbert S. (2012). *The Formation and Early Evolution of Stars*. en. Astronomy and Astrophysics Library. Berlin, Heidelberg: Springer Berlin Heidelberg. ISBN: 978-3-642-23925-0 978-3-642-23926-7. DOI: 10.1007/978-3-642-23926-7. URL: http://link.springer.com/10.1007/978-3-642-23926-7 (visited on 03/03/2023).

Shu, F. H. (June 1977). "Self-similar collapse of isothermal spheres and star formation". en. In: *The Astrophysical Journal* 214, p. 488. ISSN: 0004-637X, 1538-4357. DOI: 10.1086/155274. URL: http://adsabs.harvard.edu/doi/10.1086/155274 (visited on 03/21/2023).

Siwek, Magdalena et al. (Dec. 2022). "Preferential accretion and circumbinary disc precession in eccentric binary systems". en. In: *Monthly Notices of the Royal Astronomical Society* 518.4, pp. 5059–5071. ISSN: 0035-8711, 1365-2966. DOI: 10.1093/mnras/stac3263. URL: https://academic.oup.com/mnras/article/518/4/5059/6824448 (visited on 02/24/2023).

Spitzer, Lyman (1978). *Physical processes in the interstellar medium*. DOI: 10.1002/9783527617722.

Springel, Volker (Jan. 2010). "E pur si muove: Galilean-invariant cosmological hydrodynamical simulations on a moving mesh". In: \mnras 401.2. _eprint: 0901.4107, pp. 791–851. DOI: 10.1111/j.1365-2966.2009.15715.x.

Teyssier, R. (Apr. 2002). "Cosmological hydrodynamics with adaptive mesh refinement: A new high resolution code called RAMSES". en. In: *Astronomy & Astrophysics* 385.1, pp. 337–364. ISSN: 0004-6361, 1432-0746. DOI: 10.1051/0004-6361:20011817. URL: http://www.aanda.org/10.1051/0004-6361:20011817 (visited on 04/28/2023).

Tobin, John J. et al. (Dec. 2012). "A 0.2 solar mass protostar with a Keplerian disk in the very young L1527 IRS system". en. In: *Nature* 492.7427. arXiv:1212.0861 [astro-ph], pp. 83–85. ISSN: 0028-0836, 1476-4687. DOI: 10.1038/nature11610. URL: http://arxiv.org/abs/1212.0861 (visited on 03/23/2023).

Tomar, Suramya (June 2006). "Converting video formats with FFmpeg". In: *Linux Journal* 2006.

Tomisaka, Kohji (Oct. 1996). "Accretion in Gravitationally Contracting Clouds". en. In: *Publications of the Astronomical Society of Japan* 48.5, pp. L97–L101. ISSN: 0004-6264, 2053-051X. DOI: 10.1093/pasj/48.5.L97. URL: https://academic.oup.com/pasj/article-lookup/doi/10.1093/pasj/48.5.L97 (visited on 04/17/2023).

Toomre, A. (May 1964). "On the gravitational stability of a disk of stars". en. In: *The Astrophysical Journal* 139, p. 1217. ISSN: 0004-637X, 1538-4357. DOI: 10.1086/147861. URL: http://adsabs.harvard.edu/doi/10.1086/147861 (visited on 04/03/2023).

Toro, E. F. (2009). *Riemann solvers and numerical methods for fluid dynamics: a practical introduction.* en. 3rd ed. OCLC: ocn401321914. Dordrecht ; New York: Springer. ISBN: 978-3-540-25202-3 978-3-540-49834-6.

Truelove, J. Kelly et al. (Nov. 1997). "The Jeans Condition: A New Constraint on Spatial Resolution in Simulations of Isothermal Self-gravitational Hydrodynamics". en. In: *The Astrophysical Journal* 489.2, pp. L179–L183. ISSN: 0004637X. DOI: `10.1086/310975`. URL: `https://iopscience.iop.org/article/10.1086/310975` (visited on 09/15/2022).

Tsukamoto, Yusuke et al. (Sept. 2022). *The role of magnetic fields in the formation of protostars, disks, and outflows.* en. arXiv:2209.13765 [astro-ph]. URL: `http://arxiv.org/abs/2209.13765` (visited on 11/29/2022).

Vaytet, Neil (2022). *Osyris - Visualization for Ramses — osyris documentation.* Documentation. URL: `https://osyris.readthedocs.io/en/stable/` (visited on 03/09/2023).

Wadsley, James W., Benjamin W. Keller, and Thomas R. Quinn (Oct. 2017). "Gasoline2: a modern smoothed particle hydrodynamics code". In: *mnras* 471.2. _eprint: 1707.03824, pp. 2357–2369. DOI: `10.1093/mnras/stx1643`.

Wardle, Mark and Arieh Koenigl (June 1993). "The Structure of Protostellar Accretion Disks and the Origin of Bipolar Flows". In: *apj* 410, p. 218. DOI: `10.1086/172739`.

Zhao, Bo et al. (Apr. 2020). "Formation and Evolution of Disks around Young Stellar Objects". en. In: *Space Science Reviews* 216.3. arXiv:2004.01342 [astro-ph], p. 43. ISSN: 0038-6308, 1572-9672. DOI: `10.1007/s11214-020-00664-z`. URL: `http://arxiv.org/abs/2004.01342` (visited on 04/05/2023).